UNIVERSIDAD DE CHILE
FACULTAD DE CIENCIAS
DEPARTAMENTO DE FÍSICA

ENHANCED ELECTROMAGNETIC FLUCTUATIONS FROM HIGH-ENERGY ELECTRONS: A REVIEW OF KAPPA DISTRIBUTIONS

TESIS PARA OPTAR AL GRADO DE
MAGÍSTER EN CIENCIAS CON MENCIÓN EN FÍSICA

DANIEL HERMOSILLA PIZARRO

PROFESOR GUÍA:
PABLO S. MOYA

MIEMBROS DE LA COMISIÓN:
VÍCTOR MUÑOZ
ROBERTO NAVARRO
MARIO RIQUELME

SANTIAGO DE CHILE
2023

FACULTAD DE CIENCIAS UNIVERSIDAD DE CHILE INFORME DE APROBACIÓN

Se informa a la Escuela de Postgrado de Magíster presentada por el candidato:

Daniel Iván Hermosilla Pizarro

Ha sido aprobado por la comisión de Evaluación de la tesis como requisito para optar al grado de Magíster en Ciencias con mención en Física, en el examen de Defensa Privada de Tesis rendido el día 10 de Abril de 2023.

Director de Tesis:

Dr. Pablo S. Moya .....

Comisión de Evaluación de la Tesis:

Dr. Víctor Muñoz .....

Dr. Roberto Navarro .....

Dr. Mario Riquelme .....

Biography

I was born in Santiago in 1995. With my mother and sister, we lived for a year in Mulchén and then settled in Quilpué, in the Valparaíso region. We religiously visited our grandmother in Recoleta every weekend. I grew up with my cousins in Santiago and with my sister in Quilpué. In the fifth region, I had the opportunity to study at the colegio Alemán de Valparaíso throughout my primary and secondary education. After finishing high school, I decided to study Physics at the Universidad de Chile. When I obtained my Bachelor's degree, I decided to continue in academia in the Physics Master's program. Nowadays, with a deep love for research, I have formed an absolute conviction of how cross-cutting science is. If there is something immeasurable in life, it is always possible to make it measurable under the ideological prism of science.

Summary

In the inner heliosphere, space measurements have revealed that plasma can be described by the Kappa distributions family, which are characterized by the value of κ, indicating how far plasma is from the ideal Maxwell-Boltzmann equilibrium distribution. In magnetized plasma with enough temperature, spontaneous emissions such as magnetic fluctuations can emerge when a free source of energy is available. When supra-thermal plasma species are involved, these emissions get enhanced, and the Kappa distribution family improves the description of the related non-thermal effects. However, the lack of agreement over Kappa distribution interpretations and applications highlights the need for further exploration to gain a proper understanding of their properties and applications.

In this work, we present a systematic and quantitative comparison of Kappa-distributed magnetized plasma with the Original-Olbertian and Modified versions of Kappa distributions through electromagnetic fluctuations in different temperature anisotropy (A), plasma beta (β), and kappa value (κ) scenarios. Our results show that Olbertian-Kappa electron species exhibit high energy levels that scale with increasing values of β and decreasing values of κ, even when the same thermal speed is considered for all studied cases. Conversely, Modified-Kappa supra-thermal electron species exhibit less total magnetic energy results with lower kappa values, even when compared to the Maxwell distribution equilibrium results in the same macroscopic parameter configuration.

This work demonstrates quantitative differences in the spectrum of magnetic fluctuations when Kappa distributions are involved. With this study, we aim to provide a powerful spectrum analysis tool to gain insights about κ-distributed plasma in space via indirect measurements of fluctuating field correlations.

To all my family, fellas, and pets who passed away while I was working on this beautiful project.

Acknowledgments

Thanks to the Physic's postgraduate program from the Universidad de Chile for the duty-free scholarship and the support of ANID through Fondecyt grants No. 1191351 (P.S.M.).

Contents

Chapter 1

Introduction

Plasma is an exceptional form of matter that exists in our observable universe. It is noted by the removal of electrons from atoms, which results in the development of an ionized gas. Consequently, this medium is saturated with numerous charged particles, leading to complex interactions between them. Moreover, such interactions between charged particles may be binary or collective, making the plasma rich in wave physics with wave-wave or wave-particle interactions [1, 2]. Nevertheless, the largest laboratory of plasma research exists beyond the Earth, in space, encompassing the entire Solar system and even extending beyond it.

The plasma that propagates through space from the Sun provides an opportunity to study the thermodynamics of the Solar System. This plasma is mainly influenced by the interplanetary magnetic field, and this feature makes plasma susceptible to magnetization with arising and evanescence currents due to the drifting of charged particles. In addition, space plasma in our Solar System generally evolves in a virtual collision scenario. Thus, particles probably do not experience hard collisions, but rather interact with each other through collective behavior mediated by magnetic fields generated by other particles. This feature is highly efficient in maintaining quasi-stable thermal conditions in the constantly hot, diluted, and poorly collisional scenario of space plasma.[3, 4].

The poorly-collisional nature of plasma leads to unexpectedly low cooling rates and unsolved thermal relaxation processes [5–9]. Hence, space plasma is characterized by long-range interactions of charges with high correlations between charge densities, induced currents, and electromagnetic fields. These correlations are accounted by neglecting the binary collision scenario, as correlations arise simultaneously between all interactions of particles in plasmas, making them non-independent from each other. Otherwise, these correlations may be destroyed by randomly considering binary collisions at a certain time, thereby ignoring the development of spatial and

temporal correlations [10].

In theory, in a magnetized plasma scenario, these correlations in poorly-collisional plasmas holds on a scale relative to the gyroradius and gyromotion of electrons. Therefore, the plasma develops a mechanism that acts in a shorter time compared to the collision frequency to maintain itself in quasi-stable thermal conditions. Such a scenario occurs in plasmas emanating from the Sun, where observational data measure non-Maxwellian particle velocity distributions [11, 12]. Instead of decaying through larger velocities following a Gaussian distribution, it follows a power-law behavior that is well-fitted by kappa distributions. The high-energy tails of these distributions exhibit a decay that follows the Lorentzian function. In addition, they depend on the kappa value, which is a measure of how far the kappa distributions deviate from the thermal equilibrium that is described by a Maxwell distribution.

The morphology of velocity distributions in space plasma is affected by several non-thermal effects, such as electrostatic and electromagnetic instabilities, turbulence, non-linear particle-wave, and wave-wave interactions, etc. [13–15]. Additionally, the long-range interaction of charged species with high levels of correlation breaks the ideal Gibbs-Boltzmann statistics [16, 17]. Therefore, it is reasonable to explore generalized velocity distribution models like kappa distributions that go beyond ideal equilibrium statistics [18, 19].

The use of kappa distributions takes into account the contribution of the high thermal energy population in addressing typical space plasma problems. For example, it can be used to improve the description of the heat flux during the acceleration of the solar wind, as well as to describe enhanced kinetic instabilities driven by anisotropies, or to improve the description of non-thermal features such as particle acceleration during magnetic reconnection, as occurs in our magnetosphere [20, 21]. Generally, velocity distribution measurements in the solar wind and near Earth's magnetosphere usually arise in quasi-stable plasma conditions and involve suprathermal particles. In this scenario, the poorly-collisional feature cannot ensure local thermal equilibrium, and due to its purely electromagnetic nature, the plasma exists for a long time in a state of kinetic turbulence [22, 23]. Moreover, the linear kinetic theory on Vlasov-Maxwell's equations predicts transverse electromagnetic and parallel electrostatic collective modes for magnetized plasma. They include, ordinary, extraordinary, and whistler-cyclotron modes for transverse waves and Langmuir waves [24, 25].

For waves propagating parallel to the background magnetic field, the stability of the whistler-cyclotron mode is affected by suprathermal electrons with a velocity large enough to reach the phase velocity of the wave and exchange energy via cyclotron resonance [26]. This results in positive growth rates for the whistler-cyclotron instability, which are typically higher than those predicted by a Maxwell distribution. Thus, to obtain an accurate and comprehensive description of plasma fluctuations, the contribution of suprathermal particles must be considered not only

in the measurements of dispersion properties but also in the overall fluctuating behavior of the plasma [27, 28].

A key question concerning kappa distributions is how they are formed in the space plasma environment. These distributions are believed to develop in plasma environments where particle acceleration is expected, due to the presence of enhanced tails. This suggests that they develop in regions where heating mechanisms are present, particularly in scenarios involving Langmuir and cyclotron resonances, such as those found in electrostatic and electromagnetic turbulence in the solar wind. Furthermore, these distributions exhibit not only enhanced tails but also distinct core shapes, illustrating the versatility of this distribution in various space plasma environments.

Despite their prevalence in space plasmas, kappa distributions have been subject to questions about their fundamental properties due to theoretical interpretations. For instance, when kappa values are low, these distributions exhibit non-exponential decay, which results in their divergence at higher-order moments of velocity. Besides, these distributions cannot achieve the additive property of entropy that is obtained from thermodynamics. Instead, when computing this property, a subtractive term appears, and its interpretation is unclear. The purpose of this example is to evidence that kappa distribution presents several challenges for understanding its model, and while it is not the primary focus of this writing, it deserves further exploration [29]. However, empirical observational results of these distributions are ubiquitous in space plasma literature [30]. We think that it is time to develop a proper interpretation for these distributions to better understand the theoretical results and their implications.

In the literature, we can identify two main interpretations of the kappa models. The first distribution corresponds to the Olbertian distribution, which was originally proposed empirically for measuring the energy values of electrons in the Earth's magnetotail [31, 32]. In this space plasma scenario, one would expect acceleration of particles due to excess energy in the magnetic reconnection. This inadvertently or intentionally proposes a scenario for particle acceleration where this distribution may be preferably developed. On the other hand, another interpretation of the kappa distribution considers it to be developed in a scenario where a mechanism can retain larger densities of particles with lower velocities than predicted by a Maxwell distribution. Besides, the same mechanism or another can develop a small density of particles with large velocities [10]. Therefore, this interpretation of kappa distributions suggests that they may be developed in resonance scenarios, such as electromagnetic resonance. The modified kappa interpretation retains the concept of temperature from thermodynamics, in contrast to the original Olbertian distribution. The Olbertian distribution defines a temperature that depends on the κ parameter, and this temperature is larger than what would be computed from the Maxwell distribution in the framework of kinetic theory. Therefore, these interpretations of kappa distribution are still under discussion for their appropriate application in space

plasma scenarios.

Considering the examples shown above and the background of kappa distributions, in this thesis we adressed the following question: how can we differentiate between the two main interpretations of kappa distributions using electromagnetic fluctuations? Recently, Marian Lazar *et al.* [33], showed different destabilizing effects of supra thermal population in the whistler-cyclotron dispersion branch in a plasma modeled with the two kappa distribution interpretations. Here, we suggest that the continuum spectra of magnetic fluctuations around this branch are different, and the study of them will offer relevant information about the morphology of each distribution.

This work analyzes the levels of finite electromagnetic fluctuations using both thermal and non-thermal descriptions of high-energy electron populations through kappa distributions with the same thermal speed. The analysis aims to demonstrate differences in the energy of the continuum fluctuating spectra, where the plasma system only considers parallel dispersion branches in relation to the background magnetic field. We perform a schematic analysis of the magnetic field fluctuation spectrum in terms of the temperature anisotropy, the plasma beta, and the kappa parameter. The thesis consists of seven chapters. The next chapter will review the generalities of kappa distributions and electromagnetic fluctuations in the solar wind. The third chapter will review the two main interpretations of kappa models and how to compare them. The fourth and fifth chapters will review the results of linear kinetic and electromagnetic fluctuation theories in magnetized plasma. The sixth chapter will present a comparative scheme of the theoretical results with numerical results obtained from particle-in-cell simulations. The last chapter will provide a summary of the results along with concluding remarks.

Chapter 2

Solar Wind: Relationship with kappa distribution and turbulence

The Sun provides continuous plasma to the interplanetary media extending its last layer, the solar corona, into space [34, 35]. The space domain filled with plasma is called heliosphere and the heliosheath bounds it. Inside this space region, we understand solar wind as the plasma blown out from the Sun. To answer the question of how the plasma is blown out as a wind into the interplanetary medium, there are currently two main theories. One is based on MHD (magnetohydrodynamics), and the other is based on the kinetic framework [36].

In the fluid treatment, the solar wind is explained as a fluid streaming away due to the pressure difference between the Sun and the interplanetary medium. This theory is generally accepted, although it must be taken with care because some assumptions of the heat flux may be partially valid. In this description, the plasma must be close to thermodynamic equilibrium, which is not necessarily true in the corona [35]. Due to this feature, the heat flux by fast electrons goes under a non-collisional regime, resulting in unexpected heat flow rates in the solar wind. Therefore, this theory must assume a uniform temperature (infinite heat conductivity). On the other hand, the kinetic approach takes the solar wind as an evaporation of the outer layer of the Sun into the interplanetary space. This shows no problem with the heat flux because the heat flux is calculated within the theory. However, both theories' limitations are complex and reviewed in the reference [37].

Regardless of the model of its ejection, the solar wind is typically categorized into two velocity regimes: the fast wind, which pertains to bulk ion velocities exceeding approximately $450 - 600$ km/s, and the slow wind, which corresponds to ion velocities below this range. This rough range of velocity threshold is an assumption still under revision [38, 39]. This feature of slow and fast wind arises

from the complex morphology of the Sun's magnetic field. In solar minimum activity, the Sun is dipolar, and the fast wind emerges from a large region in the North and South magnetic poles [37]. This suggests that fast winds come from areas with open magnetic flux, developing larger particle velocities. On the other hand, the slow wind comes from active zones near the magnetic equator. This suggests that the slow wind originates from regions with closed magnetic flux, resulting in slower particle velocity development. During periods of maximum solar activity, it becomes challenging to distinguish between the sources of the fast and slow solar winds as the magnetic field morphology becomes more complex and entangled, resembling a ball of yarn.

The solar wind is primarily composed of hydrogen, with minor quantities of helium isotopes and traces of heavier ions [40]. Due to extremely hot conditions, electrons are ripped away from these atoms, playing a crucial role in the solar wind stabilization or destabilization. The velocity distributions of electrons in the solar wind are often non-equilibrium and can be measured through various means. One such means is the measurement of asymmetry in the velocity field, also known as skewness. Skewness can further evolve into temperature anisotropies through heat flux mechanisms. One way to evidence non-equilibrium velocity distribution measurements of electrons in the solar wind is to study their contribution to non-thermal processes, such as kinetic instabilities and electromagnetic fluctuations.

These fluctuations are often displayed in temperature anisotropy and electron plasma beta diagrams, which show the intensity and occurrence of these fluctuations in different space plasma scenarios, such as slow and fast wind, or magnetic reconnection in the Earth's magnetosphere [41, 42]. The temperature anisotropy represents the ratio between the mean kinetic energy in the background magnetic field axis and the perpendicular direction, while the beta parameter indicates the ratio between the thermal energy and the magnetic energy of any plasma specie. Studying the spectra of such fluctuations in these diagrams can be helpful in detecting plasma that deviate from thermal equilibrium [43–45].

The contribution of electrons with high energy is essential to properly describe the heating mechanism and stability of the solar wind. Recent studies have shown that kappa distribution can better reproduce the electron distribution up to 1 keV compared to a combination of two Maxwellians [11, 46]. Since electrons in the solar wind have a wide range of energy from 1 keV to 10 keV, it is expected that kappa distributions provide a more accurate description. kappa distribution is also a solution state to the electrostatic turbulence [47]. It is worth noting that these electrostatic fluctuations are continuously measured in the solar wind [48, 49].

Moreover, using ideal Maxwell distributions to obtain electrostatic spectra in the solar wind may lead to an unfair computation of the electron temperature [50, 51]. This is because temperature depends on the measured energy range, and the Maxwell distributions are not sufficient to accurately represent energetic electrons in

the solar wind. Considering all these facts about high energy electrons, kappa and ideal Maxwell distributions, and electrostatic turbulence, it is reasonable to believe that kappa distributions are involved in the oscillatory behavior of plasma species through electrostatic and electromagnetic resonance.

As the topic of this work concerns electromagnetic fluctuations, we will briefly review some reasons for the existence of these fluctuations in space plasma. Firstly, it is believed that they could be due to the remnants of MHD turbulence. The turbulence at the MHD scale corresponds to a collection of large-scale waves, whose spatial distribution creates turbulence in the magnetofluid. From this turbulence, kinetic energy is transferred towards smaller scales, causing enhanced thermal motion of electrons, which in turn allows for emissions to occur from them. These emissions are reabsorbed, generating electromagnetic fluctuations. This is schematically shown in the left panel of Figure 2.1, where at the kinetic scale, the zoom represents the stochastic motion of electrons that are provoking electromagnetic fluctuations.

Another possibility for the release of electromagnetic fluctuations in a plasma is when it is initially in an unstable condition near an instability threshold. Then the plasma stabilizes via emissions that are reabsorbed, causing electromagnetic fluctuations. This is schematized in the first two figures of the right panel in Figure 2.1. In the last figure of this panel, we review the third reason, which is when the plasma is initially in a quasi-stable state, meaning that it exists for a long period of time around an equilibrium state with a degree of fluctuations caused by the stochastic thermal motion of particles. For this reason, spontaneous emissions are generated, which are at the same time absorbed by other charged particles, leading to a finite level of electromagnetic fluctuations that can be measured in theory with the fluctuation dissipation theorem [52–54].

Along with the discussion on the origin of the solar wind, turbulence, and the correlation between kappa distributions and these space plasma phenomena, the upcoming chapter will examine two of the primary interpretations of the kappa model, often utilized to describe electron velocity distributions in space plasma scenarios.

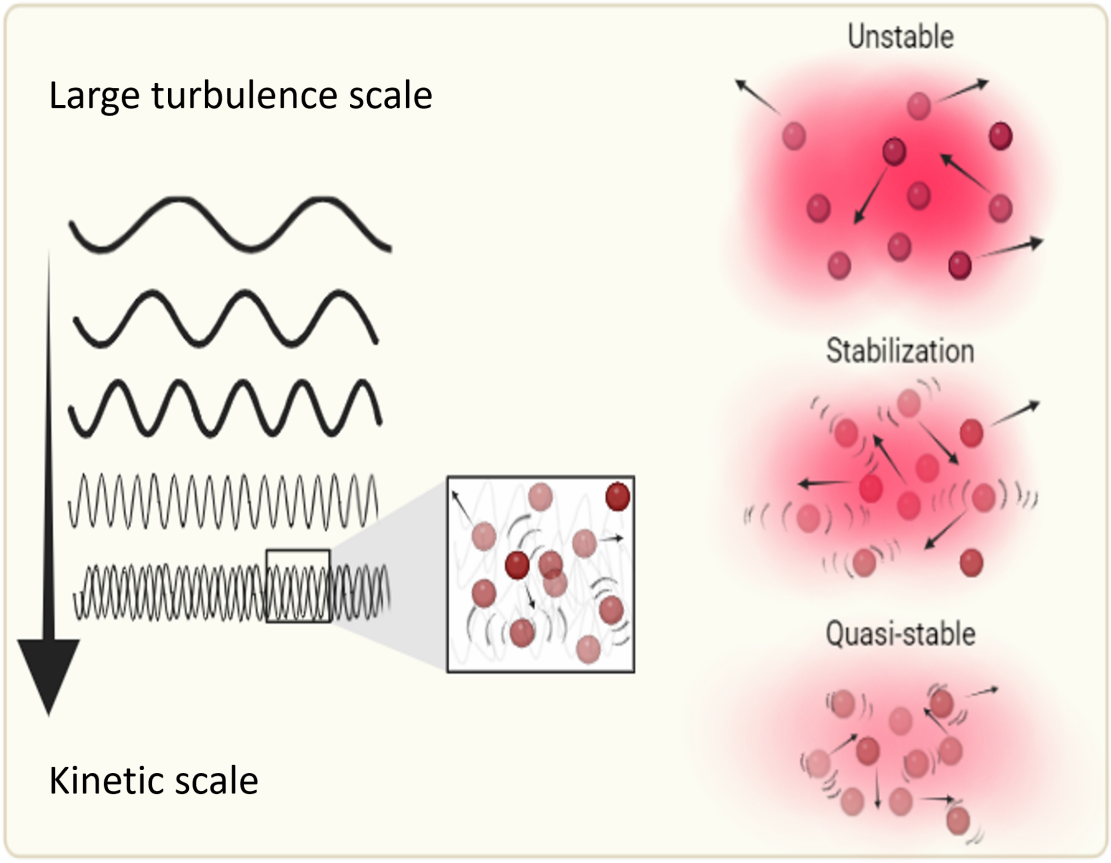

Figure 2.1: The left panel shows the transfer of kinetic energy from MHD turbulence, which results in electromagnetic fluctuations at the kinetic scale. The sinusoidal signal represents turbulence, and the red dot represents electrons with high energy. Additionally, the arrows represent velocities, and the wave symbols represent emissions. The right panel depicts a scenario in which the stabilization of unstable plasmas near an instability threshold occurs due to emissions that generate electromagnetic fluctuations. At the bottom, there is a diagram that illustrates a plasma near an equilibrium state that naturally produces emissions from the thermal motion of charges. These emissions are then reabsorbed by other charged particles, resulting in electromagnetic fluctuations.

Chapter 3

Review of kappa distributions

The family of kappa distributions is advantageous in describing high energy ranges of various plasma species that are far from thermal equilibrium, particularly in space plasma environments, when compared to mixed Maxwell-Boltzmann models[11]. In this approach, each population in plasma with different thermal energies (core, halo, *strahl*, and super-halo) is described by Maxwell distributions with different temperatures to achieve accurate fitting. This results in a larger parameter space and a model that is too specific for each observation, which unfairly describes particles with high velocities, thereby limiting the generalizability of the model [55–57].

Fortunately, the kappa distribution family takes into account the description of particles with both high and low energies. This allows for a single kappa model to provide a better description of the velocity distribution compared to an idealized Maxwellian distribution. Furthermore, kappa distributions are found in abundance in the Sun's structure, the solar wind, the magnetosphere of planets, and throughout the entire solar system and beyond [58–64]. Although this family of kappa functions improves the description in space plasma scenarios, the proper interpretation of its empirical existence and the appropriate choice of its application are still under revision [11, 27].

To explore some of the features of these distributions, we will briefly discuss the difference between the two main kappa models. Specifically, we will focus on two main kappa models in space plasma, using the notation proposed by Lazar in 2021 [11]. According to this notation, the empirical kappa model is referred to as the Olbertian or Original kappa distribution, named after its author [31], similar to how the Maxwellian distribution is named after Maxwell. Alternatively, we refer to a modified interpretation of this distribution as the Modified kappa version because it modifies the parametrization of the original kappa version.[65]. We use subscripts to differentiate between quantities for each distribution. Specifically, we use Mx for

Maxwell distribution quantities, Ob for Olbertian distribution quantities, and Md for Modified distribution quantities.

In order to provide a guide for discerning between the application of kappa distributions, we present the two analytical models for the Olbertian and modified cases in the anisotropic representation. Respectively, they are,

$$F_{Ob}(v) = \frac{n_\alpha \Gamma(\kappa_\alpha + 1)}{\pi^{3/2}\theta_{\perp\alpha}^3 \theta_{||\alpha}^2 \kappa_\alpha^{3/2} \Gamma(\kappa_\alpha - 1/2)} \left(1 + \frac{v_\perp^2}{\kappa_\alpha \theta_{\perp\alpha}^2} + \frac{v_{||}^2}{\kappa_\alpha \theta_{||\alpha}^2}\right)^{-(\kappa_\alpha+1)}, \quad (3.1)$$

$$F_{Md}(v) = C_\kappa \left(1 + \frac{v_\perp^2}{(\kappa_\alpha - 3/2)\theta_{\perp\alpha}^2} + \frac{v_{||}^2}{(\kappa_\alpha - 3/2)\theta_{||\alpha}^2}\right)^{-(\kappa_\alpha+1)}, \quad (3.2)$$

$$C_\kappa = \frac{n_\alpha \Gamma(\kappa_\alpha + 1)}{\pi^{3/2}\theta_{\perp\alpha}^3 \theta_{||\alpha}^2 (\kappa_\alpha - 3/2)^{3/2} \Gamma(\kappa_\alpha - 1/2)}.$$

Here, Γ is the gamma function, $\theta_{\perp,||}$ the thermal speed. The subscript α is the α plasma specie. These representations correspond to the Tsallis-kappa-like models, with the exponent being $-(\kappa_\alpha+1)$ [29]. Additionally, these distributions differ in the framework of kinetic theory due to the κ parametrization of temperature. In plasmas out of equilibrium described by an Olbertian distribution, a kinetic temperature is interpreted for each κ value using the second velocity moment of the distribution. This results in a larger kinetic kappa-dependent temperature than that computed from a Maxwell distribution.

$$T_{||}^{(\kappa_{Ob})} = \frac{m_\alpha}{k_B} \int F_{\kappa_O} v_{||}^2 dv_{||}^2 = \frac{\kappa_\alpha}{\kappa_\alpha - 1.5} T_{||}^{(M)}, \quad (3.3)$$

$$T_{\perp}^{(\kappa_{Ob})} = \frac{m_\alpha}{2k_B} \int F_{\kappa_O} v_{\perp}^2 dv_{\perp}^2 = \frac{\kappa_\alpha}{\kappa_\alpha - 1.5} T_{\perp}^{(M)}. \quad (3.4)$$

This parametrization requires that the concept of thermal speed be retained as equivalent to that computed in thermal equilibrium from a Maxwell distribution.

$$\theta_{\alpha||,\perp}^{(\kappa_{Ob})} = \theta_{\alpha||,\perp}^{(M)}. \quad (3.5)$$

This results in a wider mean width of the kappa distribution while preserving the same peak as the Maxwell distribution. As a result, the morphology of the velocity distribution shows an enhanced tail formed at the expense of the core density but still maintains the quasi-thermal core shape of the Maxwell distribution, as shown in Figure 3.1.

In addition, upon a quick examination of the morphology of both cases, we can find indications of the system where they may have been developed. The morphology

of the Olbertian case is represented in the right panel of Figure 3.1. Compared to the equilibrium, large supra-thermal tails can be observed, indicating that particles have developed higher velocities. In a scenario where the density in phase space of the distribution remains constant, it is expected that these particles with higher velocities are formed at the expense of the core particles. Therefore, a mechanism must be accelerating these particles to form higher densities of particles with more extensive velocities. One hypothetical example of such a mechanism could be electrostatic turbulence in the solar wind. Particles highly influenced by an oscillating electric field gain energy in resonance with electrostatic waves, thereby heating them and increasing their velocities. This is why this type of distribution is widely accepted in the space plasma community, as it offers a natural first attempt description of a space plasma scenario.

On the other hand, the Modified kappa model preserves the same concept of temperature as that obtained in thermal equilibrium.

$$T_{||}^{(\kappa_{Mo})} = \frac{m_\alpha}{k_B}\int F_{\kappa_{Mo}} v_{||}^2 dv_{||}^2 = T_{||}^{(M)}, \tag{3.6}$$

$$T_{\perp}^{(\kappa_{Mo})} = \frac{m_\alpha}{2k_B}\int F_{\kappa_{Mo}} v_{\perp}^2 dv_{\perp}^2 = T_{\perp}^{(M)}. \tag{3.7}$$

$$\tag{3.8}$$

However, this interpretation requires a kappa-dependent thermal speed, which is larger than the one obtained in thermal equilibrium.

$$\theta_{\alpha||,\perp}^{(\kappa_{Mo})} = \frac{2\kappa_\alpha - 3}{2\kappa_\alpha}\theta_{\alpha||,\perp}^{(M)}. \tag{3.9}$$

The Modified kappa model retains the same mean width as the Maxwellian function due to its preservation of the concept of thermodynamic temperature. However, its core has a sharper, narrower, and kappa-dependent peak compared to the Maxwell distribution. To maintain the interpretation of temperature in equilibrium, faint suprathermal tails with the same decay slope as the Olbertian distribution are also present to compensate for the high density of particles with low energy (refer to Figure 3.1). This description is applicable to lower kappa values, while for higher values, both kappa models recover the morphology of a velocity distribution in equilibrium.

Comparing the morphology of the Modified kappa distribution with that of the Maxwell distribution provides insights into the environment in which it may develop. The enhanced peak, which accounts for the kappa-dependent thermal speed, suggests a scenario where a mechanism can retain more particles at low velocities when it is out of thermal equilibrium, compared to the same macroscopic plasma parameters in thermal equilibrium with a Maxwell distribution. This scenario can also accelerate or maintain particles with larger velocities, forming faint suprathermal tails. These

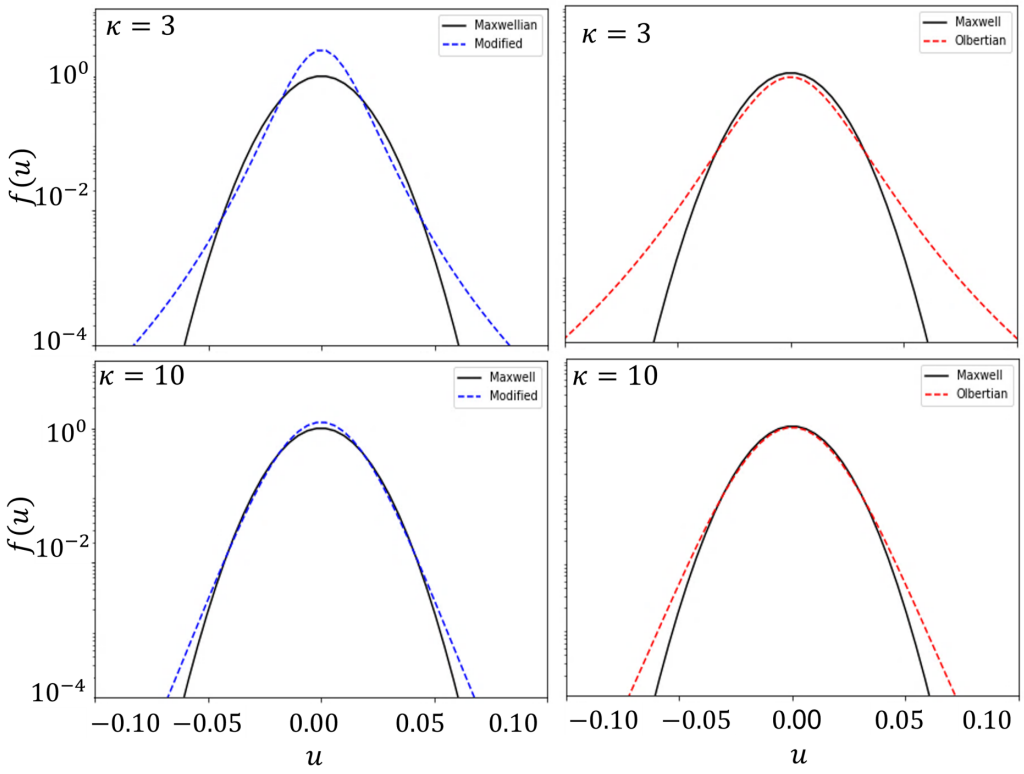

Figure 3.1: The figure displays the velocity distribution functions of both the kappa and Maxwell models. $f(u)$ is the respective distribution function and u is a dimensionless velocity normalized to an arbitrary value. The solid line represents the Maxwellian distribution, while the dashed lines show the kappa distributions for two values of the parameter κ: a large non-thermal scenario with $\kappa = 3$ and a nearly thermal equilibrium scenario with $\kappa = 10$. The range of kappa values between these two thresholds is typical of the non-thermal regimes encountered in the Heliosphere at distances of 1 to 3 astronomical units (AU) from the Sun [65].

observations suggest that the mechanism involved corresponds to an electromagnetic resonance scenario.

Both kappa distributions have been shown to accurately represent various space plasma scenarios, either theoretically or empirically. In the next chapter, we will explore their associated electromagnetic fluctuations and the results obtained from these analyses.

Chapter 4

Kinetic linear theory and electromagnetic fluctuations

4.1 Review of dispersion theory for kappa distributions

We obtained expressions for the dispersion tensor elements in magnetized plasmas using linear kinetic theory. In our notation, subscripts $\pm$ and $||$ indicate perpendicular and parallel directions, respectively, with respect to the background mean magnetic field. The $\pm$ subscript refers to the right- or left-hand helicity of the wave.

At a particular point ($t = 0$) in the Vlasov-Maxwell system, we introduce an electric and magnetic field disturbance and a perturbation of the velocity distribution under neutral and current-free initial conditions.

$$\begin{aligned} \mathbf{E} &= \delta\mathbf{E}, \\ \mathbf{B} &= \mathbf{B}_0 + \delta\mathbf{B}, \\ f &= f_0 + \delta f. \end{aligned}$$

Here, δ represents perturbed quantities at first order, and the subscript 0 represents equilibrium quantities. By retaining only first-order terms, we found an analytical expression for the dispersion tensor. This tensor is diagonal when we consider waves propagating parallel to the background magnetic field. The dispersion relation of waves propagating parallel to the background magnetic field is computed with the equation

$$\Lambda_+\Lambda_-\Lambda_{||} = 0, \tag{4.1}$$

where $\Lambda_{||}$ and $\Lambda_{\pm}$ are the diagonal elements of the dispersion tensor in the parallel and perpendicular directions with respect to the background magnetic field, respectively. Here, the components of the dispersion tensor are

$$\Lambda_{\pm} = 1 - \eta^2 + 4\pi \sum_{\alpha} \chi_{\pm\alpha}, \tag{4.2}$$

$$\Lambda_{||} = 1 + 4\pi \sum_{\alpha} \chi_{||\alpha}. \tag{4.3}$$

The sum is over α plasma species and χ_{α} represents the electric susceptibility tensor. Also, $\eta = ck/\omega$ corresponds to the wave refractive index. The electric susceptibility tensor elements are

$$\chi_{\pm\alpha} = \frac{\omega_{p\alpha}^2}{4\omega} \int \frac{\partial f_{\alpha}}{\partial v_{\perp}} \pm \frac{k_{||}}{\omega} \left(v_{\perp} \frac{\partial f_{\alpha}}{\partial v_{||}} - v_{||} \frac{\partial f_{\alpha}}{\partial v_{\perp}} \right) dv_{||} dv_{\perp}, \tag{4.4}$$

$$\chi_{||\alpha} = \frac{\omega_{p\alpha}^2}{4\omega} \int \frac{v_{||} v_{\perp}}{\omega - k_{||} v_{||}} \frac{\partial f_{\alpha}}{\partial v_{||}} dv_{||} dv_{\perp}. \tag{4.5}$$

$$\tag{4.6}$$

Here, we obtained these expressions in the Fourier-Laplace domain as it is the natural space for signal analysis. Hence, k and ω represent the frequency and wave number, respectively, after transforming time-space quantities. Additionally, $\omega_{p\alpha}$ denotes the plasma frequency.

In the case of the Maxwell distribution, the susceptibility tensor elements are

$$\chi_{\pm} = \frac{\omega_{p\alpha}^2}{4\pi\omega^2} \left(A + \phi_{\pm} Z(\xi_{\pm}) + 1 \right), \tag{4.7}$$

$$Z(\xi) = \frac{1}{\sqrt{\pi}} \int_{\infty}^{\infty} \frac{e^{s^2}}{s - \xi} ds; \phi_{\pm} = A\xi_{\pm} \mp \frac{\Omega_{\alpha}}{k_{||} u_{||}}; \xi_{\pm} = \frac{\omega \pm \Omega_{\alpha}}{k_{||} u_{||}}; A = \frac{T_{\perp}}{T_{||}}.$$

Where $Z(\xi_n)$ is the dispersion function defined for Maxwellian plasmas [66], and ξ_n is the ratio between the phase velocity of the electromagnetic wave and the parallel thermal speed of the species α. In addition, A represents the temperature anisotropy, and ϕ_n includes an additional term to ξ_n, divided by the temperature anisotropy.

In addition, for the Olbertian kappa distribution, the computation of the same elements leads to

$$\chi_{\pm} = \frac{\omega_{p\alpha}^2}{4\pi\omega^2} \left(A + \phi_{\pm} Z_{\kappa}(\xi_{\pm}) + 1 \right). \tag{4.8}$$

On the other hand, the same elements but for the Modified kappa distribution are

$$\chi_{\pm} = \frac{\omega_{p\alpha}^2}{4\pi\omega^2}\left(A + \phi_{\pm\kappa} Z_\kappa(\xi_{\pm\kappa}) + 1\right). \tag{4.9}$$

where

$$\phi_{\pm\kappa} = \left(\frac{\kappa}{\kappa - 3/2}\right)^{1/2} \phi_{\pm}; \xi_{\pm\kappa} = \left(\frac{\kappa}{\kappa - 3/2}\right)^{1/2} \xi_{\pm},$$

$$Z_\kappa = \frac{\Gamma(\kappa)}{\sqrt{\pi\kappa}\Gamma(\kappa - 1)} \int_{-\infty}^{\infty} \frac{dt}{(t - \xi)(1 + \frac{t^2}{\kappa})^\kappa}.$$

It is worth noting that here we have used a modified definition of the kappa dispersion function $Z_\kappa(\xi_n)$ in the Olbertian and Modified distribution cases [67–69]. See appendix A for more details on the deduction of these tensors in the distribution cases shown above.

4.2 Review of electromagnetic fluctuations in magnetized plasma

To obtain an analytical expression for the electromagnetic fluctuations, we consider a periodic perturbation δh_μ in a magnetized electron-proton plasma [70, 71]. Here, μ represents a component of a Cartesian coordinate system $\{i, j, k\}$. Initially, the plasma system is neutral and current-free.

$$f_\alpha = \sum_\alpha F_\alpha. \tag{4.10}$$

Here, f_α is the sum of the distribution function of all plasma species α. By considering the perturbation in the distribution and retaining only first-order terms, we obtain

$$f_\alpha = f_{\alpha 0} + \delta h_\mu \frac{\partial f_{\alpha 0}}{\partial H_\mu}, \tag{4.11}$$

The component of the kinetic energy in the direction μ is denoted by H_μ, hence sum over μ direction is implicit.

$$\delta h_\mu \frac{\partial f_{\alpha 0}}{\partial H_\mu} = \delta h_i \frac{\partial f_{\alpha 0}}{\partial H_i} + \delta h_j \frac{\partial f_{\alpha 0}}{\partial H_j} + \delta h_k \frac{\partial f_{\alpha 0}}{\partial H_k}. \tag{4.12}$$

Taking the statistical average of a component of the disturbed electric field gives us,

$$\langle \delta E_i(t) \rangle = \frac{\int \delta E_i(t) \left(f_\alpha(H_0) + \delta h_\mu \frac{\partial f_\alpha}{\partial H_\mu}\right) dv}{\int \left(f_\alpha(H_0) + \delta h_\mu \frac{\partial f_\alpha}{\partial H_\mu}\right) dv}. \tag{4.13}$$

It is worth noting that initially there was no disturbance, hence $\langle \delta E(t) \rangle = 0$. This must be considered in 4.13. Again, we only retain only first-order terms of 4.13. Besides, to obtain the spectra of electromagnetic fluctuations, we perform the Fourier-Laplace transform of the quantities in 4.13, leading to

$$\langle \delta E_{i(\mathbf{k},\omega)} \rangle = \frac{\int \delta \hat{E}_i^* \delta \hat{h}_\mu \frac{\partial f_\alpha}{\partial H_\mu} dv}{\int f_\alpha dv}. \tag{4.14}$$

Here, we define Fourier-Laplace transformed quantities with a hat, such as $\delta \hat{E}_i := \delta E_{i(\mathbf{k},\omega)}$ and $\delta \hat{h}_\mu := \delta h_{\mu(\mathbf{k},\omega)}$. In addition, $()^*$ means the complex conjugate expression.

The source of energy for the perturbation is believed to be the stochastic motion of charges. When the charges have sufficient kinetic energy, their motion generates fields that are then absorbed by other charges [25, 54]. As a result, the perturbation is

$$\delta \hat{h}_\mu = -\frac{i}{2\omega} \delta \hat{J}_\mu \delta \hat{E}_i. \tag{4.15}$$

In addition, the linear kinetic theory relates the disturbed current density to the perturbation of the electric field in the computation of the dispersion tensor (see Appendix A). Thus, the following relation holds,

$$\langle \delta \hat{E}_i \rangle = \frac{4\pi \delta \hat{J}_\mu}{\omega^2} \Lambda_{i\mu}^{-1}. \tag{4.16}$$

In addition, the term $\delta \hat{J} \mu$ is arbitrary since it represents the source of the spontaneous emissions. Therefore, we assume that it depends only on the initial conditions of the plasma system. With this assumption, the linear response of magnetized plasmas is non-dependent on the disturbance $\delta \hat{J} \mu$. By merging Eqs. 4.14, 4.15, and 4.16, we obtain

$$\frac{\int \delta \hat{E}_\mu \delta \hat{E}_i^* \frac{\partial f_\alpha}{\partial H_\mu} dv}{\int f_\alpha dv} = \frac{8\pi}{i\omega} \Lambda_{i\mu}^{-1}. \tag{4.17}$$

It's worth noting that the electric field fluctuations $\delta \hat{E}_\mu \delta \hat{E}_i^*$ in the last expression depend explicitly on the inverse of the dispersion tensor elements. As a result, it's expected that fluctuations will be enhanced around the plasma's dispersion modes.

Considering only waves propagating parallel to the background magnetic field in equation 4.17 ($\pm = \mu = i$ and $\Lambda_{ij} = \delta_{i\mu} \Lambda_\mu$, where δ_{ij} is the Kronecker delta), and adding the same expression with its conjugate leads to,

$$\frac{\int \delta \hat{E}_\mu^2 \frac{\partial f_\alpha}{\partial H_\mu} dv}{\int f_\alpha dv} = \frac{8\pi}{i(\omega + \omega^*)} (\Lambda_\mu^{-1*} - \Lambda_\mu^{-1}). \tag{4.18}$$

We are only computing transverse electric field fluctuations because, under the given system conditions, $\langle \delta B_{||}^2 \rangle = 0$. For velocity distributions, such as the Maxwellian

and the kappa models, the fluctuating electric field can be expressed in integral form as

$$\frac{\int \delta\hat{E}_{\mu}^{2}\frac{\partial f_{\alpha}}{\partial H_{\mu}}dx}{\int f_{\alpha}dx} = -\alpha_{\mu}\langle\delta\hat{E}_{\mu}^{2}\rangle. \tag{4.19}$$

Where α_{μ} is a scalar function to be determined by macroscopic parameters of the distribution in the direction μ. Hence, for these kappa interpretation models or Maxwell-distributed plasmas, we obtain,

$$\langle\delta\hat{E}_{\mu}^{2}\rangle = \frac{8\pi}{i\alpha_{\mu}(\omega+\omega^{*})}(\Lambda_{\mu}^{-1*} - \Lambda_{\mu}^{-1}). \tag{4.20}$$

As an example, we compute the $\alpha_{\perp}$ scalar function in the Maxwell anisotropic distribution case,

$$F_{Mx\alpha} = \frac{1}{\pi^{3/2}\theta_{\alpha\perp}^{2}\theta_{\alpha||}}e^{\left(-\frac{v_{\perp}^{2}}{\theta_{\alpha\perp}^{2}}-\frac{v_{||}^{2}}{\theta_{\alpha||}^{2}}\right)}. \tag{4.21}$$

The change in kinetic energy in the distributions in the direction $\mu = \{\perp, ||\}$ is mediated by

$$\frac{\partial F_{Mx\alpha}}{\partial H_{\mu}} = -\frac{2}{m_{\alpha}\theta_{\alpha\mu}^{2}}\frac{1}{\pi^{3/2}\theta_{\alpha\perp}^{2}\theta_{\alpha||}}F_{M\alpha}. \tag{4.22}$$

Substituting this result into equation 4.22 yields

$$\frac{\int \delta\hat{E}_{\mu}^{2}\frac{\partial f_{\alpha}}{\partial H_{\mu}}dx}{\int f_{\alpha}dx} = -\frac{1}{k_{B}T_{\mu\alpha}}\frac{1}{\pi^{3/2}\theta_{\alpha\perp}^{2}\theta_{\alpha||}}\frac{\int dv^{3}F_{M\alpha}\delta\hat{E}_{\mu}^{2}}{\int f_{\alpha}dx} = -\frac{1}{k_{B}T_{\mu\alpha}}\langle\delta\hat{E}_{\mu}^{2}\rangle.$$

Hence, replacing $\alpha_{\mu} = 1/k_{B}T_{\mu}$ in equation 4.20, we get,

$$\langle\delta\hat{E}_{\mu}^{2}\rangle = \frac{8\pi k_{B}T_{\mu}}{i(\omega+\omega^{*})}(\Lambda_{\mu}^{-1*} - \Lambda_{\mu}^{-1}). \tag{4.23}$$

From the equation above, we can calculate the magnetic field fluctuations using the Ampére-Faraday laws, such that

$$\langle\delta\hat{B}_{\mu}^{2}\rangle = \eta_{||}^{2}\frac{8\pi k_{B}T_{\mu}}{i(\omega+\omega^{*})}(\Lambda_{\mu}^{-1*} - \Lambda_{\mu}^{-1}). \tag{4.24}$$

Here $\eta_{||}$ corresponds to the wave refraction index. It is worth noting that this last equation is consistent with the results in the references [15, 41, 42, 53, 70–72].

Then, using equation 4.24 (see Appendix B and references [70, 71] for more details), we can compute the transverse magnetic fluctuations of the electromagnetic cyclotron mode. In the case of equilibrium thermal conditions, we obtain

$$\frac{1}{8\pi}[\langle|B_{\perp}|^{2}\rangle_{\alpha}] = \eta^{2}\frac{k_{B}T_{\perp\alpha}}{\omega\lambda_{\perp}}\cdot Im\left[\frac{4\pi\chi_{\perp\alpha}}{\Lambda_{\perp}}\right]. \tag{4.25}$$

Here, $[\langle|B_\perp|^2\rangle_\alpha]$ corresponds to the magnetic fluctuations of species alpha in the continuum spectra of frequency and wave number. In this expression, $\lambda_\perp$ represents the transverse element of the dispersion tensor in vacuum. Besides, $\chi_{\perp\alpha}$ represents the transverse electric susceptibility element, and $\Lambda_\perp$ represents the dispersion tensor element of species alpha. In addition, the analytical expression for the Olbertian case is

$$\frac{1}{8\pi}[\langle|B_\perp|^2\rangle_\alpha]_{\kappa_\alpha} = \eta^2 \frac{\kappa_\alpha - 1}{\kappa_\alpha - 3/2} \cdot \frac{k_B T_{\perp\alpha}}{\omega\lambda_\perp} \cdot Im\left[\frac{4\pi\chi_{\perp\alpha}}{\Lambda_\perp}\right]_{\kappa_\alpha - 1}. \tag{4.26}$$

The kappa Modified case also has a κ index subscript, indicating kappa-dependent spectra of magnetic fluctuations. Later, we will demonstrate that the shape and intensity of the spectra depend highly on this value in different ways for both interpretations of kappa distributions, even with the same thermal speed.

For the Modified case, the spectra of magnetic fluctuations are given by

$$\frac{1}{8\pi}[\langle|B_\perp|^2\rangle_\alpha]_{\kappa_\alpha} = \eta^2 \frac{\kappa_\alpha - 5/2}{\kappa_\alpha - 3/2} \cdot \frac{k_B T_{\perp\alpha}}{\omega\lambda_\perp} \cdot Im\left[\frac{4\pi\chi_{\perp\alpha}}{\Lambda_\perp}\right]_{\kappa_\alpha - 1}. \tag{4.27}$$

With these results we will discuss in the next chapter about differences and similitudes in the parallel electromagnetic dispersion branch and the associated fluctuating electromagnetic spectra.

Chapter 5

Results from linear kinetic theory and electromagnetic fluctuations

With the kinetic theory results from the previous chapter, we will review the behavior of parallel modes propagating along the background magnetic field. These modes become particularly relevant in plasmas that are out of equilibrium because, under certain macroscopic parameter configurations such as temperature anisotropy or beta values, they can significantly impact the plasma's stability.

We compute the dispersion relation in the case of the Maxwell and both kappa velocity distribution models in figure 5.1. We analyzed a simple set of macroscopic parameters ($\beta = \{0.01, 0.1, 1\}$, $A = T_\perp/T_{||} = 1$, $\kappa = \{3, 10\}$) and found the electron whistler cyclotron mode in a quasi-stationary regime under isotropic temperature conditions. Since all macroscopic parameters have the same values for electrons and protons, we have omitted the α subscript.

The dispersion branches for different β values are shown in the top panel of figure 5.1. We observe that the kappa (dotted and dashed) and Maxwellian (solid) distribution dispersion relation results for each beta value are similar in the respective low frequency and wave number configurations. Each dispersion branch, on the other hand, begins to separate from the others at smaller spatial scales (as shown in the subpanels where each branch diverges from the others, this happens for larger wave numbers and for smaller beta values). Therefore, non-thermal effects become more relevant for smaller scales. This is due to the presence of suprathermal electrons (and the accumulation of low energy population in the case of the modified kappa model), which affects the stationary regime of the wave in different ways.

In addition, the bottom panel shows the growth rate for all cases mentioned before. For all β values, the original kappa have almost the same stationary regarding the respective equilibrium limit ($\kappa \to \infty$). Still, the damping rate becomes softer for

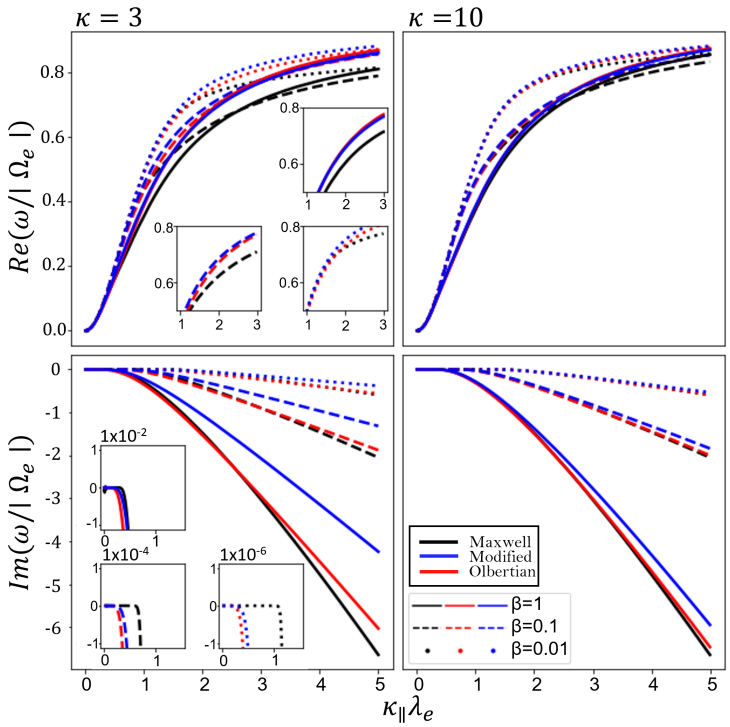

Figure 5.1: The top panel shows the dispersion branches of the whistler-cyclotron mode for the ratio of electron plasma frequency to gyro-frequency, $\omega_{pe}/|\Omega_e| = 5$ (similar results are obtained for higher frequency ratios [42]). Besides, the wavenumber is normalized to the electron inertial lenght. We considered two non-thermal scenarios, with $\kappa = 3, 10$, and three different plasma beta values, $\beta = 0.01, 0.1, 1$. The bottom panel shows the corresponding growth rates of the dispersion branches. We have also included subpanels where the dispersion branches separate in a specific wave number and where the growth rates represent a quasi-stationary regime of the wave.

the larger wave number values. A large density of suprathermal electrons interact via electromagnetic resonance with the wave in this range.

Interestingly, for the Modified kappa case, the growth rates are even lower for larger wavenumbers compared to the Olbertian and equilibrium cases for the entire range of κ and β configurations considered. As the wave number decreases, each branch separates from the others, and in the Modified kappa case, the frequencies are higher compared to the Olbertian and Maxwell cases, before the separation occurs at $k_{||}\lambda_e \simeq 2$. (see $\kappa = 3$ and $\beta = 0.01$ configuration on Fig. 5.1). These properties are attributed to the high density of electrons with low velocities, rather than the suprathermal population. This is evidenced by the differences in dispersion behavior when comparing the Olbertian and Maxwell distribution results.

It is worth noticing that the features described above about the damping rate are even more remarkable in the lowest kappa value case ($\kappa = 3$) and the larger beta value configuration ($\beta = 1$). Besides, as expected in the equilibrium case, when the β value decrease, the stationary state ($Im(\omega) = 0$) is broader in the wave number range ($0 < k_{||}\lambda_e < 1$) because of a rigid magnetic power governing the plasma. In addition, with an increment of the κ value, both kappa results recover almost the same trend in the dispersion branch and growth rates of the Maxwell case.

5.1 Whistler cyclotron and firehose mode driven by temperature anisotropies

In this study, we show temperature anisotropies and their influence on magnetic fluctuations. We compute quasi-unstable transverse collective modes with $Im(\omega) > 0$ for two temperature anisotropy configurations, $A = 0.8$ and $A = 1.2$. These values correspond to threshold values measured in the solar wind at 1 AU from the Sun [73]. This temperature anisotropy scenario breaks the symmetry of the velocity field, generating instabilities ($Im(\omega) > 0$) such as whistler-cyclotron ($A < 1$) or firehose ($A > 1$) modes. Even though these instabilities exist in a range of β and κ configurations, the firehose case becomes relevant for a higher beta value [3, 42].

In Figure 5.2, on the top panel, we present the dispersion relation of the firehose mode. It is noticeable that each dispersion branch separates from the others more significantly compared to the isotropic case (see the top-left panel of Figure 5.1 and top-left subpanels of Figure 5.2). Due to the temperature anisotropy value $A = 0.8$, is expected an enhanced contribution of the non-thermal effects from suprathermal electrons for larger wave numbers. Moreover, for this anisotropy configuration, we observe a pronounced divergence in the curves from the stationary regime of all distribution models compared to the isotropic temperature case. This highlights the significant destabilizing contribution from suprathermal electrons in the larger wave number regime, where free energy from anisotropy is available. However, all the other features described in the isotropic case remain conserved.

Figure 5.3 displays the dispersion relation of the whistler cyclotron mode for a temperature anisotropy of $A = 1.2$, with the same κ and β parameters as Figure 5.1.

As shown in the top panel of figure 5.3, we compute the whistler-cyclotron dispersion relation branch for each κ and β value. For this plasma collective mode configuration, the dispersion relation of both kappa distributions seems to have a similar trend. They are similar to what occurs in the temperature anisotropy configurations of $A = 0.8$ and $A = 1$ (see figures 5.1, 5.2, and 5.3).

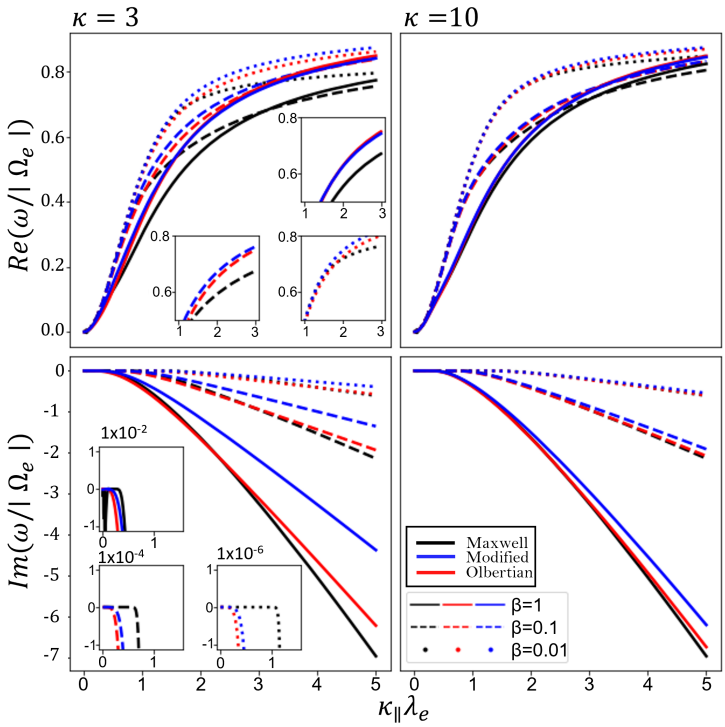

Figure 5.2: Top panel represents dispersion branches of the firehose wave mode for $\omega_{pe}/|\Omega_e| = 5$ and the temperature anisotropy configuration, $A = 0.8$. We use the same κ and β configuration of figure 5.1. Also, the same color code of figure 5.1 was used. The bottom panel represents the corresponding growth rate of the dispersion branches for each case. The subpanels indicate where the dispersion properties diverge when each distribution model is used.

Soft changes in anisotropy result in similar dispersion branches for this collective mode across all distribution models, consistent with previous findings [33, 74]. To further analyze the dispersion behavior, we also computed the growth rates for the different distribution models in the bottom panel of Figure 5.3. For this temperature anisotropy configuration, we observed differences between the Olbertian (red) and Modified (blue) distributions in terms of positive growth rates ($Im(\omega) > 0$).

In the scenario where $\kappa = 3$, we observe that in the larger space scale configuration, the maximum growth rate of this mode is proportional to $Im(\omega) = \{10^{-6}, 10^{-4}, 10^{-2}\}$ for the corresponding beta values $\beta = \{0.01, 0.1, 1\}$. As the plasma becomes highly magnetized, *i.e.*, β values decrease, the Maxwell distribution has a broader range of wave numbers where this mode remains stable. Conversely, as β values increase, the stable range in thermal equilibrium narrows down sufficiently to approach the wavelength range where this mode becomes quasi-stable or unstable in both kappa distributions.

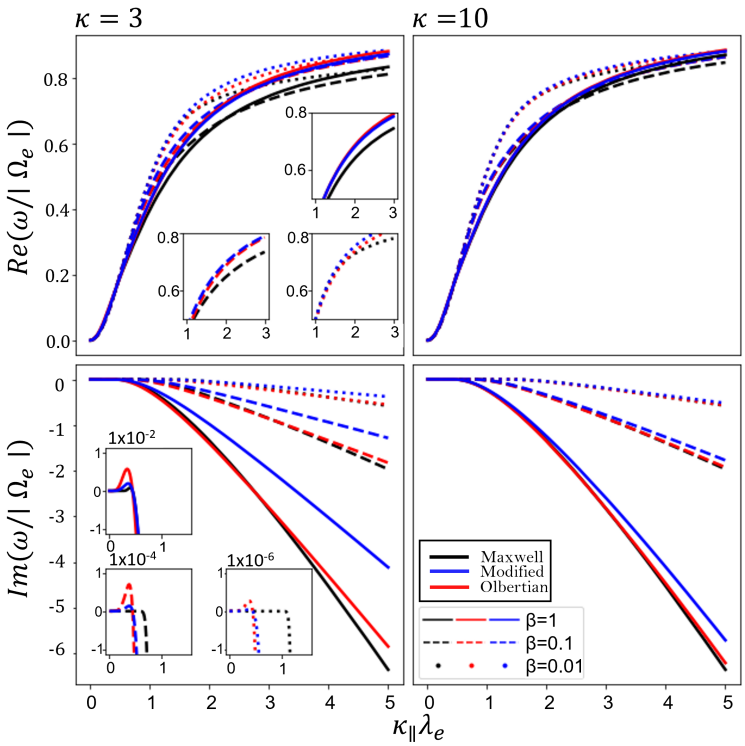

Figure 5.3: In the top panel is dispersion relations for the whistler-cyclotron wave in the case of $A = 1.2$ configuration, and in the bottom panel are the respective growth rates. The rest of the parameters and color codes are equal to figure 5.1. The subpanels indicate positive growth rates for each beta value.

Even for $\beta = 1$, for the Maxwell equilibrium case, the stationary regime becomes unstable ($Im(\omega) > 0$) in the same wavelength range of both kappa distribution interpretations. Besides, the growth rate in the Olbertian case is always more significant than in the Modified case. This suggests that the larger population of suprathermal electrons described by the Olbertian distribution interacts with this dispersion branch monotonously. On the other hand, the smaller amount of suprathermal population of the Modified distribution and the enhanced amount of particles with low velocity leads to smaller growth rates.

However, as the kappa value increases, this non-thermal effect tends to disappear, resulting in growth rates similar to the equilibrium case in both kappa distributions. While the differences mentioned above may be considered minor in guiding the discernment of plasmas out of equilibrium by both kappa models, analyzing the continuum spectra of magnetic fluctuations will reveal more significant differences.

5.2 Results of electromagnetic fluctuations in magnetized plasmas with kappa distributions

This section shows the differences in the continuum spectra of magnetic fluctuations wrapping the plasma dispersion modes described above.

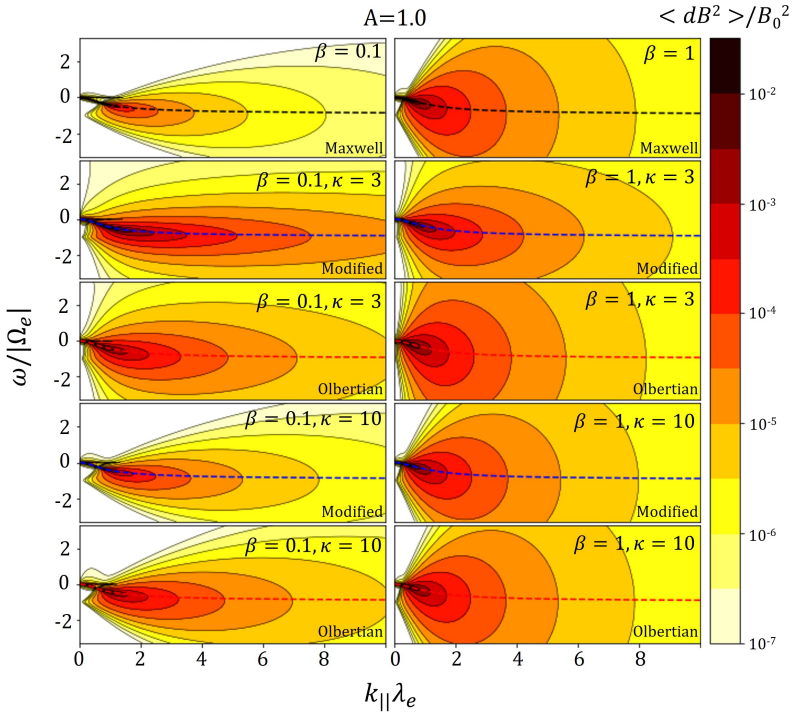

Figure 5.4: The figure shows normalized spontaneous magnetic fluctuations with respect to the mean value of the background magnetic field, plotted in terms of normalized wavenumber and frequency. Here, λ_e represents the electron inertial length and Ω_e is the electron cyclotron frequency. The left column corresponds to low β cases, while the right column corresponds to high β cases. The intensity of the magnetic fluctuations is represented by a logarithmic scale color bar. Each row shows the results for one of the three distributions with variations in the κ value, and the dashed curves indicate the dispersion branch of the transverse electromagnetic mode for each distribution case. The color code used for the dispersion results is consistent with Figure 5.1, where Maxwell is represented by black, Olbertian by red, and Modified by blue.

In Figure 5.4, we show thermal (Maxwell) and non-thermal (kappa) equilibrium magnetic fluctuations from lower to higher $\beta = \{0.1, 1\}$ and $\kappa = \{3, 10\}$ configuration. Besides, we plot the whistler-cyclotron branch in a dashed curve for each case with its typical frequency regime $\Omega_p < \omega < \Omega_e$. We found high-intensity spectra of magnetic fluctuations surrounding the whistler cyclotron branch. At first glance, we

can see that the spectrum of fluctuations becomes broader in Fourier space around the whistler branch for both kappa distributions compared to the thermal equilibrium distribution results in the first row.

This is due to the stochastic motion of high-energy charges, which reaches a larger frequency and wave number range, leading to the spreading of magnetic fluctuations compared to the equilibrium case. We have shown this in Figure 5.1, in which each kappa dispersion branch separates from the Maxwellian one for larger wave numbers and frequencies. Hence, the shape of the spectra is related to the wave dispersion branch, and different non-thermal distributions lead to different intensities and shapes of magnetic fluctuations.

For the Modified case, we observe that the high density of low-energy electrons tends to distribute the high intensity of magnetic fluctuations around the whistler branch. In contrast, the Olbertian case shows a broader spectrum of fluctuations (see the left column of Figure 5.4 for $\kappa = 3$). Additionally, in the same column, we can see that due to the enhanced suprathermal electron population, the Olbertian case for $\kappa = 3$ produces a spectrum similar to the Modified case, but with high-energy electrons spreading uniformly magnetic fluctuations to larger frequencies.

Even though all distribution cases share the same thermal speed in the low beta regime, where a strong background magnetic field balances the destabilizing effects of the suprathermal population, this feature still holds. We can compare these results with what we have shown in Figure 5.1, where keeping the lowest beta regime leads to similar damping rates and dispersion branches of the collective mode. Looking at the continuum spectra of these modes reveals hidden information about magnetized suprathermal electrons. Furthermore, in the last two rows of the first column in Figure 5.4, we show a higher kappa value selection, which almost recovers the shape of thermal equilibrium whistler cyclotron fluctuations in both kappa cases. However, there is a slight difference in intensity values between them and also with respect to the Maxwell case.

In the right column, the intensity of fluctuations increases with higher beta value selection ($\beta = 1$). The spectra obtained from all distribution cases shift the peak of magnetic fluctuations towards a smaller wavelength regime in this β regime. It's worth noting that the equilibrium case will always have the most prominent peak intensity of fluctuations for smaller wavelengths than both kappa interpretations.

Moreover, we can obtain the decay of magnetic fluctuations in term of the frequency ω by integrating over the entire wave number spectrum (refer to Figure 5.5). It's worth noting that at $\omega/|\Omega_e| = 1$, the curves exhibit fluctuations caused by the resonance of electrons with the first multiple of the cyclotron frequency.

In Figure 5.5, we present the results for reduced magnetic fluctuations energy for

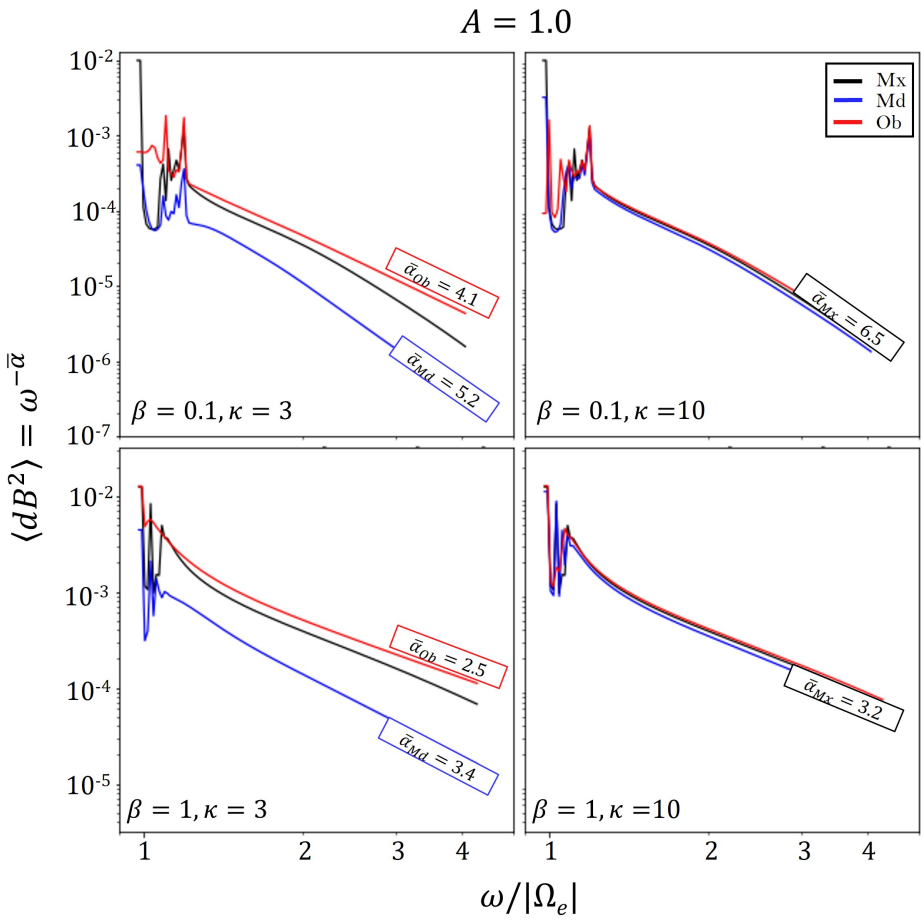

Figure 5.5: Reduced magnetic energy in terms of frequency, $\langle \delta B^2 \rangle_\omega = \omega^{-\bar{\alpha}}$, is shown for each velocity distribution case. These results were obtained by integrating over the wave number of all fluctuating magnetic spectra shown in Figure 5.4. The black curve corresponds to the Maxwell thermal equilibrium case, while the blue and red curves represent the non-thermal Modified kappa and Olbertian kappa cases, respectively. As the reduced energy decays as a power law $\omega^{-\bar{\alpha}_i}$, we plotted the decay index for each curve, where $i \in \{M_x, M_d, O_b\}$ corresponds to the Maxwell, Modified, and Olbertian cases, respectively.

the Modified, Olbertian, and Maxwell distributions. For both kappa distributions, the decay in frequency shows a steep slope in the Modified case for the $\kappa = 3$ configuration, while for the Olbertian case, the decay slope is softer. This difference is due to rigid spectra of magnetic fluctuations in the Olbertian case, supported by a larger density of suprathermal electrons that spread enhanced electromagnetic fluctuations towards larger frequency values. Therefore, the decay of magnetic fluctuations in the Olbertian case is slower than that of the Modified case. We

explain the slower decay as a result of the lower power value decay ($\langle dB^2 \rangle_\omega = \omega^{-\bar{\alpha}_i}$).

For magnetized plasmas with $\beta = 0.1$, both kappa distribution cases show a lower index decay slope than the equilibrium case. As we increase to $\beta = 1$, we observe a larger α value for the Modified case and a lower value for the same index in the Olbertian case. This is expected since the Modified case has a higher intensity of fluctuations for frequencies relative to the whistler-cyclotron mode. Moreover, as we increase the kappa value to $\kappa = 10$, both kappa results follow the equilibrium decay with almost the same slope.

5.3 Difference in the complete spectra of magnetic fluctuations for both kappa distributions

We can identify similarities and differences in the complete spectra of each velocity distribution case by subtracting them. This comparison allows us to understand the spectrum disturbance caused by non-thermal species by directly comparing these kappa results with the ideal Maxwell equilibrium case. Therefore, we present an analysis of subtracting fluctuating magnetic spectra between each distribution case.

In the first column of Figure 5.6, we show the subtraction of the Olbertian-Modified spectra. Near the whistler-cyclotron branch (white tones), both spectra of fluctuations are similar, but the Olbertian case has higher intensities (reddish tones). Beyond the frequencies of the whistler-cyclotron dispersion branch, the red color indicates an increased power of magnetic fluctuations provided by the Olbertian spectra case. As we showed in highly magnetized plasmas with $\kappa = 3, 10$ configurations, the pronounced red tone over the Fourier domain indicates the crucial role of suprathermal particles. This means that the high intensity of fluctuations is distributed with a more homogeneous feature than the Modified case.

In addition, we computed the subtraction of both kappa spectra in the middle and last column with the respective equilibrium case ($\kappa \to \infty$). In the second column of Figure 5.6, the red color predominating in a triangular area denotes the zone wherein thermal-equilibrium fluctuations are more intense than in the Modified kappa case. This triangle emerges from the first multiple of the cyclotron frequency at near-zero wave number, spreading over the Fourier domain, which is bounded by a blue color. This indicates that the Modified case of whistler fluctuation predominates for higher-frequency configurations. This result is expected by the larger velocities reached by the small number of suprathermal electrons that can spread magnetic fluctuations in this frequency regime.

In contrast, in the last column, blue indicates the predominance of the intense

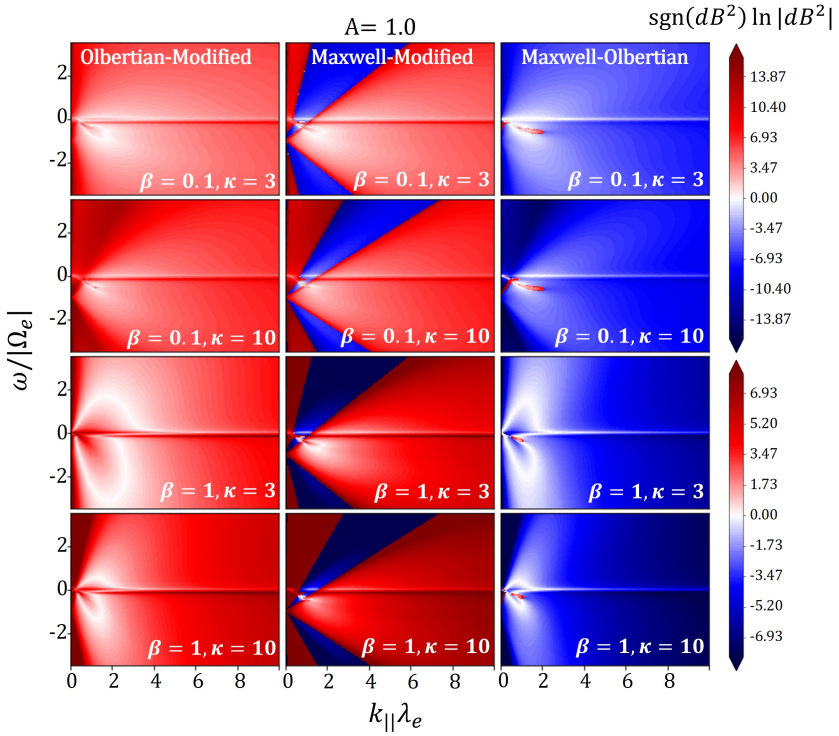

Figure 5.6: The left column shows the subtracted fluctuating magnetic spectrum for both kappa distributions. The middle column represents the subtraction between the Maxwell and Modified kappa cases, and the last column shows the subtraction between the Maxwell and Olbertian kappa cases. The two top rows show the results for the $\beta = 0.1$ configuration and $\kappa = \{3, 10\}$, while the two bottom rows are for the $\beta = 1$ configuration and $\kappa = \{3, 10\}$. The remaining parameters are the same as in Figure 5.4. The color bar indicates the predominant region for each spectrum, calculated as $sgn(dB^2_{i-j})|ln(|dB^2_{i-j}|)|$, where $i, j \in \{M_x, M_d, O_b\}$. The red and blue colors indicate where the intensity of fluctuations is predominant for each spectrum in the Fourier domain. Additionally, λ_e and Ω_e correspond to the electron inertial length and the electron cyclotron frequency, respectively.

Olbertian spectrum. Here, the red triangle shape of thermal fluctuations from the Maxwell distribution does not appear, and instead, the rest of the spectrum shows a slight red color around whistler fluctuations (predominance of the Maxwell case). This is an expected result because the Maxwell case has a small area in the Fourier domain to distribute the energy of the magnetic fluctuations. Moreover, the enhancement of electromagnetic fluctuations in practically the whole spectrum of fluctuations provided by the Olbertian case is evident. This feature is due to the high density of the suprathermal population available to generate electromagnetic fluctuations over a wider frequency domain.

In the last two rows of Figure 5.6, we present a similar comparative scheme, but for $\beta = 1$. Here, the logarithmic color scale is on a narrower range due to the high thermal energy of the plasma controlling its behavior. Moreover, the same analysis used for $\beta = 0.1$ can be applied to $\beta = 1$, except that all magnetic spectra subtraction structures become broader. In particular, the triangle shape in the middle column is wider and has more red tones, indicating a greater difference in the spectra of electromagnetic fluctuations.

5.4 Differentiation between the interpretation of both kappa distributions in energy results

In this section, we compute the total energy of magnetic fluctuations by integrating magnetic fluctuations in the frequency and wave number domain. The left panel of Figure 5.7 shows the energy of magnetic fluctuations respect to the κ value over different β values. Considering $\kappa/(\kappa - 3/2) = 1$, we recover the thermal equilibrium energy case. Comparing Olbertian's total magnetic spectra energy (red color) with the thermal equilibrium case, we show that total magnetic energy gets enhanced with decreasing kappa value.

In contrast, the suprathermal character of the Modified case (blue curves) does not share this feature and shows even less energy toward kappa value decrement. The enhanced narrow core of the distribution with decreasing kappa value supports this low magnetic spectral energy in the Modified case. Also, low density in suprathermal tails is insufficient to compensate for the effects of the low-energy core. Hence the small number of suprathermal particles contributes poorly to the energy of magnetic fluctuations, even compared with the Maxwell equilibrium case.

In the right panel, we present the decay power index for each non-thermal distribution interpretation and the ideal equilibrium case. For $\beta = 0.1$, we observe that the decay of both kappa spectra becomes softer as κ values decrease. On the other hand, for the $\beta = 1$ scenario, the kappa Modified index decay becomes larger as κ values decrease. However, the decay index results obtained from the Olbertian distribution do not follow this trend, indicating the rigid quality of electromagnetic fluctuations out of thermal equilibrium. Furthermore, for $\beta = 1$, we observe that as κ values decrease, the α index of the power law decay becomes larger even when compared to the index computed at equilibrium. This is an expected result due to the non-thermal features becoming more evident with larger beta values and the resonance scenario from the results shown in Figure 5.4 for the Modified case.

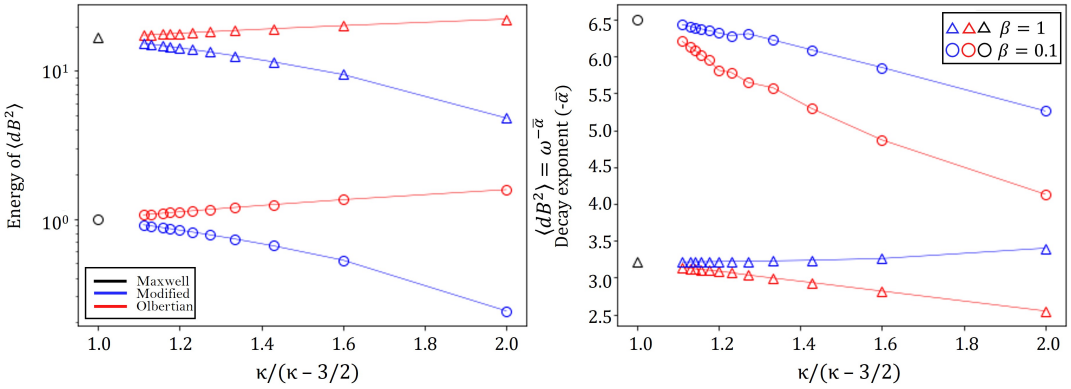

Figure 5.7: The left panel shows the total energy of magnetic fluctuations for each velocity distribution case analyzed in different β regimes, presented in terms of $\kappa/(\kappa - 3/2)$. In this function, the limit $\kappa \to \infty$ tends to $\kappa/(\kappa - 3/2) = 1$, recovering the thermal equilibrium case. The entire energy spectrum shown is normalized to the Maxwell case in the configuration $\beta = 0.1$. The right panel displays the index of the power-law decay, $\langle dB^2 \rangle = \omega^{-\bar{\alpha}}$, for each case. The $\bar{\alpha}_i$ index is the same as in Figure 5.5, but for additional κ cases. The black marker represents the Maxwell distribution result, while the red and blue markers represent the Olbertian and Modified distribution results, respectively.

5.5 Review of the ratio of the electron plasma frequency to gyro frequency

Motivated by different space plasma scenarios, we turn our analysis to the ratio of the plasma frequency to the gyro frequency. Here, we compute the total energy of the fluctuating spectra for all distribution cases in terms of the parameter $P = \omega_{pe}/|\Omega_e|$. In figure 5.8, the first row shows the energy cases for the Olbertian distribution, where decreasing κ for any P value results in higher energy levels. This feature is shared for both β values showed in here.

It is worth noting that each P result was separated from the others by adding a constant. This was intentionally made to evidence differences or similitudes because there are no significant changes in energy toward variations in P. In the second row of Figure 5.8, we present the energy cases for the Modified distribution. In both β values ($\beta = 0.1$ and $\beta = 1$), we observe a decrease in energy as κ decreases. These results suggest that P is not a parameter that enables us to distinguish the spectra generated by these distributions.

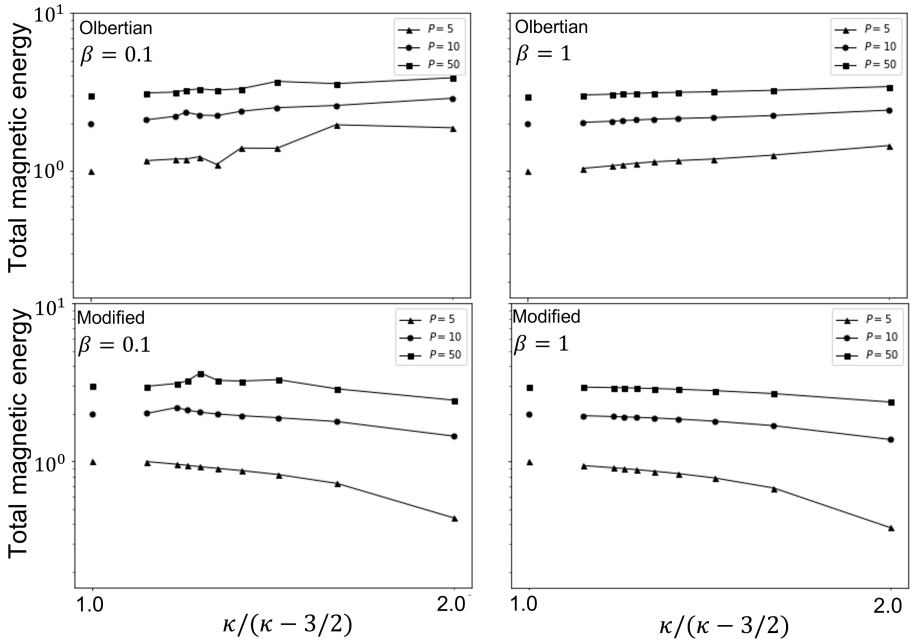

Figure 5.8: The top panels show the total energies of Olbertian magnetic fluctuations for different $P = \omega_{pe}/\Omega_e$ values, where ω_{pe} is the electron plasma frequency, in terms of $\kappa/(\kappa-3/2)$. The bottom panels display the corresponding results for the Modified case. All energies are normalized to the $\beta = 0.1$ Maxwell case. The markers represent the total magnetic energy values for $P = \{5, 10, 50\}$.

5.6 Fluctuating magnetic spectra and temperature anisotropy values

In Figure 5.9, we also compute electromagnetic fluctuations for two temperature anisotropies values, $A = 0.8$ and $A = 1.2$.

It is worth noting that the black line at $\omega/|\Omega_e| \simeq 0$ represents electromagnetic fluctuations surrounding wave modes that become relevant for ion frequencies. The left panel shows the anisotropy case of $A = 0.8$, and the right panel shows the magnetic fluctuation spectra cases for $A = 1.2$. It is evident that in these anisotropy configurations, all magnetic spectra are enhanced and broader than the isotropic temperature case shown in Figure 5.4. Also, the shape of the spectra changes with discontinuous contour lines and levels due to the enhanced fluctuations at $\omega/|\Omega_e| \simeq 0$.

Besides, for $A = 0.8$ in the $\kappa = 3$ configuration, these spectra tend to deform even more following the dispersion branch for the negative frequency values. The equilibrium case in the first row tends to distribute magnetic fluctuations with symmetry surrounding the firehose mode. Regarding the Modified case in the second row, electromagnetic fluctuations spread with more intensity for negative frequencies,

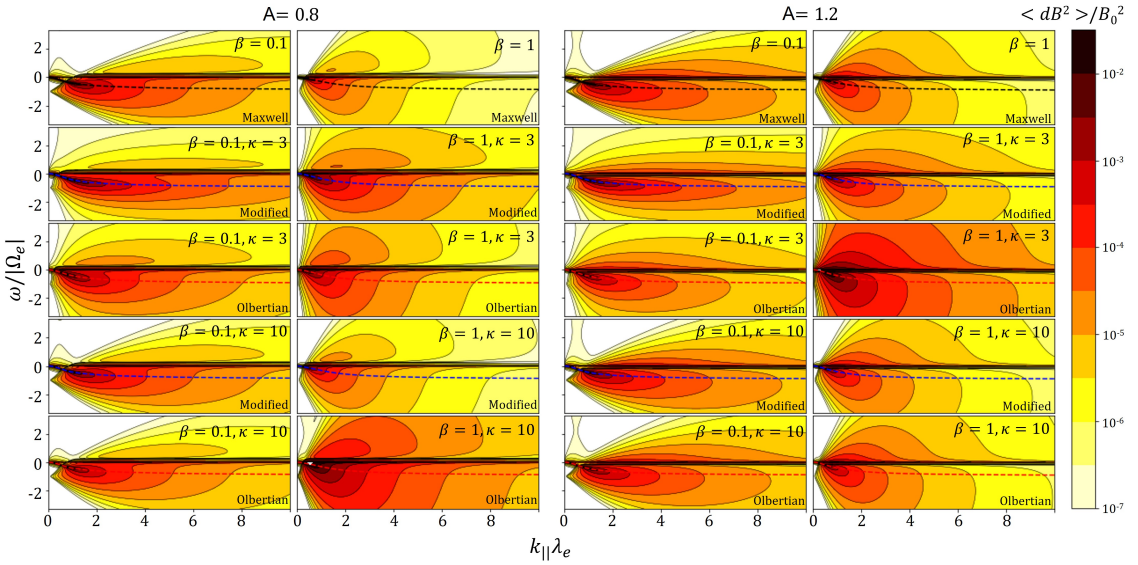

Figure 5.9: The graphs show normalized magnetic fluctuations with respect to the mean background magnetic field B_o. The first two columns display the cases for $A = 0.8$, and the last two columns are for $A = 1.2$. For each temperature anisotropy regime, the left panels show the low $\beta = 0.1$ cases, and the right panels show the $\beta = 1$ cases. The color bar is logarithmic and represents the intensity of the fluctuations. In each subpanel, we plot the fluctuating spectra of both kappa distributions and the Maxwell equilibrium case. For both kappa models, we selected two kappa values, $\kappa = 3$ and $\kappa = 10$, which are typically measured values in the non-thermal range of several space environments [10]. We also show the respective dispersion branch of Figures 5.3 and 5.2 in dashed lines.

suggesting an enhanced electromagnetic resonance feature. In the third row, for the Olbertian case, electromagnetic fluctuations spread more uniformly, similar to the equilibrium case.

In the first row of Maxwell results for $A = 1.2$, the charges spread magnetic fluctuations more symmetrically around the dispersion branch, which is a shared feature with the isotropic case (see Figure 5.4). In the second row, fluctuations are also more symmetrical around the whistler branch for the Modified case, but they are more concentrated compared to the Olbertian case shown in the third row. This suggests an enhanced electromagnetic condition for the Modified case.

In the last two rows, we plotted the $\kappa = 10$ scenario for the Olbertian and Modified cases for $A = 0.8$ and $A = 1.2$. Both kappa spectra almost recover the features of the thermal equilibrium scenario in this configuration. However, the analysis of the continuum spectra of magnetic fluctuations has more distinctive features to distinguish between the two kappa distribution results. These features were not apparent in the linear dispersion theory results.

In addition, we compute the reduced magnetic power for two anisotropy values $A = 0.8$ and $A = 1.2$.

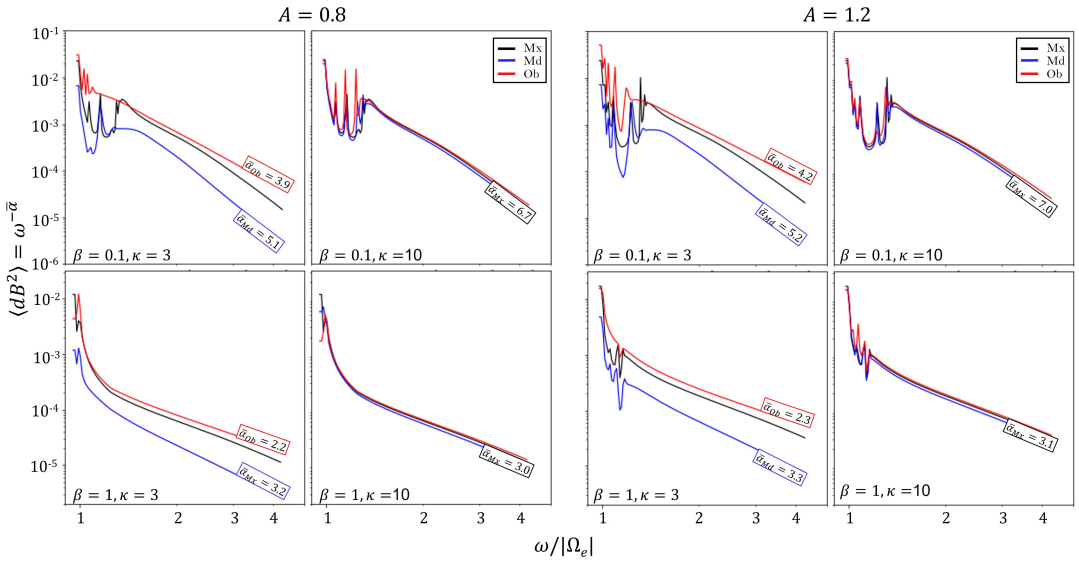

Figure 5.10: We plot the reduced magnetic energy for each velocity distribution in terms of normalized frequency, using the same parameters as Figure 5.5 for each temperature anisotropy regime ($A = 0.8$ and $A = 1.2$).

In the reduced spectra shown in Figure 5.10, the left and right panels display the anisotropy configurations $A = 0.8$ and $A = 1.2$, respectively. The β values change by row, and the κ values change by column. Generally, these temperature anisotropy configurations exhibit the same decay features described above for the isotropic case (see Figure 5.5).

It is worth noting that, in this case, the whistler-cyclotron mode is unstable. This suggests that the contribution from the suprathermal population gets enhanced for larger temperature anisotropy values. This affects the decay of the reduced magnetic power. Also, for these temperature anisotropy values when $\kappa = 10$, both kappa results tend to follow the thermal equilibrium decay. These results motivate the comparison of the total continuum spectra for all distribution cases in the following section.

5.7 Temperature anisotropy cases for the subtraction in the spectra

To review consistency across the full range of magnetic fluctuating spectra, we computed the cases of $A = 0.8$ and $A = 1.2$. Generally, we found that small changes in the temperature anisotropy values lead to results that are almost identical to those observed in the isotropic case.

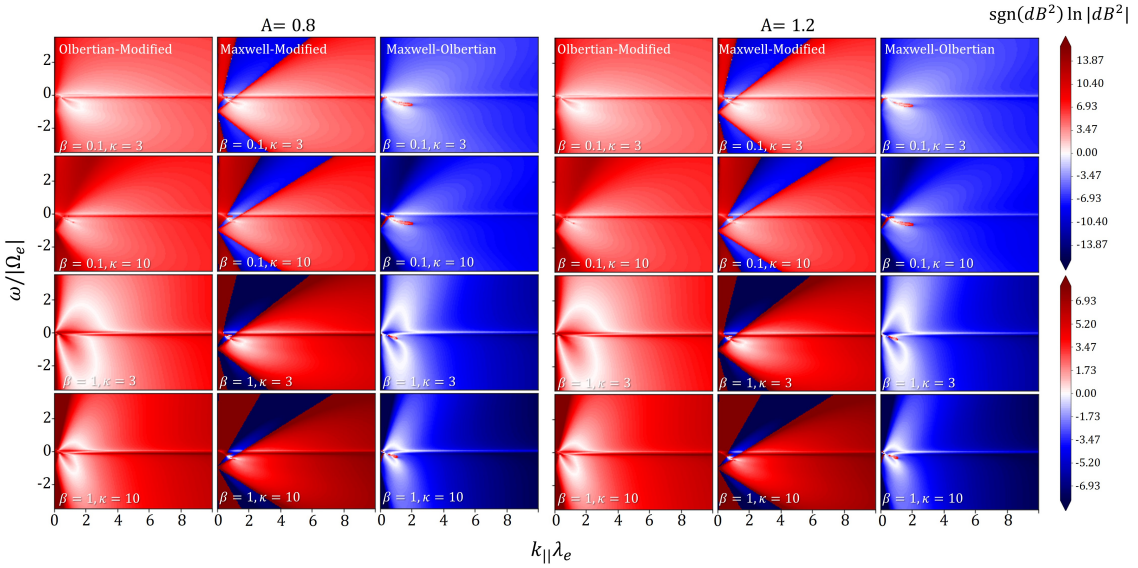

Figure 5.11: This figure shows the same normalized magnetic fluctuations as Figure 5.6, but for the $A = 0.8$ and $A = 1.2$ temperature anisotropy cases.

Considering the left and right panels of figure 5.11, we show that differences in complete spectra described for the isotropic case are preserved in the temperature anisotropic cases. These results are consistent with the ones shown in figures 5.10, where small changes in anisotropies lead to almost equal changes in the magnetic spectra. All features described in Figure 5.6 apply to these anisotropy configurations.

5.8 Energy of magnetic fluctuations in temperature anisotropy case

Here we compute the temperature anisotropy cases of the Figure 5.7. As shown above, the trend of energy in terms of a κ and β values evidence differences in the power of magnetic fluctuations in plasmas out of thermal equilibrium described with both kappa distributions.

The analysis is the same for both anisotropy regimes of $A = 0.8$ and 1.2, as shown in the left and right panels of Figure 5.12, respectively. Even though for the $A = 1.2$ regime and $\beta = 1$ scenario, we expect the whistler dispersion branch to be unstable with positive growth rates proportional to $\Omega_e = 10^{-4}$ (see Figure 5.3), this does not significantly change or influence the energy calculated for the $\kappa = 3$ value, as well as for larger values of kappa ($\kappa = 10$). Thus, this temperature anisotropy regime shares the same features as the isotropic regime.

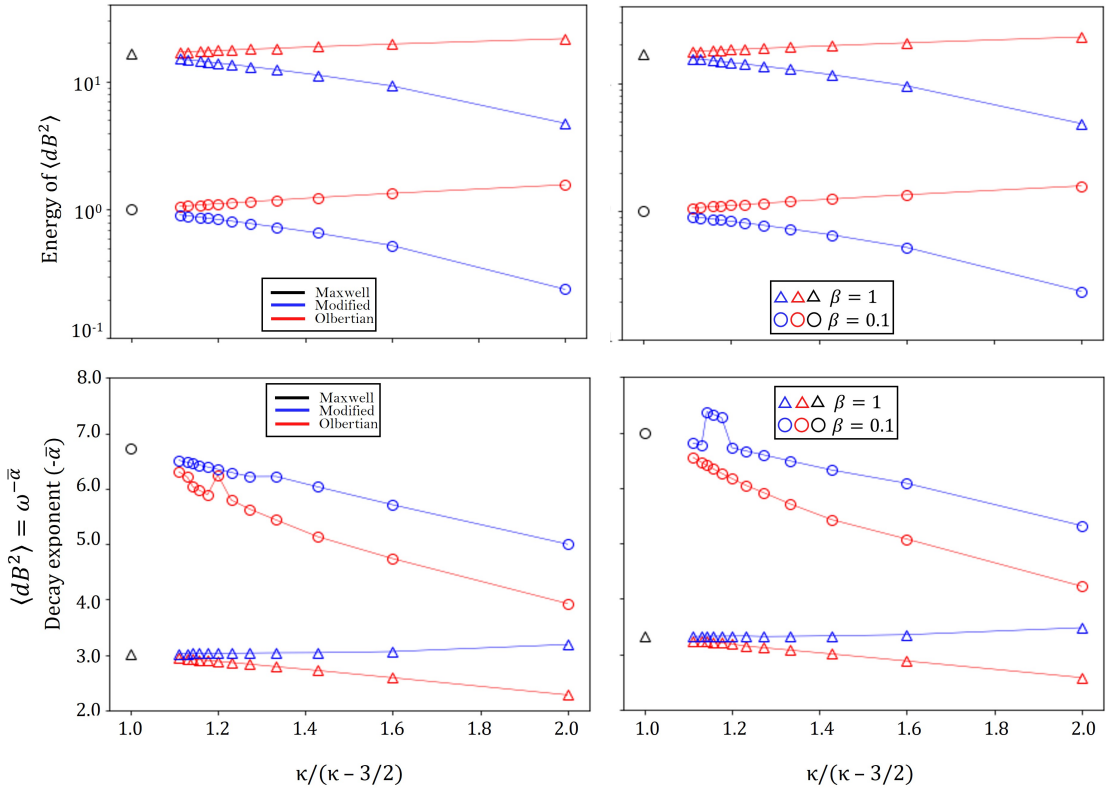

Figure 5.12: Top panel shows the total energy of spontaneous magnetic fluctuations for each velocity distribution case for two temperature anisotropy values, $A = 0.8$ and $A = 1.2$. The bottom panel shows the respective decay exponent of the reduced magnetic spectra with power-law decay behavior ($\langle \delta B^2 \rangle = \omega^{-\bar{\alpha}}$), using the same color code as in Figure 5.7. When considering the limit $\kappa \to \infty$, we recover the thermal equilibrium limit, $\kappa/(\kappa - 3/2) = 1$. All energy spectrum cases are normalized to the thermal equilibrium case with $\beta = 0.1$.

It is worth noting that for larger kappa values, the linear kinetic theory predicts $\kappa - 1$ transverse dispersion modes. Hence, for larger κ configurations, the integration over frequency and wave number of $[\langle dB^2 \rangle_{(\omega,k)}]_\kappa \propto [\Lambda^{-1}]_{\kappa-1}$ may pass over some dispersion modes due to the frequency and wave number resolution of the tensor

calculation. This produces numerical issues, resulting in noise in the energy and exponent decay results for larger κ values.

Chapter 6

Comparison between theory and simulation results

In this chapter, we briefly analyze 1.5D PIC results to assess the consistency of the theoretical results (for more details, see appendix B). In Figure 6.1, we show the isotropic temperature case of magnetic fluctuations. Theoretical results are shown on the left panel, and simulation results are on the right. Generally, the fluctuations have the same shape in theory and simulations. However, the simulations show an enhanced level of fluctuations in the same frequency and wave number range. Additionally, in the simulation results, mirror dispersion branches appear for positive frequencies in the positive range of frequencies (see Figure 6.1, $\beta = 0.1$ case for positive frequencies). These are symmetrical dispersion branches of the whistler-cyclotron mode.

However, to obtain comparable spectra shapes with the theory, we apply a Gaussian filter to smooth the simulation results. In general, simulations show the same core shape of magnetic fluctuations as the theoretical results. This means that fluctuations are enhanced and broadened as the β value increases and the κ value decreases. Simulations also preserve the characteristic features of the Modified and Olbertian cases, where the Modified spectra tend to distribute high intensity of fluctuations for frequencies near the whistler dispersion branch, and the Olbertian spectra show a homogeneous distribution of these fluctuations, as occurs with the Maxwell model. This leads to comparable results in the reduced magnetic spectra obtained from both theory and simulations.

In figure 6.2, we plot the reduced decay spectra for theoretical and simulation results. Generally, simulations and theory results share the same decay behavior. Nevertheless, simulations do from higher energy levels. In addition, Maxwell and Modified distribution results (dashed black and blue colors) tend to be closer to

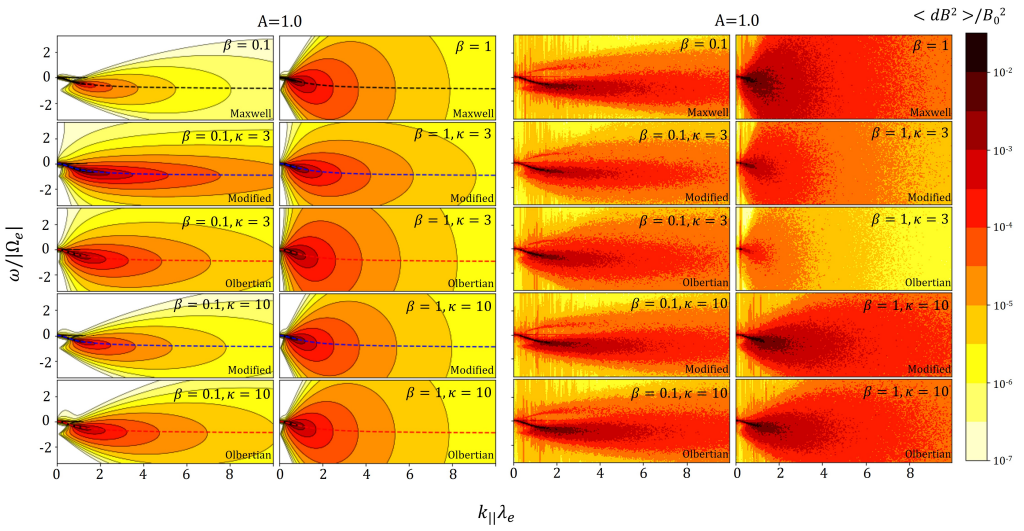

Figure 6.1: Normalized spontaneous magnetic fluctuations are shown with respect to the mean value of the background magnetic field. The theoretical results are displayed in the left panel, and the simulation results are shown on the right. The color bar is in logarithmic scale, representing the intensity of the magnetic fluctuations.

simulations results. This happens in theory results, but for the Olbertian and Maxwell distribution cases (solid red and black curves). However, we will show below that simulations and theory share almost the same decay index.

Figure 6.2 displays the reduced decay spectra for both theoretical and simulation results. The decay behavior is generally similar for both simulations and theory results. However, the simulations show higher energy levels. Additionally, the Maxwell and Modified distribution results (dashed black and blue colors) are closer to the simulation results. This is also observed in the theory results, but for the Olbertian and Maxwell distribution cases (solid red and black curves). However, we will demonstrate below that simulations and theory share nearly the same decay index (see Figure 6.3).

We also computed the total energy of magnetic fluctuations and the corresponding decay index for the simulation results in Figure 6.3. Here, we compare the total energy and index decay between theory and simulation results. As shown in Figure 6.3, for Olbertian cases (red colors), the theory results represented with solid markers match the energy results of simulation data represented with open markers, but with slightly less energy.

However, there are differences in the trend for the Modified cases (blue colors) between theory (void markers) and simulation (solid markers). In theory results, the

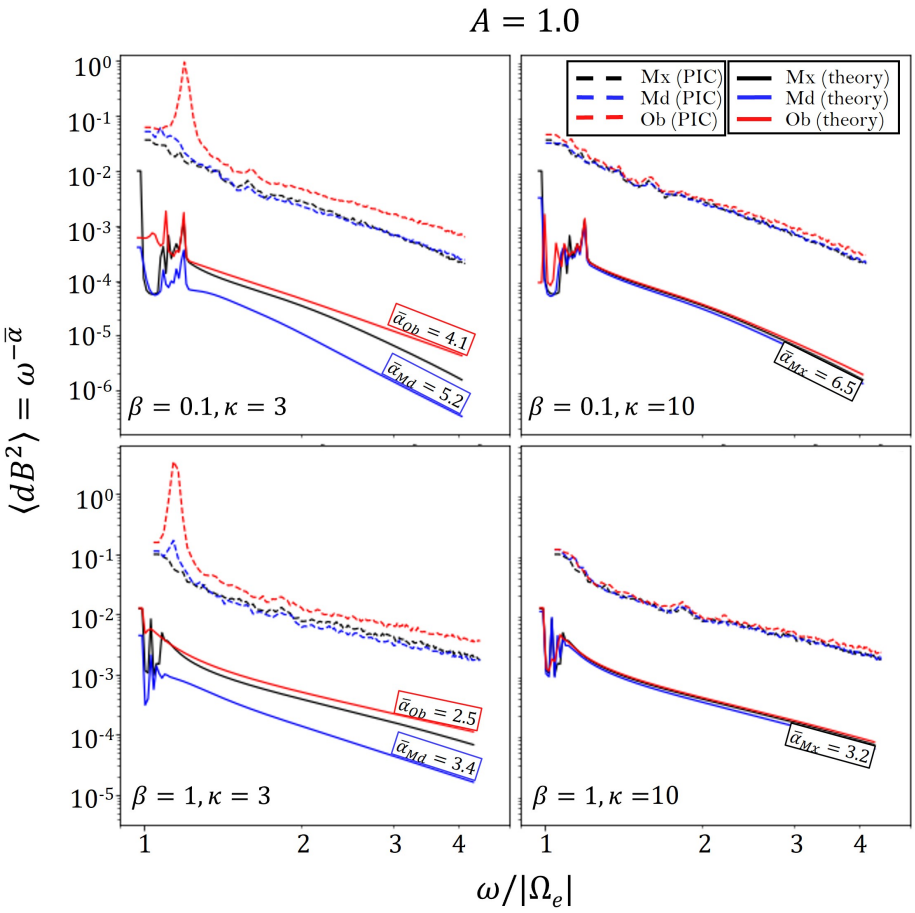

Figure 6.2: Reduced magnetic energy, in terms of frequency $\langle \delta B^2 \rangle_\omega = \omega^{-\overline{\alpha}}$, is shown for each velocity distribution case. This is the same result as in Figure 5.5 but with simulation results shown as dashed lines.

energy values decrease as the κ value decreases. In contrast, for simulation results, as κ decreases, the energy remains almost equal to the equilibrium case ($\beta = 1$) or even increases ($\beta = 0.1$). This behavior in theoretical results is due to the dependence of the dispersion tensor elements in the analytic expression of magnetic fluctuations, which takes into account electromagnetic resonance effects that simulations handle differently. In theory, we compute second-order correlations with a linear dispersion tensor at first order, while simulations consider higher non-linear orders in their results.

The exponent decay of both kappa distribution theory results matches well with the trend in β and κ values observed in the simulations. Furthermore, by increasing the κ value, both simulations and theory results are able to recover the thermal

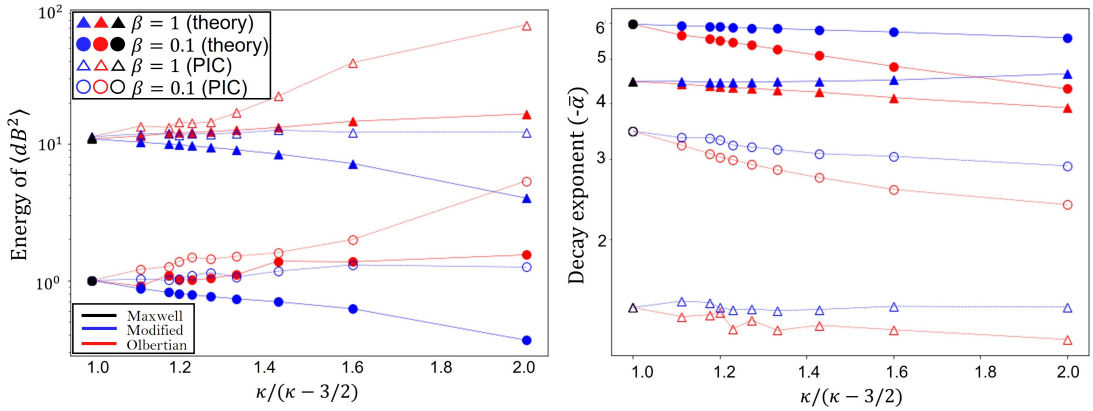

Figure 6.3: The left panel shows the total energy of magnetic fluctuations for each velocity distribution case analyzed in different β regimes, presented in terms of $\kappa/(\kappa - 3/2)$. In this function, the limit $\kappa \to \infty$ tends to $\kappa/(\kappa - 3/2) = 1$, recovering the thermal equilibrium case. The entire energy spectrum shown is normalized to the Maxwell case in the configuration $\beta = 0.1$. The right panel displays the index of the power-law decay, $\langle dB^2 \rangle = \omega^{-\bar{\alpha}}$, for each case. The $\bar{\alpha}_i$ index is the same as in Figure 5.5, but for additional κ cases. The black marker represents the Maxwell distribution result, while the red and blue markers represent the Olbertian and Modified distribution results, respectively. Void markers are for PIC data, and solid markers represent theory results. Each panel is in semi-log.

equilibrium energy and decay exponent. Additionally, both the kappa models in theory and simulations increase the energy by increasing the β parameter. These results provide strong support for the theoretical prediction of magnetic fluctuations.

6.1 Temperature anisotropy results

For completeness, we briefly analyze theoretical results of temperature anisotropic conditions compared to simulation results in Figure 6.4. We include the respective simulation results from Figure 5.9. It is evident that simulations have weaker fluctuation levels near zero frequency compared to theory, which predicts fluctuations around the zero frequency value due to the explicit dependence of the dispersion tensor. In addition, the shape of the spectra shown in Figure 6.4 is different as simulation results do not show any discontinuity of contour levels (see Figure 6.4). However, the other features between theory and simulations described in Figure 6.1 apply to this case.

In addition, we computed the reduced magnetic spectra decay with theoretical

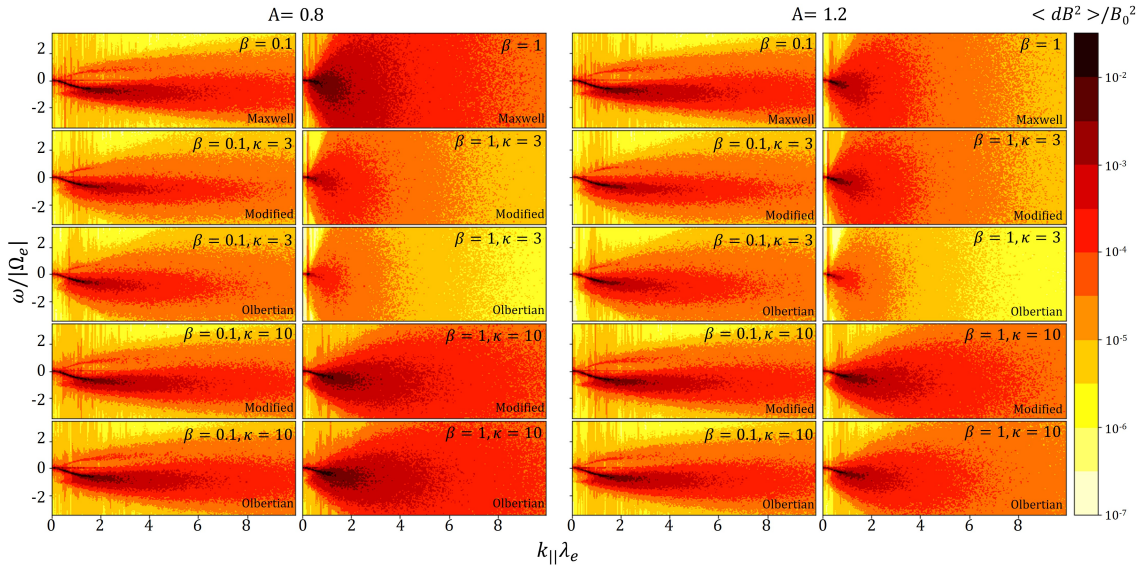

Figure 6.4: Simulation results of Figure 5.9.

results in Figure 6.5 for the anisotropic temperature cases. The features described above for the isotropic case in Figure 6.2 are also observed in these cases. Both theory and simulation results show fluctuations near the $\omega/|\Omega_e| = 1.3$ value, which is due to electron resonance with the electromagnetic wave mode. Hence, near the peak of the reduced magnetic energy, we expect enhanced fluctuations at the first multiple of the cyclotron frequency.

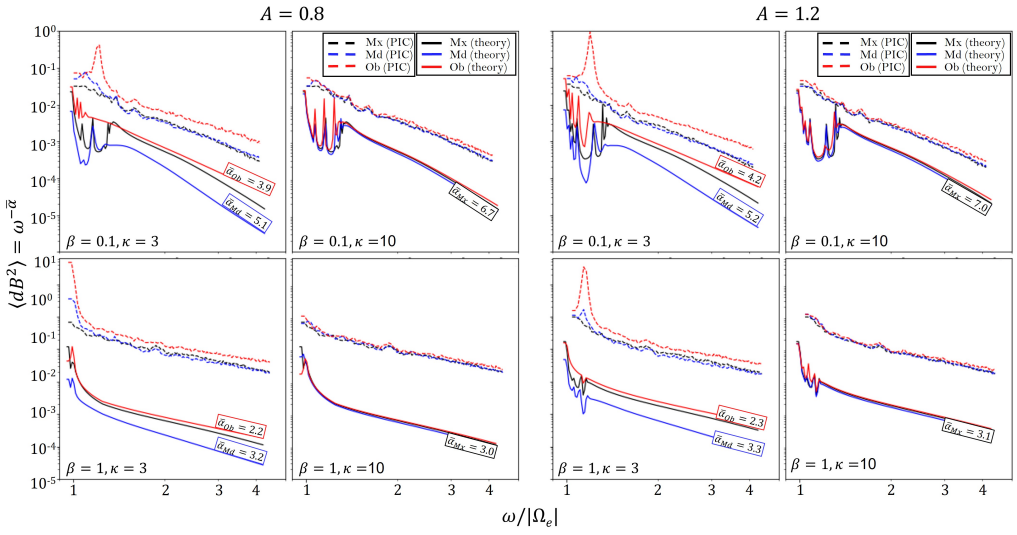

Figure 6.5: Reduced magnetic energy. Temperature anisotropy results of Figure 6.5.

Finally, we also perform anisotropic temperature cases for Figure 6.3. The results for energy and decay index obtained from theory and simulations, as shown in Figure 6.6, preserve the features described above in the isotropic case (see Figure 6.3). This result suggests that small changes in anisotropy lead to similar magnetic spectra results.

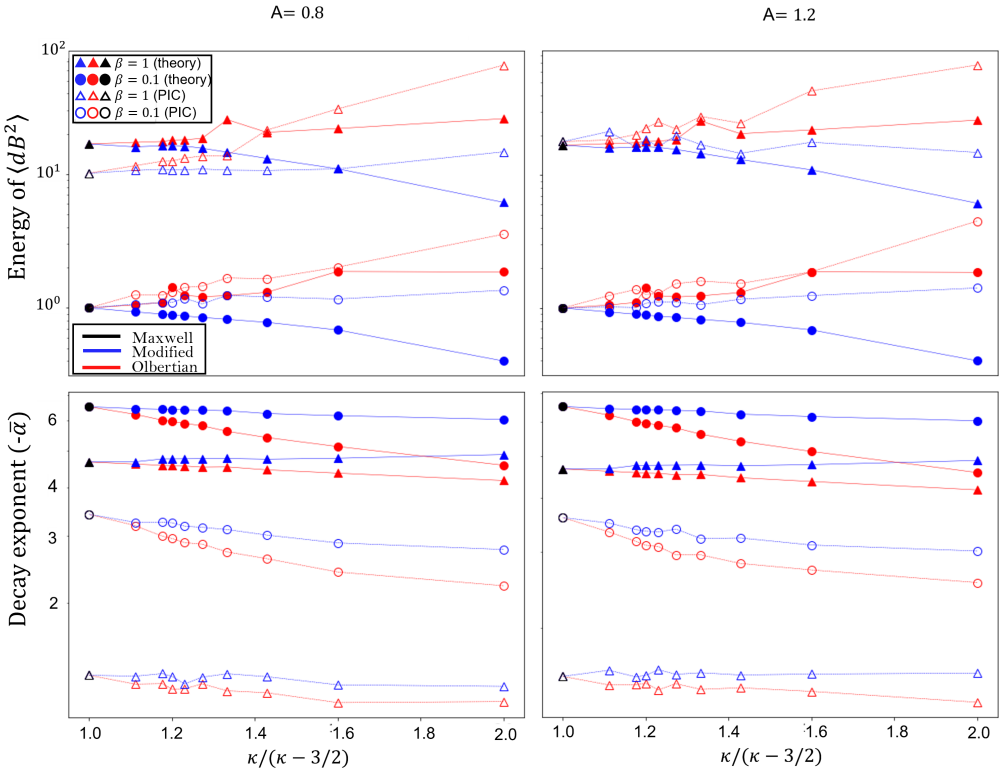

Figure 6.6: Total magnetic energy and power-law decay exponent for the temperature anisotropy cases shown in Figure 6.3. We use the same color code of Figure 6.5 for each velocity distribution result.

Chapter 7

Conclusion

In this study, we aim to distinguish between the two kappa models (Olbertian and Modified velocity distributions). We use the theory of electromagnetic fluctuations for magnetized plasmas that are out of equilibrium, as well as PIC simulations. Our main results come from analyzing the subtracting spectra (shown in Figure 5.6) and the energy of these fluctuations with respect to the κ value (shown in Figure 6.3). We found that both kappa models exhibit a high intensity of fluctuations distributed in a distinct manner for each kappa model, in comparison to the equilibrium case, and how is the energy obtained from the spectra of both models while the κ value decreases.

Specifically, this work replicates the linear kinetic and electromagnetic fluctuation theory for magnetized plasmas that are out of equilibrium [33, 70, 71, 74]. However, we enhance the analysis by examining the use of the Modified kappa distribution, with macroscopic parameters set within a range commonly observed in the solar wind. Our analysis revealed differences in the magnetic fluctuation spectra and their energy range. The linear kinetic results from the two main interpretations of the kappa distribution give us insights into the contribution of suprathermal electrons to the continuum spectra of magnetic fluctuations. Additionally, we analyzed the role of high-density, low-velocity electrons in the Modified kappa case.

Since a kappa distribution is an asymptotic result of electrostatic turbulence, which is frequently observed in the solar wind near the plasma frequency, we believe it deserves further exploration. However, it is worth noting that these distributions have numerical issues, such as divergence on higher-velocity moments. Furthermore, the Modified kappa distribution does not reproduce the thermal core for lower values of κ, which makes the scenarios where it is applicable more specific and complex. However, the ubiquitous empirical observations in space plasma environments makes these models valid.

The kappa-distributed electron plasma exhibits differences in the contribution of supra-thermal electron populations (and low-energy electrons in the Modified case) to the energy decay of the reduced magnetic spectra, as well as in the shape and power of the fluctuating magnetic field spectrum. The behavior of electromagnetic fluctuations obtained from each distribution case follows a similar trend when changes are made to the β parameter. It is expected that the power of magnetic field fluctuations will increase as the β values become larger. The main difference lies in the trend of the kappa values changes. Electrons with high kinetic energy, described by the Olbertian distribution, interact differently via cyclotron resonance with whistler cyclotron waves. This leads to a larger damping rate decay at smaller space scales and enhanced growth rates regarding the Modified kappa model.

Regarding the full spectrum of magnetic fluctuations, the Olbertian distribution describes electrons with high energy that spread magnetic fluctuations uniformly over a larger frequency domain. In contrast, the Modified kappa distribution considers the electrons that spread magnetic field fluctuations to be distributed closely around the typical frequency range of whistler-cyclotron waves, which is $|\Omega_p| < \omega < |\Omega_e|$. This feature suggests that the changes in the magnetic field are concentrated near the dispersion branch due to the large population of low-energy particles, without propagating magnetic fluctuations to larger frequencies. Furthermore, the magnetic spectra modeled with the Modified kappa distribution exhibits a similar shape to the Olbertian distribution, as both models take into account the contribution of suprathermal electrons to magnetic field fluctuations, unlike the Maxwell function. It is worth noting that the high intensity of magnetic field changes in the Modified case in comparison with the Maxwell case is even more concentrated close to the electromagnetic mode's dispersion branch.

The power law decay of the reduced magnetic fluctuating spectrum $\langle dB^2 \rangle = \omega^{-\bar{\alpha}_i}$ exhibits a steeper slope decay in the Modified case as compared to the Olbertian distribution. It can be attributed to the fact that the large intensity of fluctuations is concentrated near the first multiple of the cyclotron frequency in the Modified case, which is not a shared feature of the Olbertian model. As a result, this observation provides evidence of a more uniform distribution of the magnetic fluctuations in the Olbertian model. In addition, for the Olbertian case, as κ decreases, the decay slope flattens for any β and κ values, compared to the Modified and the Maxwell distributions. The large amount of electrons with high energy modeled with the Olbertian distribution causes magnetic fluctuations to be rigid over a larger frequency range. Interestingly, for $\beta = 1$, the Modified case exhibits an even larger value of the decay exponent as compared to the Maxwell and Olbertian distributions at the same macroscopic parameter configuration when the κ value is decreased. Besides, small changes in the temperature anisotropy do not significantly change the decay index in comparison with the isotropic case.

Furthermore, comparing the entire spectra of all distribution models in terms

of wave number and frequency reveals interesting features that can be used to distinguish between these models. One of the distinguishing features among these distribution models is the intensity of magnetic fluctuations for each case. The Olbertian distribution exhibits more intense fluctuations than both the Modified and Maxwell cases. In the Modified case, compared to the Maxwell distribution model, there are triangular bands at higher frequencies where spontaneous magnetic fluctuations are more intense. Below this frequency regime, magnetic fluctuations modeled with a Maxwellian distribution predominate. This feature suggests a way to distinguish between the Modified kappa model and the Maxwell distribution in terms of magnetic fluctuations. The spectra of the Modified case are always broader than those of the Maxwell case.

Furthermore, in Chapter six, we conducted a comparative analysis between the theoretical predictions and simulation results. It is noteworthy that, in general, the theoretical predictions are consistent with the simulation results, which reaffirms the relevance of electromagnetic fluctuation plasma analysis when the plasma is out of thermal equilibrium. However, in the Modified case, there are differences in the energy values of magnetic fluctuations for low κ values. Theoretical results show that the energy values of magnetic fluctuations in the Modified case decrease as the κ value decreases. On the other hand, in the Olbertian case, the energy of magnetic fluctuations increases as the κ value decreases. In the Modified case, the energy values in simulation data are almost equal to those obtained in the Maxwell distribution case when the κ value decreases. Furthermore, in the Olbertian case, both theory and simulations show a trend of increasing magnetic fluctuation energy as the κ value decreases. However, the energy values obtained in simulations are consistently larger than those predicted by theory.

There may be a possible explanation for the discrepancy between the theory and simulation results, which is that the theory explicitly considers the dependence of the dispersion tensor, whereas this is not accounted for in the simulations. Additionally, PIC simulations incorporate non-linear effects that are not present in the theory of fluctuations. Nevertheless, the agreement between the theory and simulation results highlights the idea that small variations in anisotropy lead to insignificant changes compared to the isotropic case.

There is a discrepancy between the Maxwell function and the Modified function cores for lower κ values. Thereby, it is challenging to attribute these differences solely to the faint suprathermal population of the Modified case. To explain the differences between the two kappa models in growth rates, stationary regime, damping rates, and the associated continuum spectra of magnetic fluctuations, the analysis of the Modified case must consider the effects of the low-energy core species combined with faint suprathermal tails. While the differences in the wave dispersion branch and growth rates are minor in the isotropic and anisotropic temperature cases, the complete magnetic spectra analysis provides a possibility to differentiate plasmas

modeled with both kappa distributions.

The projection of this work is to enhance the analysis using non-linear higher-order results. By utilizing the weak electrostatic turbulence theory described in reference [47], we intend to develop an electromagnetic theory for non-linear higher orders. These results will allow us to consider the spontaneous and induced processes that are involved in electromagnetic fluctuations. To provide an accurate description, it may be necessary to use Klimontovich's equation [54] instead of Vlasov's equation [24]. The advantage of this kinetic particle equation is that it incorporates spontaneous and induced processes and balances them in a manner similar to a Fokker-Planck equation for higher non-linear orders.

Considering this last kinetic particle equation will improve the description of wave-wave and wave-particle interactions and offer a more accurate characterization of the different contributions of plasma species with high energy, modeled with both kappa interpretations. Additionally, we plan to develop a wave kinetic equation in the framework of kappa models that properly describes higher non-linear order interactions of suprathermal charges emissions. This would guide the search for answers to questions about coronal heating and unexpected cooling rates with unsolved heat-flux mechanisms in the radial evolution of the solar wind. In this spirit, improving the numerical scheme to include the thermal relaxation process toward higher time scales will also be necessary.

In addition to the mentioned objectives, we aim to expand the scope of this work by applying it to spectrographic techniques. To achieve this, we plan to incorporate different kappa distribution models into the analysis, resulting in a more comprehensive investigation of enhanced electromagnetic fluctuations. This would improve upon the idealized electrostatic spectra results that are typically measured in the solar wind, as they tend to underestimate the contribution of suprathermal plasma populations [37]. By studying electromagnetic fluctuations, we will gain a better understanding of the properties of the Alvenic solar wind in the context of temperature anisotropy and beta diagrams. Ultimately, we hope to apply this theory to observational data obtained from spacecraft missions, making it a valuable tool for the space plasma community to differentiate between various non-thermal equilibrium scenarios.

Publications

The articles derived from this thesis are listed below.

1. Daniel H.P., Bea Zenteno-Quinteros, Pablo S. Moya, R. López, and M. Lazar, "Spectra of spontaneous emissions in high frequency magnetized κ-plasma" (in prep.)
2. Daniel H.P., Bea Zenteno-Quinteros, and Pablo S. Moya, "Spectra of anisotropic temperature spontaneous emissions through 1.5D PIC simulations" (in prep.)

Bibliography

[1] I. Langmuir. Oscillations in Ionized Gases. *Proceedings of the National Academy of Sciences*, 14:627–637, 1928.

[2] W. Crookes. On radiant matter. *Journal of the Franklin Institute*, 20:419–423, 1879.

[3] Š. Štverák, P. Trávníček, M. Maksimovic, E. Marsch, A. N. Fazakerley, and E. Scime. Electron temperature anisotropy constraints in the solar wind. *Journal of Geophysical Research*, 113:10, 2008.

[4] D. Bale, M. Pulupa, Ch. Salem, H. K. Chen, and E. Quataert. Electron heat conduction in the solar wind: transition from Spitzer- Härm to the collisionless limit. *The Astrophysical Journal*, 769:L22, 2013.

[5] M. Lazar, R. A. López, S. M. Shaaban, S. Poedts, P. H. Yoon, and H. Fichtner. Temperature anisotropy instabilities stimulated by the solar wind suprathermal populations. *Frontiers in Astronomy and Space Sciences*, 8:249, 2022.

[6] I. H. Cairns, B. Li, and J. M. Schmidt. Importance of Kappa Distributions to Solar Radio Bursts. In *Kappa Distributions: Theory and Applications in Plasmas*, volume 1, pages 549–567. 2017.

[7] S. M. Shaaban, M. Lazar, and R. Schlickeiser. Electromagnetic ion cyclotron instability stimulated by the suprathermal ions in space plasmas: A quasi-linear approach. *Physics of Plasmas*, 28:022103, 2021.

[8] M. Lazar, R. A. López, S. M. Shaaban, S. Poedts, and H. Fichtner. Whistler instability stimulated by the suprathermal electrons present in space plasmas. *Astrophysics and Space Science*, 364:171, 2019.

[9] P. S. Moya, M. Lazar, and S. Poedts. Toward a general quasi-linear approach for the instabilities of bi-kappa plasmas. whistler instability. *Plasma Physics and Controlled Fusion*, 63:25011, 2020.

[10] G. Livadiotis. Introduction to special section on origins and properties of kappa distributions: Statistical background and properties of kappa distributions in

space plasmas. *Journal of Geophysical Research A: Space Physics*, 120:1607–1619, 2015.

[11] M. Lazar. Kappa distributions from observational evidences via controversial predictions to a consistent theory of nonequilibrium plasmas. *Springer International Publishing*, 1:293–298, 2021.

[12] G. Livadiotis. Kappa distributions: Theory and applications in plasmas. *Elsevier*, 2017.

[13] R. A. López, M. Lazar, S. M. Shaaban, S. Poedts, and P. S. Moya. Alternative high plasma beta regimes of electron heat flux instabilities in the solar wind. *The Astrophysical Journal*, 900:L25, 2020.

[14] B. Zenteno-Quinteros and P. S. Moya. The role of core and strahl electrons properties on the whistler heat-flux instability thresholds in the solar wind. *Frontiers in Physics*, 1:411, 2022.

[15] P. Yoon. Thermodynamic, non-extensive, or turbulent quasi-equilibrium for the space plasma environment. *Entropy*, 21:820, 2019.

[16] G. Livadiotis. Thermodynamic origin of kappa distributions. *EPL*, 122:50004, 2018.

[17] P. H. Yoon and R. A. López. Spontaneous emission of electromagnetic fluctuations in magnetized plasmas. *Physics of Plasmas*, 24:022117, 2017.

[18] G. Livadiotis and D. J. McComas. Black-body radiation in space plasmas. *EPL*, 135:49001, 2021.

[19] P. H. Yoon. Non-equilibrium statistical mechanical approach to the formation of non-maxwellian electron distribution in space. *European Physical Journal-special Topics*, 229:819–840, 2020.

[20] B. Zenteno-Quinteros, A. F. Viñas, and P. S. Moya. Skew-kappa distribution functions and whistler-heat flux instability in the solar wind. *EGU General Assembly*, pages EGU21–3464, 2021.

[21] M. Lazar, V. Pierrard, S. M. Shaaban, H. Fichtner, and S. Poedts. Dual maxwellian kappa modeling of the solar wind electrons: new clues on the temperature of kappa populations. *Astronomy and Astrophysics*, 602:A44, 2017.

[22] P. H. Yoon. Electron kappa distribution and quasi-thermal noise. *Journal of Geophysical Research*, 119:7074–7087, 2014.

[23] C. Vocks. Kinetic models of wave-electron interaction in the solar corona and wind. *Astrophysics and space science library*, 2:125–143, 2021.

[24] A. Vlasov. The vibrational properties of an electron gas. *Physics-Uspekhi*, 10:721, 1968.

[25] D.G. Swanson. Plasma waves. *Elsevier Science*, 2012.

[26] M. Lazar, S. Poedts, and H. Fichtner. Destabilizing effects of the suprathermal populations in the solar wind. *Astronomy and Astrophysics*, 582:1–7, 2015.

[27] V. Pierrard and M. Lazar. Kappa Distributions: Theory and Applications in Space Plasmas. 267(1):153–174, 2010.

[28] G. Livadiotis and D. J. McComas. Understanding kappa distributions: A toolbox for space science and astrophysics. *Space Science Reviews*, 41:1600–1606, 2013.

[29] C. Tsallis. Possible generalization of Boltzmann-Gibbs statistics. *Journal of Statistical Physics*, 48:1–13, 1988.

[30] M. N. S. Qureshi, G. Pallocchia, R. Bruno, M. B. Cattaneo, V. Formisano, H. Reme, J. M. Bosqued, I. Dandouras, J. A. Sauvaud, L. M. Kistler, E. Möbius, B. Klecker, C. W. Carlson, J. P. McFadden, G. K. Parks, M. McCarthy, A. Korth; R. Lundin, A. Balogh, and H. A. Shah. Solar wind particle distribution function fitted via the generalized kappa distribution function: Cluster observations. *AIP proceedings*, 2003.

[31] S. Olbert. Summary of experimental results from M.I.T. detector on IMP-1. *Physics of the Magnetosphere, eds. R. D. L. Carovillano, & J. F. McClay, Astrophys. Space Sci. Libr.*, 24:022117, 1968.

[32] V. Vasyliunas. A survey of low-energy electrons in the evening sector of the magnetosphere with OGO 1 and OGO 3. *Journal of Geophysical Research*, 73:7519–7523, 1968.

[33] M. Lazar, H. Fichtner, and P. H. Yoon. On the interpretation and applicability of κ-distributions. *Astronomy and Astrophysics*, 589:A39, 2016.

[34] N. Meyer-Vernet. Basics of the solar wind: The outer solar atmosphere. *Cambridge University Press*, 2007.

[35] N. Meyer-Vernet. Basics of the solar wind: Anatomy of the sun. *Cambridge University Press*, 2007.

[36] N. Meyer-Vernet. Basics of the solar wind: How does the solar wind blow? *Cambridge University Press*, 2007.

[37] Nicole Meyer-Vernet. Basics of the solar wind. *Cambridge University Press*, 2007.

[38] B. Acosta, D. Pastén, and P. S. Moya. Reversibility of turbulent and non-collisional plasmas: Solar wind. *Proceedings of the International Astronomical Union*, 15:363–366, 2019.

[39] B. Acosta, D. Pastén, and P. S. Moya. Applying the horizontal visibility graph method to study irreversibility of electromagnetic turbulence in non-thermal plasmas. *Entropy*, 23:470, 2021.

[40] N. Meyer-Vernet. Basics of the solar wind: Structure and perturbations. *Cambridge University Press*, 2007.

[41] J. A. Valdivia, B. A. Toledo, N. Gallo, V. Muñoz, J. Rogan, M. Stepanova, P. S. Moya, R. E. Navarro, A. F. Viñas, J. A. Araneda, R. A. López, and M. Diaz. Magnetic fluctuations in anisotropic space plasmas: The effect of the plasma environment. *Advances in Space Research*, 58:2126–2133, 2016.

[42] A. F. Viñas, P. S. Moya, R. E. Navarro, J. A. Valdivia, J. A. Araneda, and V. Muñoz. Electromagnetic fluctuations of the whistler-cyclotron and firehose instabilities in a Maxwellian and Tsallis-kappa-like plasma. *Journal of Geophysical Research: Space Physics*, 120:3307–3317, 2015.

[43] M. L. Adrian, A. F. Viñas, P. S. Moya, and D. E. Wendel. Solar wind magnetic fluctuations and electron non-thermal temperature anisotropy: Survey of Wind-SWE-VEIS observations. *The Astrophysical Journal*, 833:49, 2016.

[44] P. H. Yoon. Kinetic instabilities in the solar wind driven by temperature anisotropies. *Reviews of Modern Plasma Physics*, 1:1–69, 2017.

[45] P. Hellinger, P. Trávníček, J. C. Kasper, and A. J.Lazarus. Solar wind proton temperature anisotropy: Linear theory and WIND/SWE observations. *Geophysical Research Letters*, 33:10, 2006.

[46] M. Maksimovic, V. Pierrard, and P. Riley. Ulysses electron distributions fitted with kappa functions. *Geophysical Research Letters*, 24:1151–1154, 1997.

[47] P. H. Yoon. Classical kinetic theory of weakly turbulent nonlinear plasma processes. *Cambridge University Press*, 2019.

[48] N. Meyer-Vernet, P. Couturier, S. Hoang, J. L. Steinberg, and R. D. Zwickl. Ion thermal noise in the solar wind: Interpretation of the "excess" electric noise on ISEE 3. *Journal of Geophysical Research*, 91:3294–3298., 1986.

[49] N. Meyer-Vernet, S. Hoang, K. Issautier, M. Moncuquet, and G. Marcos. Plasma thermal noise: The long wavelength radio limit. In *Geophysical Monograph Series*, volume 119, page 67. 2000.

[50] M. Lazar, S. Kim, R. A. López, P. H. Yoon, R. Schlickeiser, and S. Poedts. Suprathermal Spontaneous Emissions in κ -distributed Plasmas . *The Astrophysical Journal*, 868:L25, 2018.

[51] N. Meyer-Vernet and C. Perche. Tool kit for antennae and thermal noise near the plasma frequency. *Journal of Geophysical Research*, 94:2405–2415, 1989.

[52] H. B. Callen and T. A. Welton. Irreversibility and generalized noise. *Physical Review*, 83:34, 1951.

[53] A. G. Sitenko. Electromagnetic fluctuations in plasma. *Academic Press, New York*, 1967.

[54] J. P. Dougherty and L. Klimontovich. The statistical theory of non-equilibrium processes in a plasma. *Pergamon Press*, 1967.

[55] V. Pierrard, M. Maksimovic, and J. Lemaire. Core, halo and strahl electrons in the solar wind. *Astrophysics and Space Science*, 277:195–200, 2001.

[56] M. Maksimovic, I. Zouganelis, J. Chaufray, K. Issautier, E. Scime, J. Littleton, E. Marsch, D. Mccomas, C. Salem, R. Lin, and H. Elliott. Radial evolution of the electron distribution functions in the fast solar wind between 0.3 and 1.5 AU. *Journal of Geophysical Research*, 110:9, 2005.

[57] S. Stverak, P. Travnicek, M. Maksimovic, E. Marsch, A. N. Fazakerley, and E. Scime. Radial evolution of non-thermal electron populations in the low-latitude solar wind: Helios, cluster and ulysses observations. *Journal of Geophysical Research: Space Physics*, 114:11, 2009.

[58] M. Maksimovic, V. Pierrard, and J. Lemaire. A kinetic model of the solar wind with kappa distribution functions in the corona. *Astronomy and Astrophysics*, 324:725–734, 1997.

[59] I. Zouganelis. Measuring suprathermal electron parameters in space plasmas : Implementation of the quasi-thermal noise spectroscopy with kappa distributions using in situ ulysses/urap radio measurements in the solar wind. *Journal of Geophysical Research*, 113:12, 2008.

[60] G. Lapenta, J. Berchem, M. El-Alaoui, and R. J. Walker. Turbulent energization of electron power law tails during magnetic reconnection. *Plasma Physics*, 125:225101, 2020.

[61] H. Arnold, J. F. Drake, M. Swisdak, F. Guo, J. Dahlin, B. Chen, G. D. Fleishman, L. Glesener, E. P. Kontar, T. Phan, and C. Shen. Electron acceleration during macroscale magnetic reconnection. *Physical Review Letters*, 126:135101, 2021.

[62] G. Livadiotis, M. I. Desai, and L. B. Wilson. Generation of kappa distributions in solar wind at 1 au. *The Astrophysical Journal*, 853:142, 2018.

[63] G. Livadiotis. Using kappa distributions to identify the potential energy. *Journal of Geophysical Research*, 123:1050–1060, 2018.

[64] G. Livadiotis, D. Mccomas, H. Funsten, N. Schwadron, J. Szalay, and E. Zirnstein. Thermodynamics of the inner heliosheath. *The Astrophysical Journal Supplement Series*, 262:53, 2022.

[65] G.Livadiotis. Introduction to special section on origins and properties of kappa distributions: Statistical background and properties of kappa distributions in space plasmas. *Journal of Geophysical Research*, 120:1607–1619, 2015.

[66] B. D. Fried and S. D. Conte. The plasma dispersion function. *Academic Press*, 123:1050–1060, 1961.

[67] M. A. Hellberg and R. L. Mace. Generalized plasma dispersion function for a plasma with a kappa-maxwellian velocity distribution. *Physics of Plasmas*, 9:1495–1504, 2002.

[68] R. L. Mace and M. A. Hellberg. A new formulation and simplified derivation of the dispersion function for a plasma with a kappa velocity distribution. *Physics of Plasmas*, 16:072113, 2009.

[69] R. L. Mace and R. D. Sydora. Parallel whistler instability in a plasma with an anisotropic bi-kappa distribution. *Journal of Geophysical Research*, 115:12, 2010.

[70] R. E. Navarro, J. Araneda, V. Muñoz, P. S. Moya, A. F.-Viñas, and J. A. Valdivia. Theory of electromagnetic fluctuations for magnetized multi-species plasmas. *Physics of Plasmas*, 112:18, 2014.

[71] R. E. Navarro, V. Muñoz, J. Araneda, A. F. Viñas, P. S. Moya, and J. A. Valdivia. Magnetic Alfvén-cyclotron fluctuations of anisotropic nonthermal plasmas. *Journal of Geophysical Research: Space Physics*, 120:2382–2396, 2015.

[72] A. F. Viñas, P. S. Moya, R. Navarro, and J. A. Araneda. The role of higher-order modes on the electromagnetic whistler-cyclotron wave fluctuations of thermal and non-thermal plasmas. *Physics of Plasmas*, 012902:21, 2014.

[73] V. Pierrard, M. Lazar, S. Poedts, Štverák, M. Maksimovic, and P. M. Trávníček. The Electron Temperature and Anisotropy in the Solar Wind. Comparison of the Core and Halo Populations. *Solar Physics*, 291:2165–2179, 2016.

[74] M. Lazar, S. Poedts, and H. Fichtner. Destabilizing effects of the suprathermal populations in the solar wind. *Astronomy and Astrophysics*, 582:A124, 2015.

[75] R. Navarro. Fluctuaciones electromagnéticas en plasmas tipo viento solar [thesis]. *Universidad de Chile*, 2014.

Appendix A

A.1 Linear kinetic analysis

Consider a magnetized plasma system at a high-frequency scale, where we can neglect the thermal motion of ions. Additionally, Coulomb collisions are ineffective in this high-frequency regime, therefore, we can consider Vlasov's particle kinetic equation. The closed equation starts with Maxwell's equations.

$$\nabla \cdot \mathbf{E} = 4\pi\rho, \tag{A.1}$$

$$\nabla \cdot \mathbf{B} = 0, \tag{A.2}$$

$$\nabla \times \mathbf{E} = \frac{1}{c}\frac{\partial \mathbf{B}}{\partial t}, \tag{A.3}$$

$$\nabla \times \mathbf{B} = \frac{1}{c}\frac{\partial \mathbf{E}}{\partial t} + \frac{4\pi}{c}\mathbf{J}. \tag{A.4}$$

Here, $\mathbf{E}$ represents the electric field, $\mathbf{B}$ represents the magnetic field, and $\mathbf{J}$ represents the current density. The velocity of light is denoted by c. Besides, to evolve the particle distribution f_α, we utilize Vlasov's equation.

$$\frac{\partial f_\alpha}{\partial t} + \mathbf{v} \cdot \nabla_r f_\alpha + \frac{q_\alpha}{m_\alpha}\left(\mathbf{E} + \frac{\mathbf{v}}{c} \times \mathbf{B}\right) \cdot \nabla_v f_\alpha = 0. \tag{A.5}$$

Here, q_α and m_α are charge and mass. Moreover, to close the system we define charge and current density that satisfy the continuity equation, where ρ stands for charge density, and n is the particle density,

$$\rho = q_\alpha n \int dv^3 f_\alpha, \tag{A.6}$$

$$\mathbf{J} = q_\alpha n \int dv^3 \mathbf{v} f_\alpha. \tag{A.7}$$

In addition, we establish stability conditions for linear analysis of the perturbation. The stationary state of quasi-equilibrium Vlasov's equation for initially current-free

and neutral plasma implies,

$$\frac{q_\alpha}{m_\alpha}\left(\frac{\mathbf{v}}{c}\times\mathbf{B}\right)\cdot\nabla_v f_{\alpha 0}=0. \tag{A.8}$$

At a certain time ($t=0$), we consider a perturbation in the electromagnetic field and a perturbation in the velocity distribution,

$$\begin{aligned}\mathbf{E} &= \delta\mathbf{E}, && \text{(A.9)}\\ \mathbf{B} &= \mathbf{B}_0+\delta\mathbf{B}, && \text{(A.10)}\\ f_\alpha &= f_{\alpha 0}+\delta f_\alpha. && \text{(A.11)}\\ & && \text{(A.12)}\end{aligned}$$

Linear perturbed quantities are specified with a δ. $\mathbf{B}_0$ is the background magnetic field. Subscript 0 indicates equilibrium quantities. The velocity is given in cylindrical coordinates, where the parallel and perpendicular directions are defined with respect to the background magnetic field, as follows,

$$\mathbf{v}=v_\perp\hat{\rho}+v_{||}\hat{z}. \tag{A.13}$$

We assume a gyrotropic solution for the disturbance of the velocity distribution, where ∇_v is in the cylindrical coordinate system. This leads to

$$\nabla_v\delta f_{0\alpha}\cdot\hat{\phi}=\frac{1}{v_\perp}\frac{\partial\delta f_{0\alpha}}{\partial\phi}. \tag{A.14}$$

Here ϕ is the azimuthal angle. Then,

$$\frac{q_\alpha}{m_\alpha}\frac{B_0}{c}\frac{\partial\delta f_{0\alpha}}{\partial\phi}=\Omega_\alpha\frac{\partial\delta f_{0\alpha}}{\partial\phi}, \tag{A.15}$$

where Ω_α is the gyro-frequency. To solve these types of differential equations, we apply Laplace-Fourier transform. For a quantity A, the respective transformation into frequency and wave number domain leads to,

$$A_{\mathbf{k}\omega}=\frac{1}{(2\pi)^{3/2}}\int_0^\infty dt\int d^3r A_{\mathbf{r}t}e^{-i(\mathbf{k}\cdot\mathbf{r}-\omega t)}. \tag{A.16}$$

On the other hand, the inverse of the transform Laplace-Fourier

$$A_{\mathbf{r}t}=\frac{1}{(2\pi)^{5/2}}\int d^3k\int_{i\bar{\omega}-\infty}^{i\bar{\omega}+\infty}d\omega A_{\mathbf{k}\omega}e^{i(\mathbf{k}\cdot\mathbf{r}-\omega t)},\ \bar{\omega}>\omega_0. \tag{A.17}$$

For ω_0 the singularity with a larger complex value and $\bar{\omega}$ is larger than ω_0 (see reference [75] for more details). Moreover, we use $\hat{A}:=A(\mathbf{k},\omega)$ for transformed

quantities. Then, by transforming the Vlasov-Maxwell equations and retaining only first-order terms, we obtain,

$$i(\mathbf{v}\cdot\mathbf{k}-\omega)\delta\hat{f}_\alpha+\Omega_\alpha\frac{\partial\delta\hat{f}}{\partial\phi}+\frac{q_\alpha}{m_\alpha}\left(\delta\hat{\mathbf{E}}+\frac{\mathbf{v}}{c}\times\delta\hat{\mathbf{B}}\right)\cdot\nabla_v f_{\alpha 0}=0. \tag{A.18}$$

On the other hand, from Ampere's law and Faraday's law, we obtain

$$\lambda\delta\hat{\mathbf{E}}=\frac{4\pi}{c}\delta\hat{\mathbf{J}}, \tag{A.19}$$

where λ is the dispersion tensor in the vacuum. Here the current density in Fourier space is,

$$\delta\hat{\mathbf{J}}=q_\alpha\int dv\mathbf{v}\delta\hat{f}_\alpha, \tag{A.20}$$

with

$$\delta\hat{f}_\alpha=\mathbf{F}\delta\hat{\mathbf{E}}. \tag{A.21}$$

Where $\mathbf{F}$ is a vector containing information about the dispersion properties, and it will be calculated below. Then, the induced current density is

$$\delta\hat{\mathbf{J}}=q_\alpha\int dv^3\mathbf{v}\delta\hat{f}=q_\alpha\left(\int dv^3\mathbf{v}\mathbf{F}\right)\delta\hat{\mathbf{E}}. \tag{A.22}$$

Considering the Eq. A.18, we compute

$$\frac{\partial\delta\hat{f}_\alpha}{\partial\phi}+\frac{i(\mathbf{v}\cdot\mathbf{k}-\omega)}{\Omega_\alpha}\delta\hat{f}_\alpha-\frac{q_\alpha}{m_\alpha\Omega_\alpha}\left(\delta\hat{\mathbf{E}}+\frac{\mathbf{v}}{c}\times\delta\hat{\mathbf{B}}\right)\cdot\nabla_v f_{\alpha 0}=0. \tag{A.23}$$

This first-order partial differential equation may be solved by the integrating factor, such that the solution is

$$\delta\hat{f}_\alpha=e^{-\int P(\phi)d\phi}\int e^{\int P(\phi)d\phi}Q(\phi)d\phi, \tag{A.24}$$

with $P(\phi)$ and $Q(\phi)$ functions that belong to class C_1 of differentiable functions, which are

$$P(\phi) = \frac{i}{\Omega_\alpha}(\omega-\mathbf{v}\cdot\mathbf{k}), \tag{A.25}$$

$$Q(\phi) = \frac{q_\alpha}{m_\alpha\Omega_\alpha}\left(\delta\hat{\mathbf{E}}+\frac{\mathbf{v}}{c}\times\delta\hat{\mathbf{B}}\right). \tag{A.26}$$

Considering only parallel propagation ($\mathbf{k}\times\delta\hat{\mathbf{B}}=0$), from Maxwell's equations, we obtain $\delta\hat{\mathbf{B}}=(c/\omega)\mathbf{k}\times\delta\hat{\mathbf{E}}$. Replacing these results into $Q(\phi)$,

$$P(\phi) = \frac{i}{\Omega_\alpha}(\omega-k_{||}v_{||}) \tag{A.27}$$

$$\int P(\phi)d\phi = \frac{i}{\Omega_\alpha}(\omega-k_{||}v_{||})\phi, \tag{A.28}$$

$$Q(\phi) = \frac{q_\alpha}{m_\alpha\Omega_\alpha}\left(\delta\hat{\mathbf{E}}+\frac{\mathbf{v}}{\omega}\times\mathbf{k}\times\delta\hat{\mathbf{E}}\right). \tag{A.29}$$

Expanding $Q(\phi)$ using the double cross product vector identity,

$$\begin{aligned} Q(\phi) &= \frac{q_\alpha}{m_\alpha \Omega_\alpha}\left(\delta\hat{\mathbf{E}} + \frac{\mathbf{v}}{\omega}\times\mathbf{k}\times\delta\hat{\mathbf{E}}\right), \\ Q(\phi) &= \frac{q_\alpha}{m_\alpha \Omega_\alpha}\left(\delta\hat{\mathbf{E}} + \frac{1}{\omega}(\mathbf{v}\cdot\delta\hat{\mathbf{E}}\mathbf{k} - (\mathbf{v}\cdot\mathbf{k})\delta\hat{\mathbf{E}})\right)\cdot\nabla_{\mathbf{v}} f_{0\alpha}. \end{aligned} \tag{A.30}$$

By considering the Cartesian coordinate system in the directions $\{i, j, k\}$, we obtain,

$$\mathbf{v}\cdot\delta\hat{\mathbf{E}} = (v_\perp\cos\phi\hat{i} + v_\perp\sin\phi\hat{j} + v_{||}\hat{k})\cdot\delta\hat{\mathbf{E}}. \tag{A.31}$$

In addition,

$$\nabla_{\mathbf{v}} f_{0\alpha} = \frac{\partial f_{\alpha 0}}{\partial v_\perp}\cos\phi\hat{i} + \frac{\partial f_{\alpha 0}}{\partial v_\perp}\sin\phi\hat{j} + \frac{\partial f_\alpha}{\partial v_{||}}\hat{k}. \tag{A.32}$$

Hence, replacing equations A.31 and A.32 into A.30,

$$Q(\phi) = \frac{q_\alpha}{m_\alpha\Omega_\alpha\omega}\left[\left(\bar{\Delta}\cos\phi\hat{i} + \bar{\Delta}\sin\phi\hat{j} + \omega\frac{\partial f_{0\alpha}}{\partial v_{||}}\hat{k}\right)\cdot\delta\hat{\mathbf{E}}\right], \tag{A.33}$$

$$Q(\phi) = \frac{q_\alpha}{m_\alpha\Omega_\alpha\omega}\bar{\mathbf{F}}\cdot\delta\hat{\mathbf{E}}. \tag{A.34}$$

Here, $\bar{\Delta}$ and $\bar{\mathbf{F}}$ stand for

$$\bar{\Delta} = (\omega - v_{||}k_{||})\frac{\partial f_{\alpha 0}}{\partial v_\perp} + k_{||}v_{||}\frac{\partial f_{\alpha 0}}{\partial v_{||}}, \tag{A.35}$$

$$\bar{\mathbf{F}} = \bar{\Delta}\cos\phi\hat{i} + \bar{\Delta}\sin\phi\hat{j} + \omega\frac{\partial f_{0\alpha}}{\partial v_{||}}\hat{k}. \tag{A.36}$$

Therefore, replacing equations A.35 and A.36 in A.24,

$$\delta\hat{f}_\alpha = e^{-(i/\Omega_\alpha)(\omega - v_{||}k_{||})\phi}\int e^{-(i/\Omega_\alpha)(\omega - v_{||}k_{||})\phi}\frac{q_\alpha}{m_\alpha\Omega_\alpha\omega}\bar{\mathbf{F}}\cdot\delta\hat{\mathbf{E}}. \tag{A.37}$$

Then to simplify A.37, we define

$$\sigma = \frac{\omega - k_{||}v_{||}}{\Omega_\alpha}. \tag{A.38}$$

Besides, to solve equation A.37 we use,

$$\int e^{i\sigma\phi}\cos\phi d\phi = -\frac{e^{\sigma\phi}(\sigma\cos\phi - i\sin\phi)}{\sigma^2 - 1}, \tag{A.39}$$

$$\int e^{i\sigma\phi}\sin\phi d\phi = \frac{e^{\sigma\phi}(\cos\phi - i\sigma\sin\phi)}{\sigma^2 - 1}, \tag{A.40}$$

$$\int e^{i\sigma\phi}d\phi = -i\frac{e^{i\sigma\phi}}{\sigma}. \tag{A.41}$$

Using this last set of integrals in equation A.38 we find $\mathbf{F}$ in equation A.21,

$$F_i = -\frac{\Delta q_\alpha}{m_\alpha \omega} i \left((\omega - k_{||} v_{||}) \cos\phi - \Omega_\alpha i \sin\phi \right), \tag{A.42}$$

$$F_j = -\frac{\Delta q_\alpha}{m_\alpha \omega} i \left(\Omega_\alpha i \cos\phi - (\omega - k_{||} v_{||}) \sin\phi \right), \tag{A.43}$$

$$F_k = -\frac{q_\alpha}{m_\alpha} i \frac{1}{\omega - v_{||} k_{||}} \frac{\partial f_{\alpha 0}}{\partial v_{||}}. \tag{A.44}$$

Here, Δ means,

$$\Delta = \left((\omega - v_{||} k_{||}) \frac{\partial f_{\alpha 0}}{\partial v_\perp} + k_{||} v_{||} \frac{\partial f_{\alpha 0}}{\partial v_{||}} \right) \left(\frac{1}{(\omega - k_{||} v_{||})^2 - \Omega_\alpha^2} \right). \tag{A.45}$$

Hence, the current density at linear order may be expressed as

$$\delta \hat{\mathbf{J}} = q_\alpha \int dv \mathbf{v} \delta \hat{f} = q_\alpha \left(\int dv \mathbf{v} \mathbf{F} \right) \delta \hat{\mathbf{E}} = q_\alpha M_\alpha \delta \hat{\mathbf{E}}. \tag{A.46}$$

In this last expression, M_α is a tensor with elements given by

$$M_{11} = -i \frac{q_\alpha}{m_\alpha \omega} \iint \frac{v_\perp^2 \bar{\Delta} dv_\perp dv_{||}}{\sigma^2 - 1} \int \sigma \cos^2\phi - i sin\phi \cos\phi d\phi, \tag{A.47}$$

$$M_{12} = -i \frac{q_\alpha}{m_\alpha \omega} \iint \frac{v_\perp^2 \bar{\Delta} dv_\perp dv_{||}}{\sigma^2 - 1} \int i \cos^2\phi + \sigma \sin\phi \cos\phi d\phi, \tag{A.48}$$

$$M_{13} = -i \frac{q_\alpha}{m_\alpha \omega} \iint \frac{v_\perp^2 \omega \frac{\partial f_{\alpha 0}}{\partial v_{||}}}{\alpha} dv_\perp dv_{||} \int \cos\phi d\phi, \tag{A.49}$$

$$M_{21} = -i \frac{q_\alpha}{m_\alpha \omega} \iint \frac{v_\perp^2 \bar{\Delta} dv_\perp dv_{||}}{\sigma^2 - 1} \int i\sigma \cos\phi \sin\phi - i sin^2\phi \cos\phi d\phi, \tag{A.50}$$

$$M_{22} = -i \frac{q_\alpha}{m_\alpha \omega} \iint \frac{v_\perp^2 \bar{\Delta} dv_\perp dv_{||}}{\sigma^2 - 1} \int i \cos\phi \sin\phi + \sigma \sin^2\phi d\phi, \tag{A.51}$$

$$M_{23} = -i \frac{q_\alpha}{m_\alpha \omega} \iint \frac{v_\perp^2 \omega \frac{\partial f_{\alpha 0}}{\partial v_{||}}}{\alpha} dv_\perp dv_{||} \int \sin\phi d\phi, \tag{A.52}$$

$$M_{31} = -i \frac{q_\alpha}{m_\alpha \omega} \iint \frac{v_\perp v_{||} \bar{\Delta} dv_\perp dv_{||}}{\sigma^2 - 1} \int \sigma \cos\phi - i sin\phi d\phi, \tag{A.53}$$

$$M_{32} = -i \frac{q_\alpha}{m_\alpha \omega} \iint \frac{v_\perp v_{||} \bar{\Delta} dv_\perp dv_{||}}{\sigma^2 - 1} \int i \cos\phi + \sigma \sin\phi d\phi, \tag{A.54}$$

$$M_{33} = -2\pi i \frac{q_\alpha}{m_\alpha \omega} \iint \frac{v_\perp v_{||} \omega \frac{\partial f_{\alpha 0}}{\partial v_{||}}}{\alpha} dv_\perp dv_{||}. \tag{A.55}$$

$$\tag{A.56}$$

Integrating over the azimuthal angle domain $\phi \in [0, 2\pi]$, we can obtain the following expressions for the elements of the tensor M_α,

$$M_{11} = -i\frac{q_\alpha}{m_\alpha\omega}\iint \pi\sigma\frac{v_\perp^2\bar{\Delta}dv_\perp dv_{||}}{\sigma^2-1}, \tag{A.57}$$

$$M_{12} = \frac{q_\alpha}{m_\alpha\omega}\iint \pi\frac{v_\perp^2\bar{\Delta}dv_\perp dv_{||}}{\sigma^2-1}, \tag{A.58}$$

$$M_{21} = -M_{12}, \tag{A.59}$$

$$M_{22} = M_{11}, \tag{A.60}$$

$$M_{33} = -2\pi i\frac{q_\alpha}{m_\alpha\omega}\iint \frac{v_\perp v_{||}\omega\frac{\partial f_{\alpha 0}}{\partial v_{||}}}{\alpha}dv_\perp dv_{||}, \tag{A.61}$$

$$M_{13} = M_{23} = M_{31} = M_{32} = 0. \tag{A.62}$$

$$\tag{A.63}$$

Now replacing these results into Eqs. A.46 and then into A.19, we could find the dispersion tensor elements,

$$\Lambda_{11} = \Lambda_{22} = 1 - \eta^2 + 4\pi\chi_{11}, \tag{A.64}$$

$$\Lambda_{12} = -\Lambda_{21} = 4\pi\chi_{12}, \tag{A.65}$$

$$\Lambda_{33} = 1 + 4\pi\chi_{33}, \tag{A.66}$$

$$\Lambda_{13} = \Lambda_{23} = \Lambda_{31} = \Lambda_{32} = 0. \tag{A.67}$$

Where χ_{ij} are elements of the electric susceptibility tensor. From here, we can show that for parallel waves propagation, this tensor is diagonal,

$$\Lambda_\pm = \Lambda_{11} \pm i\Lambda_{12}, \tag{A.68}$$

$$\Lambda_{||} = \Lambda_{33}, \tag{A.69}$$

in the polarized coordinates (+ right and - for the left). The elements are

$$\Lambda_\pm = 1 - \eta^2 + 4\pi\sum_\alpha \chi_{\pm\alpha}, \tag{A.70}$$

$$\Lambda_{||} = 1 + 4\pi\sum_\alpha \chi_{||\alpha}. \tag{A.71}$$

Then, the electric susceptibility tensor elements in terms of velocity distribution are

$$\chi_\pm = \frac{\omega_{p\alpha}^2}{4\omega}\int \frac{\partial f_\alpha}{\partial v_\perp} \pm \frac{k_{||}}{\omega}\left(v_\perp\frac{\partial f_\alpha}{\partial v_{||}} - v_{||}\frac{\partial f_\alpha}{\partial v_\perp}\right)dv_{||}dv_\perp, \tag{A.72}$$

$$\chi_{||} = \frac{\omega_{p\alpha}^2}{4\omega}\int \frac{v_{||}v_\perp}{\omega - k_{||}v_{||}}\frac{\partial f_\alpha}{\partial v_{||}}dv_{||}dv_\perp. \tag{A.73}$$

$$\tag{A.74}$$

A.2 Analytic results

From linear kinetic theory, we have obtained expressions for the elements of the susceptibility tensor, which in the case of a Maxwellian distribution are given by,

$$\chi_{\pm} = \frac{\omega_{p\alpha}^2}{4\pi\omega^2}\left(A + \phi_{\pm} Z(\xi_{\pm}) + 1\right), \tag{A.75}$$

where

$$Z(\xi) = \frac{1}{\sqrt{\pi}} \int_{\infty}^{\infty} \frac{e^{s^2}}{s-\xi} ds; \phi_{\pm} = A\xi_{\pm} \mp \frac{\Omega_{\alpha}}{k_{||} u_{||}}; \xi_{\pm} = \frac{\omega \pm \Omega_{\alpha}}{k_{||} u_{||}}; A = \frac{T_{\perp}}{T_{||}}.$$

For the Olbertian Kappa, we obtain,

$$\chi_{\pm} = \frac{\omega_{p\alpha}^2}{4\pi\omega^2}\left(A + \phi_{\pm} Z_{\kappa}(\xi_{\pm}) + 1\right). \tag{A.76}$$

For the Modified Kappa,

$$\chi_{\pm} = \frac{\omega_{p\alpha}^2}{4\pi\omega^2}\left(A + \phi_{\pm\kappa} Z_{\kappa}(\xi_{\pm\kappa}) + 1\right). \tag{A.77}$$

where

$$\phi_{\pm\kappa} = \left(\frac{\kappa}{\kappa - 3/2}\right)^{1/2} \phi_{\pm}; \xi_{\pm\kappa} = \left(\frac{\kappa}{\kappa - 3/2}\right)^{1/2} \xi_{\pm}$$

$$Z_{\kappa} = \frac{\Gamma(\kappa)}{\sqrt{\pi\kappa}\Gamma(\kappa - 1)} \int_{-\infty}^{\infty} \frac{dt}{(t-\xi)(1 + \frac{t^2}{\kappa})^{\kappa}},$$

$$Z_k(\xi) = i\frac{\kappa - \frac{1}{2}}{\kappa^{3/2}} F_{21}\left[1, 2\kappa, \kappa + 1; \frac{1}{2}\left(1 - \frac{\xi}{i\sqrt{\kappa}}\right)\right]. \tag{A.78}$$

Where F_{21} is the hypergeometric function, which can be used instead of the modified dispersion function for both Kappa interpretations when $\kappa > 1/2$ [72].

A.3 Normalization and parametrization

To obtain information at the kinetic scale of electrons, we use dimensionless expressions by normalizing frequencies to the absolute value of the electron gyro-frequency

and wave numbers are normalized to electron inertial length.

$$x = \frac{\omega}{|\Omega_e|}; y = \frac{kc}{\omega_{pe}}, \tag{A.79}$$

$$A_\alpha = \frac{m_\alpha}{m_p}, \tag{A.80}$$

$$\mu_\alpha = \frac{T_{\perp\alpha}}{T_{||\alpha}}, \tag{A.81}$$

$$Z_\alpha = \frac{q_\alpha}{e}, \tag{A.82}$$

$$P_\alpha = \frac{\omega_{p\alpha}}{|\Omega_e|} \tag{A.83}$$

$$\beta_{\alpha||} = \frac{n_0 k_B T_{\alpha||}}{B_0^2/8\pi}, \tag{A.84}$$

$$\eta_\alpha = \frac{n_\alpha}{n_0}. \tag{A.85}$$

$$\tag{A.86}$$

The dimensionless version of the wave refractive index is,

$$\frac{k_{||}^2 c^2}{\omega^2} = \frac{\left(y^2 \frac{\omega_{pe}^2}{c^2}\right) c^2}{x^2 |\Omega_e|^2} = \frac{y^2}{x^2} \frac{\omega_{pe}^2}{|\Omega_e|^2} = \frac{y^2}{x^2} P^2. \tag{A.87}$$

The second term, which also appears in all dispersion tensor elements stands for

$$\xi_\alpha^0 = \frac{\omega}{k u_{||}^\alpha} = \frac{x|\Omega_e|}{\left(\frac{\omega_{pe} y}{c u_{||}^\alpha}\right)} = \frac{x}{y} \frac{|\Omega_e| c}{\omega_{pe} u_{||}^\alpha} = \frac{x}{y} \frac{|-e|B_0}{m_e c} \sqrt{\frac{m_e}{4\pi n_0 e^2}} \frac{c}{u_{||}^\alpha},$$

$$\xi_\alpha^0 = \frac{x}{y} \frac{B_0}{\sqrt{4\pi n_0 m_e}} \sqrt{\frac{m_\alpha}{2 k_B T_{||}^\alpha}} \cdot \sqrt{\frac{n_0^\alpha}{n_0^\alpha}} = \frac{x}{y} \frac{B_0}{\sqrt{8\pi n_0^\alpha k_B T_{||}^\alpha}} \sqrt{\frac{n_0^\alpha}{n_0}} \sqrt{\frac{m_\alpha}{m_e}},$$

$$\xi_\alpha^0 = \frac{x}{y} \sqrt{\frac{1}{\beta_{||}^\alpha}} \sqrt{\frac{n_0^\alpha}{n_0}} \sqrt{\frac{m_\alpha}{m_e}} \cdot \sqrt{\frac{m_p}{m_p}} = \frac{x}{y} \sqrt{\frac{1}{\beta_{||}^\alpha}} \sqrt{\eta_\alpha} \sqrt{A_\alpha} \sqrt{\frac{1}{A_e}} = \frac{x}{y} \sqrt{\frac{\eta_\alpha A_\alpha}{\beta_{||^\alpha A_e}}}. \tag{A.88}$$

The next term stands for

$$\xi_n^\alpha = \frac{\omega}{k_{||} u_{||}^\alpha} + n \frac{\Omega_\alpha}{k_{||} u_{||}^\alpha}. \tag{A.89}$$

As we showed above, the first term is already dimensionless, therefore we focus only on the second term

$$\frac{\Omega_\alpha}{k_{||} u_{||}^\alpha} = \frac{\Omega_\alpha}{\left(\frac{\omega_{pe}}{c} y\right)} = \frac{1}{y} \frac{\Omega_\alpha c}{\omega_{pe} u_{||}^\alpha} = \frac{1}{y} \frac{\left(\frac{q_\alpha B_0}{m_\alpha c}\right) c}{\sqrt{\frac{4\pi n_o e^2}{m_e}} \sqrt{\frac{2 k_B T_{||}^\alpha}{m_\alpha}}} = \frac{1}{y} \frac{q_\alpha B_0}{m_\alpha c} \sqrt{\frac{m_e}{4\pi n_0 e^2}} \sqrt{\frac{m_\alpha}{2 k_B T_{||}^\alpha}} c,$$

$$\frac{\Omega_\alpha}{k_{||}u_{||}^\alpha} = \frac{1}{y}\frac{q_\alpha}{e}B_0\sqrt{\frac{m_e}{m_\alpha}}\frac{1}{\sqrt{8\pi k_B T_{||}^\alpha}}\frac{1}{\sqrt{n_0}}\cdot\sqrt{\frac{m_p n_0^\alpha}{m_p n_0^\alpha}},$$

$$\frac{\Omega_\alpha}{k_{||}u_{||}^\alpha} = \frac{1}{y}Z_\alpha B_0\frac{1}{\sqrt{8\pi k_B T_{||}^\alpha n_0^\alpha}}\sqrt{\frac{m_e}{m_p}}\sqrt{\frac{m_p}{m_\alpha}}\sqrt{\frac{n_0^\alpha}{n_0}},$$

$$\frac{\Omega_\alpha}{k_{||}u_{||}^\alpha} = \frac{1}{y}Z_\alpha\sqrt{\frac{1}{\beta_{||}^\alpha}}\sqrt{A_e}\sqrt{\frac{1}{A_\alpha}}\sqrt{\eta_\alpha} = \frac{1}{y}Z_\alpha\sqrt{\frac{A_e\eta_\alpha}{\beta_{||}^\alpha A_\alpha}}. \tag{A.90}$$

Hence, the whole dimensionless term is,

$$\xi_n^\alpha = \frac{x}{y}\sqrt{\frac{\eta_\alpha A_\alpha}{\beta_{||}^\alpha A_e}} + \frac{nZ_\alpha}{y}\sqrt{\frac{A_e\eta_\alpha}{\beta_{||}^\alpha A_\alpha}}. \tag{A.91}$$

With these results we obtain

$$\phi_n^\alpha = \frac{1}{y}\sqrt{\frac{A_\alpha\eta^\alpha}{A_e\beta_{||}^\alpha}}\left(x - nZ_\alpha\frac{A_e}{A_\alpha}\right) + \frac{n}{y}Z_\alpha\sqrt{\frac{A_e\eta^\alpha}{A^\alpha\beta_{||\alpha}}}\frac{1}{\mu_\alpha}. \tag{A.92}$$

All dimensionless expressions described above are valid for all distribution cases, but for the Modified case it will be useful to weight this expression with a function of κ values,

$$\xi_{n\kappa}^\alpha = \sqrt{\frac{\kappa}{\kappa - 3/2}}\xi_n^\alpha, \tag{A.93}$$

$$\phi_{n\kappa} = \sqrt{\frac{\kappa}{\kappa - 3/2}}\phi_n. \tag{A.94}$$

The last term to have all dispersion tensor elements dimensionless and normalized is,

$$\frac{\omega_{ps}^\alpha}{\omega^2} = \frac{1}{x^2}\frac{\frac{4\pi n_0^\alpha q_\alpha^2}{m_\alpha}}{\frac{e^2B_0^2}{m_e^2c^2}} = \frac{1}{x^2}\frac{4\pi n_0^\alpha q_\alpha^2}{m_\alpha}\frac{m_e^\alpha c^2}{e^2B_0^2}$$

$$\frac{\omega_{ps}^\alpha}{\omega^2} = \frac{1}{x^2}\frac{P^2\eta_p}{Z_e^2A_e\eta_e}\eta_\alpha\frac{1}{\eta_p}A_e^2\frac{1}{A_\alpha}Z_\alpha^2 = \frac{1}{x^2}\frac{P^2\eta_p}{Z_e^2A_e\eta_e}\frac{Z_\alpha^2A_e^2\eta_\alpha}{\eta_pA_\alpha},$$

$$\frac{\omega_{ps}^2}{\omega^2} = \frac{1}{x^2}P^2\frac{Z_\alpha^2}{Z_e^2}\frac{A_e\eta_\alpha}{A_\alpha\eta_e}. \tag{A.95}$$

Appendix B

B.1 Electromagnetic fluctuations in magnetized plasma

In Fourier domain the pertubation of the electric field may be expressed as

$$\langle \delta E_{i(\mathbf{k},\omega)} \rangle = \frac{\int \delta \hat{E}_i^* \delta \hat{h}_\mu \frac{\partial f_\alpha}{\partial H_\mu} dv}{\int f_\alpha dv}. \tag{B.1}$$

Here, we define Fourier-Laplace transformed quantities with a hat, such as $\delta \hat{E}_i := \delta E_{i(\mathbf{k},\omega)}$ and $\delta \hat{h}_\mu := \delta h_{\mu(\mathbf{k},\omega)}$. In addition, $()^*$ means the complex conjugate expression.

We propose variations in the internal energy δh_μ for which the dissipative linear process holds. Hence, from charge and energy conservation laws, the time variation of the local perturbation stands for

$$\frac{\partial \delta h_\mu}{\partial t} = -\int \delta E_\mu \cdot \delta J_\mu dV. \tag{B.2}$$

The source of the perturbation is considered purely by the inverse of the Joule heating, *i.e.*, stochastic movement of charges or energy supplied by current densities opposite to the electric field. To obtain the spectra of magnetic fluctuations, it would be useful to compute Fourier components of this quantity.

$$\delta \hat{h}_\mu = -\frac{i}{2\omega} \delta \hat{J}_\mu \delta \hat{E}_i.. \tag{B.3}$$

In addition, from linear kinetic theory, we can obtain

$$\langle \delta \hat{E}_i \rangle = \frac{4\pi \delta \hat{J}_\mu}{\omega^2} \Lambda_{i\mu}^{-1}. \tag{B.4}$$

By replacing Eqs. B.4 and B.3 in B.1 and considering that linear response of the magnetized plasmas is non-dependent on the disturbance $\delta\hat{J}_\mu$,

$$\frac{\int \delta\hat{E}_\mu \delta\hat{E}_i^* \frac{\partial f_\alpha}{\partial H_\mu} dv}{\int f_\alpha dv} = \frac{8\pi}{i\omega}\Lambda_{i\mu}^{-1}. \tag{B.5}$$

This expression added whit its conjugate,

$$i\omega\frac{\int \delta\hat{E}_\mu \delta\hat{E}_i^* \frac{\partial f_\alpha}{\partial H_\mu} dv}{\int f_\alpha dv} + i\omega^*\frac{\int \delta\hat{E}_i \delta\hat{E}_\mu^* \frac{\partial f_\alpha}{\partial H_\mu} dv}{\int f_\alpha dv} = 8\pi(\Lambda_{i\mu}^{-1*} - \Lambda_{\mu i}^{-1}). \tag{B.6}$$

It is easy to prove that for the right-hand side of this expression (RHS) (see reference [75])

$$8\pi(\Lambda_{i\mu}^{-1*} - \Lambda_{\mu i}^{-1}) = 32\pi^2(\lambda_{in}^{-1*}\chi_{nm}^*\Lambda_{m\mu}^{-1*} - \Lambda_{\mu m}^{-1}\chi_{mn}\lambda_{ni}^{-1}). \tag{B.7}$$

From this expression we could use the assumption of parallel propagation cases, then the dispersion tensor is diagonal, hence, $\lambda_{ij} = \lambda_i\delta_{ij}$, $\Lambda_{ij} = \Lambda_i\delta_{ij}$ and $\chi_{ij} = \chi_i\delta_{ij}$. Then, the right hand of the equation B.7,

$$RHS = 32\pi^2(\delta_{\mu m}\delta_{mn}\delta_{ni})(\lambda_i^{-1*}\chi_n^*\Lambda_m^{-1*} - \Lambda_\mu^{-1}\chi_m\lambda_n^{-1}). \tag{B.8}$$

Hence, replacing this result in Eq. B.6

$$RHS = i\omega\frac{\int \delta\hat{E}_\mu \delta\hat{E}_i^* \frac{\partial f_\alpha}{\partial H_\mu} dv}{\int f_\alpha dv} + i\omega^*\frac{\int \delta\hat{E}_i \delta\hat{E}_\mu^* \frac{\partial f_\alpha}{\partial H_\mu} dv}{\int f_\alpha dv}, \tag{B.9}$$

$$RHS = 32\pi^2(\delta_{\mu m}\delta_{mn}\delta_{ni})(\lambda_i^{-1*}\chi_n^*\Lambda_m^{-1*} - \Lambda_\mu^{-1}\chi_m\lambda_n^{-1}). \tag{B.10}$$

Then, considering $i = \mu$ in equation B.6, with the results of the RHS described above, we obtain

$$\frac{\int \delta\hat{E}_\mu^2 \frac{\partial f_\alpha}{\partial H_\mu} dv}{\int f_\alpha dv} = \frac{32\pi^2}{i(\omega+\omega^*)}(\lambda_\mu^{-1*}\chi_\mu^*\Lambda_\mu^{-1*} - \Lambda_\mu^{-1}\chi_\mu\lambda_\mu^{-1}). \tag{B.11}$$

For some representation of velocity distribution, usually exhibited in space plasma, the integral form of fluctuating electric field may be expressed as

$$\frac{\int \delta\hat{E}_\perp^2 \frac{\partial f_\alpha}{\partial H_\perp} dx}{\int f_\alpha dx} = \alpha_\perp\langle\delta\hat{E}_\perp^2\rangle. \tag{B.12}$$

Where α_μ is a scalar function to be determined by macroscopic parameters of the distribution in the direction μ (sum over μ index is implicit). Hence, we obtain

$$\langle\delta\hat{E}_\perp^2\rangle = \frac{32\pi^2}{i\alpha_\perp(\omega+\omega^*)}(\lambda_\perp^{-1*}\chi_\perp^*\Lambda_\perp^{-1*} - \Lambda_\perp^{-1}\chi_\perp\lambda_\perp^{-1}). \tag{B.13}$$

B.2 Electromagnetic fluctuations theory for Kappa distributions

A general expression of both Kappa distributions is,

$$F_\alpha = C_{\sigma_\alpha,\kappa_\alpha}\left[1+\frac{v_\perp^2}{(\kappa_\alpha-\sigma_\alpha)u_\perp^2}+\frac{(v_{||}-U_\alpha)^2}{(\kappa_\alpha-\sigma_\alpha)u_{||}^2}\right]^{-\kappa_\alpha-1}. \tag{B.14}$$

Here, $C_{\sigma_\alpha,\kappa_\alpha}$ is a constant of normalization, $u_{\perp,||}$ are the respective thermal velocities, U_α is a drift velocity, and σ_α a free parameter, with $\sigma_\alpha = \{0, 3/2\}$ values. Then, the change in kinetic energy in the distributions in the direction $\mu = \{\perp, ||\}$ is mediated by

$$\frac{\partial F_\alpha}{\partial H_\mu} = -\frac{2}{m_\alpha u_\mu^2}\frac{\kappa_\alpha+1}{k_\alpha-\sigma_\alpha}C_{\sigma_\alpha,\kappa_\alpha}\left[1+\frac{v_\perp^2}{(\kappa_\alpha-\sigma_\alpha)u_\perp^2}+\frac{(v_{||}-U_\alpha)^2}{(\kappa_\alpha-\sigma_\alpha)u_{||}^2}\right]^{-\kappa_\alpha-2}. \tag{B.15}$$

Then, including this result in the equation B.12,

$$\left[\frac{\int \delta\hat{E}_\perp^2\frac{\partial f_\alpha}{\partial H_\perp}dx}{\int f_\alpha dx}\right]_{\kappa_\alpha} = -\frac{1}{k_B T_{\perp\alpha}}\frac{k_\alpha+1}{\kappa_\alpha-\sigma_\alpha}C_{\sigma_\alpha,\kappa_\alpha}\int dv^3\cdot \tag{B.16}$$

$$\cdot\quad\left[1+\frac{v_\perp^2}{(\kappa_\alpha-\sigma_\alpha)u_\perp^2}+\frac{(v_{||}-U_\alpha)^2}{(\kappa_\alpha-\sigma_\alpha)u_{||}^2}\right]^{-\kappa_\alpha-2}|E_\perp|^2. \tag{B.17}$$

To find an equivalent expression of the fluctuating electric field for this distribution, we do this substitution,

$$\frac{v_i}{\sqrt{\kappa_\alpha-\sigma_\alpha}} = \frac{x_i}{\sqrt{\kappa_\alpha-\sigma_\alpha+1}}, dv_i = \frac{\sqrt{(\kappa_\alpha-\sigma_\alpha)}}{\sqrt{(\kappa_\alpha-\sigma_\alpha+1)}}dx_i.$$

Hence,

$$\frac{\int \delta\hat{E}_\perp^2\frac{\partial f_\alpha}{\partial H_\perp}dx}{\int f_\alpha dx} = -\frac{1}{k_B T_{\perp\alpha}}\frac{k_\alpha+1}{\kappa_\alpha-\sigma_\alpha}\frac{\sqrt{(\kappa_\alpha-\sigma_\alpha)^3}}{\sqrt{(\kappa_\alpha-\sigma_\alpha+1)^3}}\cdot$$

$$\cdot C_{\sigma_\alpha,\kappa_\alpha}\int dx^3\left[1+\frac{v_\perp^2}{(\kappa_\alpha-\sigma_\alpha+1)u_\perp^2}+\frac{(v_{||}-U_\alpha)^2}{(\kappa_\alpha-\sigma_\alpha+1)u_{||}^2}\right]^{-\kappa_\alpha-2}|E_\perp|^2. \tag{B.18}$$

Rearranging equation B.18,

$$\left[\frac{\int \delta\hat{E}_\perp^2\frac{\partial f_\alpha}{\partial H_\perp}dx}{\int f_\alpha dx}\right]_{\kappa_\alpha} = -\frac{1}{k_B T_{\perp\alpha}}\frac{(k_\alpha+1)\sqrt{(\kappa_\alpha-\sigma_\alpha)}}{\sqrt{(\kappa_\alpha-\sigma_\alpha+1)^3}}\frac{C_{\sigma_\alpha,\kappa_\alpha}}{C_{\sigma_\alpha,\kappa_\alpha+1}}.[\langle|E_\perp|^2\rangle_\alpha]_{\kappa_\alpha+1}. \tag{B.19}$$

We change the notation to specify $C_{\kappa_\alpha,\mathbf{a},b}$ the constant for the Modified case.

$$C_{\kappa_\alpha,\mathbf{a},b} = \frac{1}{\pi^{3/2}u_{\perp\alpha}^2 u_{||\alpha}} \frac{\kappa_\alpha \Gamma(\kappa_\alpha)}{(\kappa_\alpha - 3/2)^{3/2}\Gamma(\kappa_\alpha - \frac{1}{2})}, \tag{B.20}$$

$$C_{\kappa_\alpha+1,\mathbf{a},b} = \frac{1}{\pi^{3/2}u_{\perp\alpha}^2 u_{||\alpha}} \frac{(\kappa_\alpha+1)\Gamma(\kappa_\alpha+1)}{(\kappa_\alpha - 1/2)^{3/2}\Gamma(\kappa_\alpha + \frac{1}{2})}. \tag{B.21}$$

On the other hand, for the Olbertian case we change the constant, $C_{\kappa_\alpha,a,\mathbf{b}}$. Then working on the next expression,

$$C_{\kappa_\alpha,a,\mathbf{b}} = \frac{1}{\pi^{3/2}u_{\perp\alpha}^2 u_{||\alpha}} \frac{\Gamma(\kappa_\alpha)}{\kappa_\alpha^{1/2}\Gamma(\kappa_\alpha - \frac{1}{2})}, \tag{B.22}$$

$$C_{\kappa_\alpha+1,a,\mathbf{b}} = \frac{1}{\pi^{3/2}u_{\perp\alpha}^2 u_{||\alpha}} \frac{\Gamma(\kappa_\alpha+1)}{(\kappa_\alpha+1)^{1/2}\Gamma(\kappa_\alpha + \frac{1}{2})}. \tag{B.23}$$

Then, it is useful to take the following expression for the Modified case,

$$\frac{C_{\kappa_\alpha,\mathbf{a},b}}{C_{\kappa_\alpha+1,\mathbf{a},b}} = \frac{(\kappa_\alpha - 1/2)^{3/2}}{(\kappa_\alpha - 3/2)^{3/2}} \cdot \frac{\kappa_\alpha - 1/2}{(\kappa_\alpha + 1)}. \tag{B.24}$$

In the Olbertian case,

$$\frac{C_{\kappa_\alpha,a,\mathbf{b}}}{C_{\kappa_\alpha+1,a,\mathbf{b}}} = \frac{\Gamma(\kappa_\alpha)}{\kappa_\alpha^{1/2}\Gamma(\kappa_\alpha - \frac{1}{2})} \cdot \frac{(\kappa_\alpha+1)^{1/2}\Gamma(\kappa_\alpha + \frac{1}{2})}{\Gamma(\kappa_\alpha+1)}, \tag{B.25}$$

$$\frac{C_{\kappa_\alpha,a,\mathbf{b}}}{C_{\kappa_\alpha+1,a,\mathbf{b}}} = \frac{(\kappa_\alpha+1)^{1/2}}{\kappa_\alpha^{1/2}} \cdot \frac{\kappa_\alpha - 1/2}{\kappa_\alpha}. \tag{B.26}$$

Furthermore, for the Olbertian case $\sigma_\alpha = 0$, then,

$$\left[\frac{\int \delta\hat{E}_\perp^2 \frac{\partial f_\alpha}{\partial H_\perp} dx}{\int f_\alpha dx}\right]_{\kappa_\alpha} = -\frac{1}{k_B T_{\perp\alpha}} \frac{\sqrt{(\kappa_\alpha)}}{\sqrt{(\kappa_\alpha+1)}} \frac{C_{\sigma_\alpha,\kappa_\alpha,a,\mathbf{b}}}{C_{\sigma_\alpha,\kappa_\alpha+1,a,\mathbf{b}}} [\langle |E_\perp|^2 \rangle_\alpha]_{\kappa_\alpha+1}, \tag{B.27}$$

$$\left[\frac{\int \delta\hat{E}_\perp^2 \frac{\partial f_\alpha}{\partial H_\perp} dx}{\int f_\alpha dx}\right]_{\kappa_\alpha} = -\frac{1}{k_B T_{\perp\alpha}} \frac{\sqrt{(\kappa_\alpha)}}{\sqrt{(\kappa_\alpha+1)}} \frac{(\kappa_\alpha+1)^{1/2}}{\kappa_\alpha^{1/2}} \cdot \frac{\kappa_\alpha - 1/2}{\kappa_\alpha} [\langle |E_\perp|^2 \rangle_\alpha]_{\kappa_\alpha+1}, \tag{B.28}$$

$$\left[\frac{\int \delta\hat{E}_\perp^2 \frac{\partial f_\alpha}{\partial H_\perp} dx}{\int f_\alpha dx}\right]_{\kappa_\alpha} = -\frac{1}{k_B T_{\perp\alpha}} \cdot \frac{\kappa_\alpha - 1/2}{\kappa_\alpha} [\langle |E_\perp|^2 \rangle_\alpha]_{\kappa_\alpha+1}. \tag{B.29}$$

Now, for the Modified case $\sigma_\alpha = 3/2$, we obtain a similar result,

$$\left[\frac{\int \delta\hat{E}_\perp^2 \frac{\partial f_\alpha}{\partial H_\perp} dx}{\int f_\alpha dx}\right]_{\kappa_\alpha} = -\frac{1}{k_B T_{\perp\alpha}} \frac{(\kappa_\alpha+1)\sqrt{(\kappa_\alpha - 3/2)}}{\sqrt{(\kappa_\alpha - 3/2+1)^3}} \frac{C_{\sigma_\alpha,\kappa_\alpha,\mathbf{a},b}}{C_{\sigma_\alpha,\kappa_\alpha+1,\mathbf{a},b}} [\langle |E_\perp|^2 \rangle_\alpha]_{\kappa_\alpha+1},$$

$$\left[\frac{\int \delta\hat{E}_{\perp}^{2}\frac{\partial f_{\alpha}}{\partial H_{\perp}}dx}{\int f_{\alpha}dx}\right]_{\kappa_{\alpha}} = -\frac{1}{k_B T_{\perp\alpha}}\frac{(\kappa_{\alpha}+1)\sqrt{(\kappa_{\alpha}-3/2)}}{\sqrt{(\kappa_{\alpha}-3/2+1)^3}}\cdot \tag{B.30}$$

$$\cdot\frac{(\kappa_{\alpha}-1/2)^{3/2}}{(\kappa_{\alpha}-3/2)^{3/2}}\cdot\frac{\kappa_{\alpha}-1/2}{(\kappa_{\alpha}+1)}[\langle|E_{\perp}|^2\rangle_{\alpha}]_{\kappa_{\alpha}+1}, \tag{B.31}$$

$$\left[\frac{\int \delta\hat{E}_{\perp}^{2}\frac{\partial f_{\alpha}}{\partial H_{\perp}}dx}{\int f_{\alpha}dx}\right]_{\kappa_{\alpha}} = -\frac{1}{k_B T_{\perp\alpha}}\cdot\frac{\kappa_{\alpha}-1/2}{(\kappa_{\alpha}-3/2)}[\langle|E_{\perp}|^2\rangle_{\alpha}]_{\kappa_{\alpha}+1}. \tag{B.32}$$

Then, again for the Olbertian case,

$$\left[\frac{\int \delta\hat{E}_{\perp}^{2}\frac{\partial f_{\alpha}}{\partial H_{\perp}}dx}{\int f_{\alpha}dx}\right]_{\kappa_{\alpha}} = -\frac{1}{k_B T_{\perp\alpha}}\cdot\frac{\kappa_{\alpha}-1/2}{\kappa_{\alpha}}[\langle|E_{\perp}|^2\rangle_{\alpha}]_{\kappa_{\alpha}+1}, \tag{B.33}$$

$$\frac{1}{8\pi}[\langle|E_{\perp}|^2\rangle_{\alpha}]_{\kappa_{\alpha}} = \frac{\kappa_{\alpha}-1}{\kappa_{\alpha}-3/2}\cdot\frac{k_B T_{\perp\alpha}}{\omega\lambda_{\perp}}\cdot\mathrm{Im}\left[\frac{4\pi\chi_{\perp\alpha}}{\Lambda_{\perp}}\right], \tag{B.34}$$

$$\frac{1}{8\pi}[\langle|B_{\perp}|^2\rangle_{\alpha}]_{\kappa_{\alpha}} = \frac{c^2k_{|}^2}{\omega^2}\frac{\kappa_{\alpha}-1}{\kappa_{\alpha}-3/2}\cdot\frac{k_B T_{\perp\alpha}}{\omega\lambda_{\perp}}\cdot\mathrm{Im}\left[\frac{4\pi\chi_{\perp\alpha}}{\Lambda_{\perp}}\right]_{\kappa_{\alpha}-1}. \tag{B.35}$$

Also, for the Modified case

$$\frac{1}{8\pi}[\langle|E_{\perp}|^2\rangle_{\alpha}]_{\kappa_{\alpha}} = \frac{\kappa_{\alpha}-5/2}{\kappa_{\alpha}-3/2}\cdot\frac{k_B T_{\perp\alpha}}{\omega\lambda_{\perp}}\cdot\mathrm{Im}\left[\frac{4\pi\chi_{\perp\alpha}}{\Lambda_{\perp}}\right], \tag{B.36}$$

$$\frac{1}{8\pi}[\langle|B_{\perp}|^2\rangle_{\alpha}]_{\kappa_{\alpha}} = \frac{c^2k_{|}^2}{\omega^2}\frac{\kappa_{\alpha}-5/2}{\kappa_{\alpha}-3/2}\cdot\frac{k_B T_{\perp\alpha}}{\omega\lambda_{\perp}}\cdot\mathrm{Im}\left[\frac{4\pi\chi_{\perp\alpha}}{\Lambda_{\perp}}\right]_{\kappa_{\alpha}-1}. \tag{B.37}$$

In summary, from electromagnetic fluctuations theory, we compute the scalar function $\alpha_{\mu} = 1/k_B T_{\mu\alpha}$, then the magnetic spectra for the thermal case were obtained considering Maxwell equations,

$$\frac{1}{8\pi}[\langle|B_{\mu}|^2\rangle_{\alpha}]_{\kappa_{\alpha}} = \eta^2\frac{k_B T_{\mu\alpha}}{\omega\lambda_{\mu}}\cdot\mathrm{Im}\left[\frac{4\pi\chi_{\mu\alpha}}{\Lambda_{\mu}}\right]. \tag{B.38}$$

For the Olbertian case $\alpha_{\mu} = (1/k_B T_{\mu\alpha})(\kappa_{\alpha}-3/2)/(\kappa_{\alpha}-1)$ and the fluctuating magnetic spectra is

$$\frac{1}{8\pi}[\langle|B_{\mu}|^2\rangle_{\alpha}]_{\kappa_{\alpha}} = \eta^2\frac{\kappa_{\alpha}-1}{\kappa_{\alpha}-3/2}\cdot\frac{k_B T_{\mu\alpha}}{\omega\lambda_{\mu}}\cdot\mathrm{Im}\left[\frac{4\pi\chi_{\mu\alpha}}{\Lambda_{\mu}}\right]_{\kappa_{\alpha}-1}. \tag{B.39}$$

For the Modified case $\alpha_{\mu} = (1/k_B T_{\mu\alpha})(\kappa_{\alpha}-5/2)/(\kappa_{\alpha}-1)$ and magnetic spectra is

$$\frac{1}{8\pi}[\langle|B_{\mu}|^2\rangle_{\alpha}]_{\kappa_{\alpha}} = \eta^2\frac{\kappa_{\alpha}-5/2}{\kappa_{\alpha}-3/2}\cdot\frac{k_B T_{\mu\alpha}}{\omega\lambda_{\mu}}\cdot\mathrm{Im}\left[\frac{4\pi\chi_{\mu\alpha}}{\Lambda_{\mu}}\right]_{\kappa_{\alpha}-1}. \tag{B.40}$$

B.3 Normalized dimensionless magnetic fluctuations

Here, we compute normalized magnetic fluctuation for the Maxwell case. Then, we use the same parameters of dimensionless kinetic theory. Besides, to get Olbertian and Modified expressions for magnetic fluctuations is useful to replace the respective dispersion tensor and weight the result by the respective function of κ values. Hence, the magnetic fluctuations for the Maxwell case stands for

$$\langle|\delta B_{\pm}|^2\rangle = \frac{c^2k_{||}^2}{w^2}\frac{32\pi^2}{1-\frac{c^2k_{||}^2}{\omega^2}}\sum_{\alpha}\frac{k_BT_{\alpha\perp}}{\omega}\mathrm{Im}\left(\frac{\chi_{\alpha\pm}}{\Lambda_{\pm}}\right). \tag{B.41}$$

Generating a normalized expression

$$\frac{n_0|\Omega_e|}{2B_0^2}\langle|\delta B_{\pm}|^2\rangle = \frac{c^2k_{||}^2}{w^2}\frac{32\pi^2}{1-\frac{c^2k_{||}^2}{\omega^2}}\sum_{\alpha}\frac{n_0|\Omega_e|}{2B_0^2}\frac{k_BT_{\alpha\perp}}{\omega}\mathrm{Im}\left(\frac{\chi_{\alpha\pm}}{\Lambda_{\pm}}\right). \tag{B.42}$$

In the previous section on dimensionless kinetic theory, we presented the dimensionless elements for each distribution case. In this expression, everything is dimensionless except for the term

$$\begin{aligned}\frac{n_0|\Omega_e|}{2B_0^2}\frac{k_BT_{\alpha\perp}}{\omega} &= \frac{n_0|\Omega_e|}{2B_0^2}\frac{k_BT_{\alpha\perp}}{x|\Omega_e|},\\ \frac{n_0|\Omega_e|}{2B_0^2}\frac{k_BT_{\alpha\perp}}{\omega} &= \frac{1}{2x}\frac{k_BT_{\alpha\perp}n_0}{B_0^{\alpha}}\cdot\frac{n_0^2 8\pi}{n_0^{\alpha}8\pi} = \frac{1}{2x}\frac{k_BT_{\alpha\perp}n_0^{\alpha}8\pi}{B_0^2}\frac{n_0}{n_0^{\alpha}8\pi},\end{aligned} \tag{B.43}$$

$$\frac{n_0|\Omega_e|}{2B_0^2}\frac{k_BT_{\alpha\perp}}{\omega} = \frac{1}{2x}\beta_{\perp}^{\alpha}\frac{1}{\eta_{\alpha}}\frac{1}{8\pi} = \frac{\beta_{\perp}^{\alpha}}{2\cdot 8\pi\eta_{\alpha}}\frac{1}{x}. \tag{B.44}$$

Then the normalized and dimensionless expression stands for

$$\frac{n_0|\Omega_e|}{2B_0^2}\langle|\delta B_{\pm}|^2\rangle = 4\pi\frac{\frac{y^2}{x^2}P^2}{1-\frac{y^2}{x^2}P^2}\sum_{\alpha}\frac{\beta_{\perp}^{\alpha}}{2\eta_{\alpha}}\frac{1}{x}\mathrm{Im}\left(\frac{\chi_{\alpha\pm}}{\Lambda_{\pm}}\right). \tag{B.45}$$

Appendix C

C.1 Review of PIC space and time dimensions

To obtain electromagnetic fluctuation results for comparison with the ones obtained in theory, we use data from a particle-in-cell code. Therefore, below we will review the structure and particularities of this code.

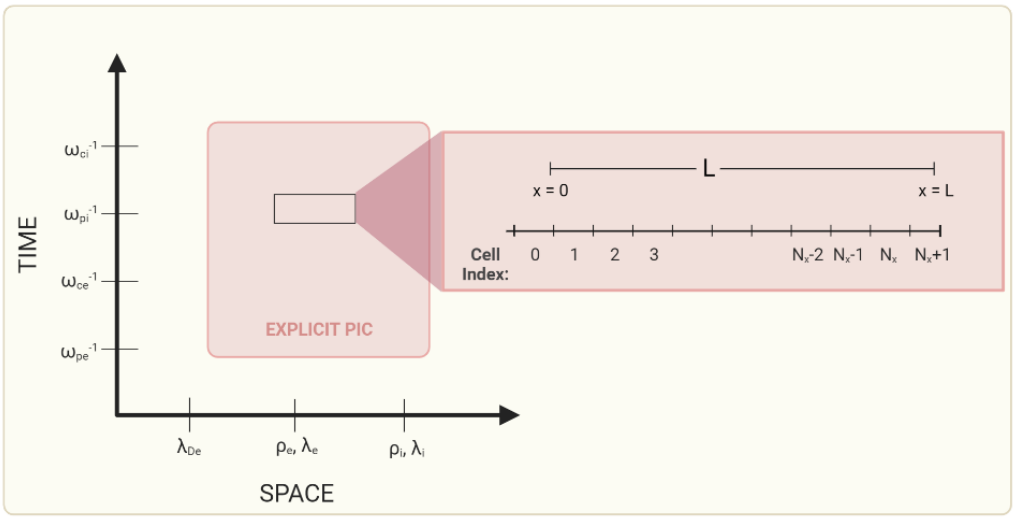

Figure C.1: Space and frequency dimensions to be considered in PIC scenarios. In the subpanel is a scheme of a one-dimensional grid used in the 1.5D particle-in-cell code. This grid has N_x cells.

In Figure C.1, we illustrate the space-time dimensions where explicit PIC codes are effective in describing kinetic plasma physics. The frequency range accessible with this approach corresponds to $\omega_{pe} < \omega < \Omega_i$, while the typical length of the system, L, is beyond the electron Debye length λ_{De} for magnetized plasmas, and falls between the gyro-radii of both species, $\rho_e < L < \rho_i$, or between the electron

and ion inertial lengths, $\lambda_e < L < \lambda_i$.

The sub-panel shows a schematic representation of the computational domain used in simulating the magnetized plasma. It consists of a one-dimensional grid with $N_x = 2048$ cells and 1000 particles per cell.

C.2 Stability conditions of the code

PIC codes must satisfy space-time constraints to ensure code stability. The time domain of the simulation must satisfy a threshold to prevent information from propagating faster than the speed of light. To accurately describe electron kinetic physics, the time step must be smaller than the time it takes an electromagnetic wave to travel one cell in a single time step,

$$\omega_{pe}\Delta t < 2. \tag{C.1}$$

Additionally, since electromagnetic fields are calculated on a grid, the Courant condition must be satisfied:

$$c\Delta t < \Delta x < \lambda_D, \tag{C.2}$$

where information propagation of electromagnetic waves towards the time step is ensured, and the spacing between grids must be less than or equal to the Debye length.

C.3 Code parameters

In PIC codes, to have relevant information around a space-time scale of interest, variables inside the code must be properly dimensionless. Hence, here we show the dimensionless expression used in the code. First, the time step is normalized to the electron plasma frequency

$$t = \frac{\Delta t}{\omega_{pe}}, \omega_{pe} = \sqrt{\frac{4\pi n_0 e^2}{m_e}}. \tag{C.3}$$

In addition, the space step is normalized to the inertial length of the electrons

$$x = \frac{\Delta x \omega_{pe}}{c}. \tag{C.4}$$

All velocities are normalized to the speed of light.

$$\bar{v} = \frac{v}{c}. \tag{C.5}$$

The magnetic field is normalized to the mean magnetic field B_0 with a weight factor indicating the rate of electron plasma frequency to electron gyro-frequency.

$$B = \frac{B}{B_0 P}, \tag{C.6}$$

where P is the ratio of plasma frequency and electron gyro-frequency. Also, the charge density is normalized to the electron density

$$\rho = \frac{\rho}{n_0 e}. \tag{C.7}$$

Then, the current density is normalized to

$$J = \frac{J}{e n_0 c}. \tag{C.8}$$

The selected parameters used in the code are listed below.

$$\begin{aligned}
\frac{m_e}{m_p} &= 1836, && \text{(C.9)}\\
L &= 265\lambda_e, && \text{(C.10)}\\
T_{max} &= 16365, && \text{(C.11)}\\
N_x &= 2048, && \text{(C.12)}\\
dt &= \frac{0.08}{\omega_{pe}}, && \text{(C.13)}\\
\text{particles per cell} &= 10^3, && \text{(C.14)}\\
P &= \frac{\omega_{pe}}{|\Omega_e|} = 5. && \text{(C.15)}
\end{aligned}$$

C.4 Code scheme

To numerically solve the scheme shown in Figure C.2, we review the numerical methods involved. The positions and velocities of the particles are solved using the Boris-Buneman method. This method starts with the Lorentz equation

$$\frac{dv}{dt} = \frac{q}{m}(\mathbf{E} + \mathbf{v} \times \mathbf{B}). \tag{C.16}$$

The discretization in time of Equation C.16 is given by,

$$\frac{\mathbf{v}^{t+\frac{\Delta t}{2}} - \mathbf{v}^{t-\frac{\Delta t}{2}}}{\Delta t} = \frac{q}{m}(\mathbf{E}^t + \frac{\mathbf{v}^{t+\frac{\Delta t}{2}} - \mathbf{v}^{t-\frac{\Delta t}{2}}}{\Delta t} \times \mathbf{B}^t). \tag{C.17}$$

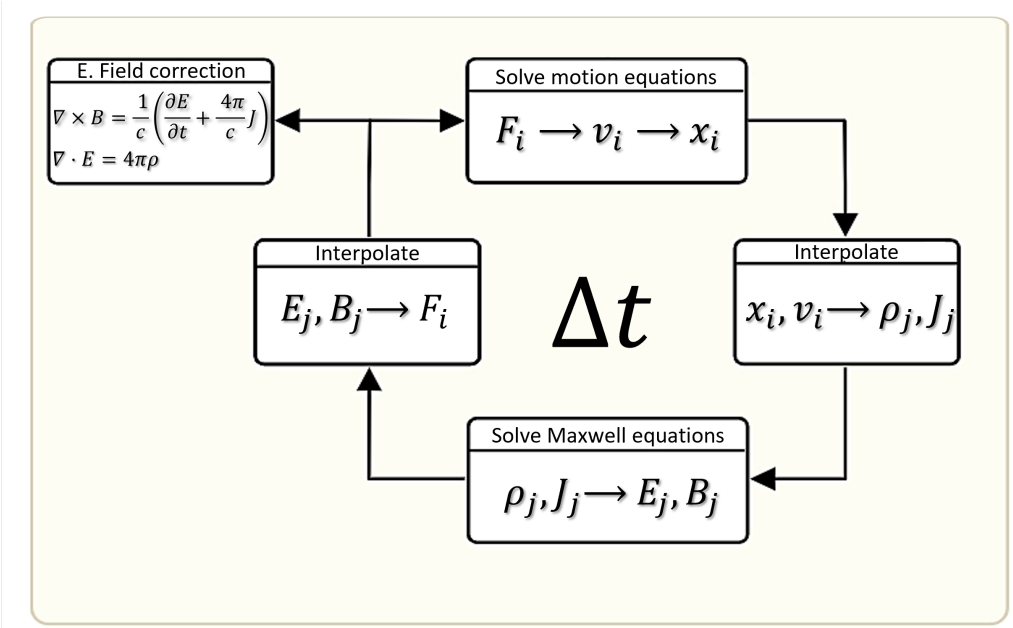

Figure C.2: Time iteration step for the PIC code.

Hence, considering the Boris-Bunemman method, the next step of positions and velocity in a magnetized plasma scheme,

$$x_{\Delta t+1} = x_{\Delta t} + \Delta t v_{\Delta t+1/2}, \tag{C.18}$$

$$v_{\Delta t+1/2} = \bar{v}_{\Delta t-1/2} + \frac{\Delta t q}{2m} E_{\Delta t}, \tag{C.19}$$

$$\tag{C.20}$$

with

$$\bar{v}_{\Delta t-1/2} = u + \left[u + \left(u \times \frac{\Delta t q \mathbf{E}_{\Delta t}}{2m}\right) \times \mathbf{B}_{\Delta t} \frac{\Delta t q}{m} / \left(1 + \left(\frac{\Delta t q \mathbf{B}_{\Delta t}}{2m}\right)^2\right)\right] \tag{C.21}$$

$$u = v_{\Delta t-1/2} + \frac{\Delta t q}{2m} \mathbf{E}_{\Delta t}. \tag{C.22}$$

The interpolation framework for each species' particle distribution $f_s(\mathbf{x}, \mathbf{v}, t)$ is obtained by summing up all N_s particles for each super particle distribution $f_p(\mathbf{x}, \mathbf{v}, t)$ (the simulated particle distribution).

$$f_s(\mathbf{x}, \mathbf{v}, t) = \sum_{n=1}^{N_s} f_p(\mathbf{x}, \mathbf{v}, t). \tag{C.23}$$

Additionally, to calculate the contribution of particles to the grid, it is useful to write each computational particle distribution in terms of the shape function S.

Hence,

$$f_p(\mathbf{x}, \mathbf{v}, t) = N_p S_x(\mathbf{x} - \mathbf{x}_p) S_v(\mathbf{v} - \mathbf{v}_p), \tag{C.24}$$

where the subscripts x and v, stand for the shape function in space and velocity. Usually, for spatial shape function, it is used a b-spline function and for velocities a delta function. The first order of this b-spline function stands for

$$b_0(\xi) = \begin{cases} 1 & \text{if} \quad |\xi| < 1/2, \\ \\ 0 & \text{otherwise.} \end{cases} \tag{C.25}$$

For larger orders,

$$b_l = \int_{\infty}^{\infty} b_0(\xi - \xi') b_{l-1}(\xi') d\xi', \tag{C.26}$$

With the conditions

$$\sum_{i}^{\infty} b_l(\xi + i) = 1, \tag{C.27}$$

$$\int_{\infty}^{\infty} b_l(\xi) d\xi = 1. \tag{C.28}$$

In this code implementation, we use the 2-spline function, which has a smooth Maxwellian shape. With this consideration, the motion equation for each super-particle may be expressed as

$$\frac{d\mathbf{x}_p}{dt} = \mathbf{v}_p, \tag{C.29}$$

$$\frac{d\mathbf{v}_p}{dt} = \frac{q}{m}(\mathbf{E}_p + \mathbf{v}_p \times \mathbf{B}_p). \tag{C.30}$$

The mesh where the electromagnetic field is solved, denoted by the subscript g, can be used to interpolate to the particles by employing the following interpolation function in an L-dimensional space of the grid.

$$W(\mathbf{x}_g - \mathbf{x}_p) = \int_L S_x(\mathbf{x} - \mathbf{x}_p) b_0 \left(\frac{\mathbf{x} - \mathbf{x}_g}{\Delta x} \right) d\mathbf{x} = \frac{b_1(\mathbf{x} - \mathbf{x}_p)}{\delta \mathbf{x}}. \tag{C.31}$$

Hence, the interpolated electromagnetic field from the grid to the particle are

$$\mathbf{E}_p = \sum_g \mathbf{E}_g W(\mathbf{x}_g - \mathbf{x}_p), \tag{C.32}$$

$$\mathbf{B}_p = \sum_g \mathbf{B}_g W(\mathbf{x}_g - \mathbf{x}_p). \tag{C.33}$$

$$\tag{C.34}$$

Also, charge density ρ and current density $\mathbf{J}$ may be interpolated to the grid as

$$\rho_g = \frac{1}{\Delta x}\sum_p qW(\mathbf{x}_g - \mathbf{x}_p), \tag{C.35}$$

$$\mathbf{J}_g = \frac{1}{\Delta x}\sum_p q\mathbf{v}_p W(\mathbf{x}_g - \mathbf{x}_p). \tag{C.36}$$

Then, integrating the shape function and the electromagnetic fields in the space L to compute the electromagnetic fields of the particles,

$$\mathbf{E}_p = \int_L S_x(\mathbf{x} - \mathbf{x}_p)\mathbf{E}(x)d\mathbf{x}, \tag{C.37}$$

$$\mathbf{B}_p = \int_L S_x(\mathbf{x} - \mathbf{x}_p)\mathbf{B}(x)d\mathbf{x}. \tag{C.38}$$

To solve Maxwell equations on the one-dimensional grid we use discretization with finite differences at second order. Hence, the one-dimension Maxwell system stands for

$$\frac{1}{c}\frac{\partial B_y}{\partial t} = \frac{\partial E_z}{\partial x}, \tag{C.39}$$

$$\frac{1}{c}\frac{\partial E_z}{\partial t} = \left(\frac{\partial B_y}{\partial x} - j_z\right). \tag{C.40}$$

For simplicity, we neglect the source term j_z first, hence

$$\frac{1}{c}\frac{\partial B_y}{\partial t} = \frac{\partial E_z}{\partial x}, \tag{C.41}$$

$$\frac{1}{c}\frac{\partial E_z}{\partial t} = \left(\frac{\partial B_y}{\partial x}\right). \tag{C.42}$$

Then, considering a central difference around x position with Taylor expansion, the spatial differentiation on Maxwell equations,

$$\frac{1}{c}\frac{\partial B_y}{\partial t} = \frac{E_z(x+\Delta x,t) - E_z(x-\Delta x,t)}{2\Delta x}, \tag{C.43}$$

$$\frac{1}{c}\frac{\partial E_z}{\partial t} = \frac{B_y(x+\Delta x,t) - B_y(x-\Delta x,t)}{2\Delta x}. \tag{C.44}$$

By considering a normalization $\Delta x/2 = \Delta x$, we obtain

$$\frac{1}{c}\frac{\partial B_y}{\partial t} = \frac{E_z(x+\frac{\Delta x}{2},t) - E_z(x-\frac{\Delta x}{2},t)}{\Delta x}, \tag{C.45}$$

$$\frac{1}{c}\frac{\partial E_z}{\partial t} = \frac{B_y(x+\frac{\Delta x}{2},t) - B_y(x-\frac{\Delta x}{2},t)}{\Delta x}. \tag{C.46}$$

We consider a staggered unidimensional uncoupled grid, noting that for an electric field evaluated at x_0, would be not related to any electric field evaluated at $x_0 + n\Delta x$ for odd numbers. This holds also for the magnetic field.

$$\frac{1}{c}\left(\frac{\partial B_y}{\partial t}\right)_{x+n\frac{\Delta x}{2}} = \frac{E_z(x+n\Delta x,t) - E_z(x-n\Delta x,t)}{\Delta x}, \tag{C.47}$$

$$\frac{1}{c}\left(\frac{\partial E_z}{\partial t}\right)_{n\Delta x} = \frac{B_y(x+n\frac{\Delta x}{2},t) - B_y(x-n\frac{\Delta x}{2},t)}{\Delta x}. \tag{C.48}$$

To simplify the notation, $A(x+n\Delta x) = (A)_n$, hence,

$$\frac{1}{c}\left(\frac{\partial B_y}{\partial t}\right)_{n+\frac{1}{2}} = \frac{(E_z(t))_{n+1} - (E_z(t))_n}{\Delta x}, \tag{C.49}$$

$$\frac{1}{c}\left(\frac{\partial E_z}{\partial t}\right)_{n} = \frac{(B_y(t))_{n+\frac{1}{2}} - (B_y(t))_{n-\frac{1}{2}}}{\Delta x}. \tag{C.50}$$

When we discretize the fields in time, we observe that the field points can be decoupled into nearby points by considering even or odd steps,

$$\frac{1}{c}\left(\frac{(B_y)_{n+\frac{1}{2},m+\frac{1}{2}} - (B_y)_{n+\frac{1}{2},m-\frac{1}{2}}}{\Delta t}\right) = \frac{(E_z)_{n+1,m} - (E_z)_{n,m}}{\Delta x}, \tag{C.51}$$

$$\frac{1}{c}\left(\frac{(E_z)_{n,m+1} - (E_z)_{n,m}}{\Delta t}\right) = \frac{(B_y)_{n+\frac{1}{2},m+\frac{1}{2}} - (B_y)_{n-\frac{1}{2},m+\frac{1}{2}}}{\Delta x}. \tag{C.52}$$

Hence, the next step in time for the electromagnetic fields yields

$$\frac{1}{c}\left(\frac{(B_y)_{n+\frac{1}{2},m+\frac{1}{2}}}{\Delta t}\right) = (B_y)_{n+\frac{1}{2},m-\frac{1}{2}} + \frac{\Delta t}{\Delta x}\frac{(E_z)_{n+1,m} - (E_z)_{n,m}}{\Delta x}, \tag{C.53}$$

$$\frac{1}{c}\left(\frac{(E_z)_{n,m+1}}{\Delta t}\right) = (E_z)_{n,m} + \frac{\Delta t}{\Delta x}\frac{(B_y)_{n+\frac{1}{2},m+\frac{1}{2}} - (B_y)_{n-\frac{1}{2},m+\frac{1}{2}}}{\Delta x}. \tag{C.54}$$

Now for our system, the magnetic field along x direction is constant and the system considers the source ($\mathbf{J}$),

$$(B_y)_{n,m+1} = (B_y)_{n,m} + \frac{\Delta t}{\Delta x}((E_z)_{n+\frac{1}{2},m+\frac{1}{2}} - (E_z)_{n-\frac{1}{2},m+\frac{1}{2}}), \tag{C.55}$$

$$(B_z)_{n+\frac{1}{2},m+\frac{1}{2}} = (B_z)_{n+\frac{1}{2},m-\frac{1}{2}} - \frac{\Delta t}{\Delta x}((E_y)_{n+\frac{1}{2},m} - (E_z)_{n-\frac{1}{2},m}). \tag{C.56}$$

$$\tag{C.57}$$

For the electric field,

$$
\begin{aligned}
(E_x)_{n+\frac{1}{2},m+\frac{1}{2}} &= (E_x)_{n+\frac{1}{2},m-\frac{1}{2}} - \Delta t (J_x)_{n+\frac{1}{2},m+\frac{1}{2}}, && \text{(C.58)} \\
(E_y)_{n,m+1} &= (E_y)_{n,m} - \frac{\Delta t}{\Delta x}((B_z)_{n+\frac{1}{2},m+\frac{1}{2}} - (B_z)_{n-\frac{1}{2}}, m+\frac{1}{2}) \\
&- \Delta t (J_y)_{n,m+1}, && \text{(C.59)} \\
(E_z)_{n+\frac{1}{2},m+\frac{1}{2}} &= (E_z)_{n+\frac{1}{2},m+\frac{1}{2}} + \frac{\Delta t}{\Delta x}((B_y)_{n+1,m} - (B_y)_{n,m}) \\
&- \Delta t (J_z)_{n+\frac{1}{2},m+\frac{1}{2}}. && \text{(C.60)}
\end{aligned}
$$

In addition, these fields have periodic boundary conditions, given by

$$
\begin{aligned}
E_y(N_0) &= E_y(N_x) \\
E_z(1) &= E_z(N_x+1) \\
B_y(N_0) &= E_y(N_x) \\
B_z(1) &= E_z(N_x+1)
\end{aligned}
$$

In addition, as shown in Figure C.2, the longitudinal electric field in the grid computed by Ampere's-Maxwell law is corrected to ensure consistency with Poisson's equation. This condition reduces numerical noise and results in a smooth time evolution of the code. This is a code based on KEMPO-1, implemented and modified by Adolfo Viñas, Rodrigo López, and Pablo Moya [42].